

JOURNAL OF MECHANICAL ENGINEERING

*Transaction of The Mechanical Engineering Division
The Institution of Engineers, Bangladesh*

ANALYSIS OF ACCELERATED FLOW OVER AN INSULATED WEDGE SURFACE USING VON KARMAN-POHLHAUSEN'S MOMENTUM INTEGRAL METHOD

Fazlar Rahman

1-12

STUDY ON DIFFERENT PROPERTIES OF LOW DENSITY POLYETHYLENE COMPOSITES REINFORCED WITH PINEAPPLE LEAF FIBER

Habibur Rahman, Muhamad Borhan Uddin and Ruhul Amin Khan

13-17

MACHINABILITY STUDY OF A KEVLAR AND GLASS REINFORCED POLYESTER COMPOSITE UNDER DRY AND COMPRESSED AIR-COOLING CONDITION

Mohammad Shahadath Hossain and Nikhil Ranjan Dhar

18-26

EFFECT OF DIFFERENT ANTIOXIDANTS ON PHYSIO-CHEMICAL PROPERTIES WITH BIODIESEL BLENDS

M.M. Rashed and Bengir Ahmed Shuvho

27-39

PRODUCTIVITY IMPROVEMENT OF GRID CASTING IN A BATTERY MANUFACTURING COMPANY - A CASE STUDY

Raihanul Haq and Abdullahil Azeem

40-45

EFFECT OF AROMATIC AMINE ANTIOXIDANTS ON EMISSION CHARACTERISTICS WITH MORINGA BIODIESEL BLEND IN A MULTI-CYLINDER DIESEL (MCD) ENGINE

M. M. Rashed and M. A. Kalam

46-48

DESIGN OF INTEGRATED SUPPLY CHAIN NETWORK UNDER TRANSIENT DEMAND AND COST UNCERTAINTY

Ferdous Sarwar, Md Saiful Islam

49-63

MARINE PROPELLER DESIGN USING CFD TOOLS

Goutam Kumar Saha, Md. Hayatul Islam Maruf, and Md. Rakibul Hasan

64-70



ANALYSIS OF ACCELERATED FLOW OVER AN INSULATED WEDGE SURFACE USING VON KARMAN-POHLHAUSEN'S MOMENTUM INTEGRAL METHOD

Fazlar Rahman

Department of Mechanical and Production Engineering (MPE)

Ahsanullah University of Science and Technology (AUST), Tejgaon Industrial Area, Bangladesh

Corresponding Email: Fazlar19@hotmail.com

Abstract: An accelerated flow over an insulated wedge surface is investigated for wedge angle in between 0.50 degree to 175 degree by using Von Karman-Pohlhausen's momentum integral method. The wedge surface is insulated at the leading edge and heating begin at the end of insulation zone. The effect of wedge angle on flow characteristics such as boundary layer thickness, momentum thickness, thermal boundary layer thickness and heat transfer coefficient are investigated. The equations of flow characteristics are derived for various wedge angles from the governing equations of Von Karman-Pohlhausen's momentum integral method and expressed in terms of Reynolds number, Prandtl number and Nusselt number. The results are plotted to investigate the flow within the boundary layer and found that separation of flow occurred earlier with increase of wedge angle to 105 degree and beyond. The results of flow characteristics for 0.5 degree wedge angle are compared with Blasius's exact solution of flat plate and also with VonKarman-Pohlhausen's solution of flat plate to validate the analysis presented in this paper. From the analysis, it is also revealed that Von Karman-Pohlhausen's momentum integral method is convenient to solve or draw outline of solution of flow over an arbitrary shaped object than Blasius's exact solution method.

Keywords: Flow over Wedge Surface; Boundary Layer Integral Method; Thermal Boundary Layer.

INTRODUCTION

The mathematical complexity of convection heat transfer is related to the non-linearity of Navier-Stokes equation and coupling of fluid flow with thermal fields. The Navier-Stokes equation is elliptical in nature and quite difficult to get solution. The boundary layer concept was first introduced by Prandtl in 1904 by simplification of Navier-Stokes equation. The simplified Navier-Stokes equation is known as Prandtl's boundary layer equations. It is easier to solved and exhibit completely different mathematical behavior than Navier-Stokes equation. The systematic calculation of Prandtl's boundary layer equations yields flow characteristics within the boundary layer of the fluid flow¹.

In 1908, Heinrich Blasius solved Prandtl's boundary layer equations into non-linear

ordinary differential equations. Despite the importance of Blasius's solution, in 1921 Von Karman, obtained momentum-integral equation through the simple expedient of integrating the boundary-layer equations across the boundary layer. Later the Von Karman momentum integral equations are refined by Ernst Pohlhausen, which is known as Von Karman-Pohlhausen's momentum integral method. It is well suited to generate a quick outline of a solution in complex cases and arbitrary shaped objects. The Von Karman-Pohlhausen's momentum integral methods provide significant mathematical simplification by reducing the number of independent variables. It gives an insight to the behavior of fluid particles within the boundary layer and easier to work with¹.

For mathematical simplification, Von Karman-Pohlhausen's momentum integral method is extensively used to solve a wide range of problems in fluid flow, convection heat and mass transfer from complex to arbitrary shaped object, where Blasius's exact solution is difficult to achieved²⁻³.

Flow over wedge surface is an important phenomenon in aerodynamics to design the aircraft's wing, missiles and other flying and floating objects, as well as, designing of other thermo-mechanical equipments and devices. There are numerous research papers published to investigate flow over edge surface with various conditions and situations. But only few of them investigated the flow over insulated wedge surface. Before mathematical formulation, the related papers and books are well studied¹⁻⁷. Zhang, Yuwen⁸ worked with flow over insulated web surface with a constant velocity U_∞ i.e. assuming, $\frac{dU}{dx} = 0$ by using boundary layer integral methods. Basu, B⁹ investigated flow over web surface without insulation with Blasius equations. Keshtkar, Mohammad¹⁰ investigated flow over wedge surface with varying viscosity and heat generation of Falkner-Skan flow. Akcay, Mehmet¹¹ investigated flow over a moving wedge surface with wall mass injection of non-Newtonian fluid by using Prandtl's boundary layer hypothesis. Ashwini, G.¹² investigated unsteady MHD (Magneto-hydrodynamics or magneto fluid dynamics) decelerating flow over wedge surface with heat generation or absorption in presence of magnetic field by using boundary layer equations and Keller-box solution method. Padet, J.¹³ investigated transient convective heat transfer over wedge surface with differential and integral method without insulation over the wedge surface. Butt, S., Adnan¹⁴ investigated flow and heat transfer over a static and a moving wedge surface by similarity method without insulation. Seddeek, M.¹⁵ investigated MHD Falkner-Skan flow and heat transfer over wedge

surface with variable viscosity and thermal conductivity by similarity solution. Mukhopadhyay, Swati¹⁶ investigated boundary layer flow and heat transfer of a Casson fluid over porous wedge surface. Before mathematical formulation, all papers¹⁻²⁰ are well studied and found that Von Karman-Pohlhausen's integral formulation is easier to work with complex and arbitrary shaped object, as well as, the accuracy of the solution is acceptable within the engineering and research communities.

The flow over wedge surface is investigated by Von Karman-Pohlhausen's integral methods for various wedge angles in between $0.5^\circ < \alpha < 175^\circ$.

METHODOLOGY

Considering two-dimensional laminar steady flow over a wedge surface, as shown in the **Fig.-1**. Where x is measured along parallel to the wedge surface and y is measured along perpendicular to the wedge surface. The surface of the wedge is insulated in between $0 < x < x_0$. The free stream velocity and temperature are U_∞ and T_∞ respectively. The temperature of the wedge surface and velocity of fluid over wedge surface are T_w and $U(x) = c x^m$ respectively, where $m = \frac{\beta}{2-\beta}$ ($m > 0$), $\beta = \frac{\alpha}{180}$ and α is the wedge angle in degree.

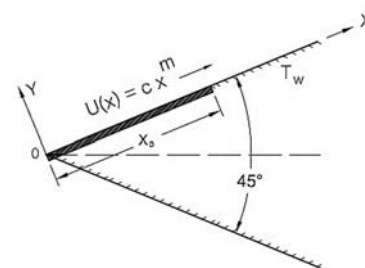


Fig.-1: Flow Over Wedge Surface.

Considering no generation of thermal energy, negligible dissipation, no gravity and no blowing or suction at the wedge surface. The wedge surface is insulated in between

$0 < x < x_0$, so there is no thermal boundary layer developed at the edge and wall temperature of wedge surface is same as free stream fluid temperature within insulated region i.e.

$$T_w = T_\infty.$$

The thermal boundary layer will be developed at $x > x_0$ and $\delta_t(x)$ is less than $\delta(x)$.

The ratio of $\frac{\delta_t(x)}{\delta(x)}$ will be less than 1 i.e. $\xi = \frac{\delta_t(x)}{\delta(x)} < 1$.

GOVERNING EQUATIONS

All the governing equations of Von Karman-Pohlhausen's momentum integral methods are readily available in H. Schlichting². The velocity of fluid over the wedge surface is given by the equation,

$$U(x) = c x^m \quad (1)$$

For steady flow with zero incidence and laminar boundary layer, the momentum thickness $\delta_2(x)$ is given by the following integral equation,

$$\frac{\rho U(x) \delta_2^2(x)}{\mu} = \frac{0.47}{U(x)^5} \int_0^x U(x)^5 dx \quad (2)$$

The relationship in between boundary layer shape factor $\Lambda(x)$ and boundary layer thickness $\delta(x)$ is given by the following equation,

$$\Lambda(x) = \frac{\rho \delta^2(x)}{\mu} \frac{dU(x)}{dx} \quad (3)$$

The dimensionless ratio of local velocity u to the free stream velocity U_∞ is given by the following equation,

$$\frac{u}{U_\infty} = (2\eta - 2\eta^3 + \eta^4) + \frac{\Lambda(x)}{6} (\eta - 3\eta^2 + 3\eta^3 - \eta^4) \quad (4)$$

Where $\eta = \frac{y}{\delta(x)}$

Flat plate with zero incidences, the ratio of momentum thickness $\delta_2(x)$ and boundary layer thickness $\delta(x)$ is given by the following equation,

$$\frac{\delta_2(x)}{\delta(x)} = \frac{37}{315} - \frac{\Lambda(x)}{945} - \frac{\Lambda(x)^2}{9072} \quad (5)$$

The momentum layer shape factor $K(x)$ is related to the momentum thickness $\delta_2(x)$ by the following equation,

$$K(x) = \frac{\rho \delta_2^2(x)}{\mu} \frac{dU(x)}{dx} \quad (6)$$

$H(\xi)$ is the universal function of $\xi(x)$ and $\xi(x) = \frac{\delta_t(x)}{\delta(x)}$. The value of function

$H(\xi)$ is given by the following equations,

For $\xi \leq 1$, $H(\xi) = \frac{2}{15}\xi - \frac{3}{140}\xi^3 + \frac{1}{180}\xi^4$ and for $\xi > 1$,

$$H(\xi) = \frac{3}{10} - \frac{3}{10}\xi^{-1} + \frac{2}{15}\xi^{-2} + \frac{3}{140}\xi^{-4} + \frac{1}{180}\xi^{-5} \quad (7a-b)$$

The differential form of integral energy equation for the thermal boundary layer $\delta_t(x)$ is given by the following equation,

$$\frac{d}{dx} [U(x) H(\xi) \delta_t(x)] = \frac{2k}{\rho C_p} \frac{1}{\delta_t(x)} \quad (8)$$

The local rate of heat transfer is given by the following equation,

$$q_x = \frac{2k}{\delta_t(x)} (T_w - T_\infty) \quad (9a)$$

In terms of heat flux or coefficient of heat transfer equation (9a) can be written as,

$$q_x = h_x (T_w - T_\infty) \quad (9b)$$

$$\text{Where } h_x = \frac{2k}{\delta_t(x)} \quad (9c)$$

MATHEMATICAL FORMULATION

The equations related to the flow characteristics over the wedge surface are derived systematically as shown below by using governing equations (1) to (9) and expressed each equation in terms of non-dimensional constants of Reynolds number, Prandtl's number and Nusselt number. The effect of flow characteristics for various

wedge angle from $\alpha = 0.5^0$ to $\alpha = 175^0$ are investigated.

Momentum Thickness, $\delta_2(x)$:

From the governing equations (1) and (2),

$$\delta_2^2(x) = \frac{0.47\nu}{(c x^m)^6} \int_0^x (c x^m)^5 dx \quad (10a)$$

After integrating and applying boundary condition at $x = 0$, $\delta_2(x) = 0$, equation (10a) becomes,

$$\delta_2^2(x) = \left(\frac{0.47\nu}{c}\right) \left(\frac{x^{-m+1}}{5m+1}\right) \quad (10b)$$

$$\delta_2(x) = \left\{\frac{0.47\nu}{c(5m+1)}\right\}^{\frac{1}{2}} (x)^{\frac{-m+1}{2}} \quad (10c)$$

Local Reynolds number,

$$R_{ex} = \frac{U(x) \cdot x}{\nu} = \frac{c x^{m+1}}{\nu}$$

Substituting expression of local Reynolds number R_{ex} in equation (10c) and rearranging variables,

$$\frac{\delta_2(x)}{x} = \left(\frac{0.47}{5m+1}\right)^{\frac{1}{2}} \frac{1}{\sqrt{R_{ex}}} \quad (10d)$$

Boundary Layer Thickness, $\delta(x)$:

From the governing equation (1) and (3),

$$\Lambda(x) = \frac{\delta^2(x)}{\nu} (c m x^{m-1}) \quad (11a)$$

$$\delta^2(x) = \left(\frac{\nu}{c m}\right) (x^{-m+1}) \Lambda(x) \quad (11b)$$

$$\delta(x) = \left(\frac{\nu}{c m}\right)^{\frac{1}{2}} \left(x^{\frac{-m+1}{2}}\right) \Lambda(x)^{\frac{1}{2}} \quad (11c)$$

From the equations (10c), (11c) and governing equation (5),

$$\frac{1}{63} \left\{ \frac{37}{5} - \frac{\Lambda(x)}{15} - \frac{\Lambda(x)^2}{144} \right\} = \left(\frac{0.47m}{5m+1}\right)^{\frac{1}{2}} \left\{ \frac{1}{\Lambda(x)} \right\}^{\frac{1}{2}} \quad (12a)$$

$$\frac{\Lambda(x)^{\frac{5}{2}}}{144} + \frac{\Lambda(x)^{\frac{3}{2}}}{15} - \frac{37\Lambda(x)^{\frac{1}{2}}}{5} + 63 \left(\frac{0.47m}{5m+1}\right)^{\frac{1}{2}} = 0 \quad (12b)$$

$$\frac{\Lambda(x)^{\frac{5}{2}}}{144} + \frac{\Lambda(x)^{\frac{3}{2}}}{15} - \frac{37\Lambda(x)^{\frac{1}{2}}}{5} + C_2 = 0 \quad (12c)$$

$$\text{Where } C_2 = 63 \left(\frac{0.47m}{5m+1}\right)^{\frac{1}{2}} \quad (12d)$$

The value of $K(x)$ is found from the governing equation (1), (6) and equation (10c).

$$K(x) = \frac{1}{\nu} \left(\frac{0.47\nu}{c}\right) \left(\frac{x^{-m+1}}{5m+1}\right) (c m x^{m-1}) \quad (13a)$$

$$K(x) = \frac{0.47m}{5m+1} \quad (13b)$$

Expressing equation (11c) in terms of local Reynolds number R_{ex} ,

$$\frac{\delta(x)}{x} = \left\{ \frac{\Lambda(x)}{m} \right\}^{\frac{1}{2}} \frac{1}{\sqrt{R_{ex}}} \quad (14a)$$

$$\delta(x) = \left\{ \frac{\nu \Lambda(x)}{c m} \right\}^{\frac{1}{2}} \left(x^{\frac{-m+1}{2}} \right) \quad (14b)$$

$$\delta(x) = C_3 \left(x^{\frac{-m+1}{2}} \right) \quad (14c)$$

$$\text{Where } C_3 = \left\{ \frac{\nu \Lambda(x)}{c m} \right\}^{\frac{1}{2}} \quad (14d)$$

Thermal Boundary Layer Thickness, $\delta_t(x)$:

The thermal boundary layer $\delta_t(x)$ will be developed at $x \geq x_0$ and boundary layer will be developed at $x=0$ and $\xi(x) = \frac{\delta_t(x)}{\delta(x)}$ will be less than 1 ($\xi < 1$).

From governing equation (7a),

$$H(\xi) = \frac{2}{15} \left\{ \frac{\delta_t(x)}{\delta(x)} \right\} - \frac{3}{140} \left\{ \frac{\delta_t(x)}{\delta(x)} \right\}^3 + \frac{1}{180} \left\{ \frac{\delta_t(x)}{\delta(x)} \right\}^4 \quad (15a)$$

Neglecting higher order terms and substituting the value of $\delta(x)$ from the equation (14b),

$$H(\xi) = \frac{2}{15} \left\{ \frac{cm}{v\Lambda(x)} \right\}^{\frac{1}{2}} \left(x^{\frac{m-1}{2}} \right) \delta_t(x) \quad (15b)$$

Substituting value of $H(\xi)$ from equation (15b) and $U(x)$ from governing equation (1) to the governing equation (8),

$$\frac{d}{dx} \left[cx^m \frac{2}{15} \left\{ \frac{cm}{v\Lambda(x)} \right\}^{\frac{1}{2}} \left(x^{\frac{m-1}{2}} \right) \delta_t^2(x) \right] = \left(\frac{2k}{\rho C_p} \right) \frac{1}{\delta_t(x)} \quad (16a)$$

Rearranging the variables,

$$\left\{ x^{\frac{3m-1}{2}} \delta_t^2(x) \right\}^{\frac{1}{2}} d \left\{ x^{\frac{3m-1}{2}} \delta_t^2(x) \right\} = \frac{15}{2} \left(\frac{v}{c} \right)^{\frac{3}{2}} \left\{ \frac{\Lambda(x)}{m} \right\}^{\frac{1}{2}} \left(\frac{k}{\mu C_p} \right) \left(x^{\frac{3m-1}{4}} \right) dx \quad (16b)$$

$$\frac{3}{2} \left\{ x^{\frac{3m-1}{2}} \delta_t^2(x) \right\}^{\frac{3}{2}} = \left(\frac{v}{c} \right)^{\frac{3}{2}} \left\{ \frac{\Lambda(x)}{m} \right\}^{\frac{1}{2}} \left(\frac{1}{P_r} \right) \left\{ \frac{4}{3(m+1)} \right\} \left\{ x^{\frac{3(m+1)}{4}} \right\} + A_1 \quad (16c)$$

$$\left\{ x^{\frac{3m-1}{2}} \delta_t^2(x) \right\}^{\frac{3}{2}} = 30 \left(\frac{v}{c} \right)^{\frac{3}{2}} \left\{ \frac{\Lambda(x)}{m} \right\}^{\frac{1}{2}} \left(\frac{1}{P_r} \right) \left(\frac{1}{m+1} \right) \left\{ x^{\frac{3(m+1)}{4}} \right\} + A_2 \quad (16d)$$

Where A_1 and A_2 are integration constants. Applying boundary condition in the equation (16d), at $x = x_0$, $\delta_t(x) = 0$.

$$A_2 = -30 \left(\frac{v}{c} \right)^{\frac{3}{2}} \left\{ \frac{\Lambda(x)}{m} \right\}^{\frac{1}{2}} \left(\frac{1}{P_r} \right) \left(\frac{1}{m+1} \right) \left\{ x_0^{\frac{3(m+1)}{4}} \right\}$$

Substituting the value of constant A_2 in equation (16d),

$$\left[x^{\frac{3m-1}{2}} \delta_t^2(x) \right]^{\frac{3}{2}} = \left\{ \frac{30}{P_r(m+1)} \right\} \left(\frac{v}{c} \right)^{\frac{3}{2}} \left\{ \frac{\Lambda(x)}{m} \right\}^{\frac{1}{2}} x^{\frac{3(m+1)}{4}} \left[1 - \left(\frac{x_0}{x} \right)^{\frac{3(m+1)}{4}} \right] \quad (16e)$$

$$\delta_t^2(x) = \left\{ \frac{30}{P_r(m+1)} \right\}^{\frac{2}{3}} \left(\frac{v}{c} \right) \left\{ \frac{\Lambda(x)}{m} \right\}^{\frac{1}{3}} x^{-m+1} \left[1 - \left(\frac{x_0}{x} \right)^{\frac{3(m+1)}{4}} \right]^{\frac{2}{3}} \quad (16f)$$

$$\delta_t(x) = \left\{ \frac{30}{P_r(m+1)} \right\}^{\frac{1}{3}} \left\{ \frac{\Lambda(x)}{m} \right\}^{\frac{1}{6}} \left(\frac{v}{c x^m} \right)^{\frac{1}{2}} x \left[1 - \left(\frac{x_0}{x} \right)^{\frac{3(m+1)}{4}} \right]^{\frac{1}{3}} \quad (17a)$$

Rearranging the variables of equation (17a),

$$\delta_t(x) = C_4 \left(\frac{1}{P_r} \right)^{\frac{1}{3}} \left(\frac{v}{c} \right)^{\frac{1}{2}} x^{-\frac{m+1}{2}} \left[1 - \left(\frac{x_0}{x} \right)^{\frac{3(m+1)}{4}} \right]^{\frac{1}{3}} \quad (17b)$$

Expressing equation (17b) terms of local Reynolds number Re_x ,

$$\delta_t(x) = \left(\frac{30}{m+1} \right)^{\frac{1}{3}} \left\{ \frac{\Lambda(x)}{m} \right\}^{\frac{1}{6}} \left\{ \frac{1}{(Re_x)^{\frac{1}{2}} P_r} \right\} x \left[1 - \left(\frac{x_0}{x} \right)^{\frac{3(m+1)}{4}} \right]^{\frac{1}{3}} \quad (18a)$$

$$\delta_t(x) = C_4 \frac{1}{R_{ex}^{\frac{1}{2}} P_r^{\frac{1}{3}}} x \left[1 - \left(\frac{x_0}{x} \right)^{\frac{3(m+1)}{4}} \right]^{\frac{1}{3}} \quad (18b)$$

$$\text{Where, } C_4 = \left(\frac{30}{m+1} \right)^{\frac{1}{3}} \left\{ \frac{\Lambda(x)}{m} \right\}^{\frac{1}{6}} \quad (18c)$$

The value of $\delta_t(x)$ can be found if value of x_0 or local Reynolds number Re_{x0} and also Prandtl's number are known. The value of x_0 can be found from the local Reynolds number Re_{x0} at the end of insulation of the wedge surface, i.e. at $x = x_0$.

$$Re_{x0} = \frac{cx_0^{m+1}}{v} \quad (19a)$$

$$x_0 = \left(\frac{R_{ex} v}{c} \right)^{\frac{1}{m+1}} \quad (19b)$$

The values of shape factor $\Lambda(x)$ are found by solving equation (12c) numerically after substituting value of C_2 from equation (12d) and value of $K(x)$ is found from equation (13b). The value of C_3 and C_4 are found from the equations (14d) and (18c) respectively. The value of $K(x)$ and $\Lambda(x)$ for different wedge angle factors β , are shown in the **Table-1**. The results of **Table-1** are found analogous to the Holstein and Bohlen solution² for $\Lambda(x)$ and $K(x)$. It is assumed that the value of flow constant $c = 50$ i.e. $U(x) = 50 x^m$.

Table-1: Value of $\Lambda(x)$, $K(x)$, C_2 , C_3 & C_4

α^0	β	m	$\Lambda(x)$	$K(x)$	C_2	C_3	C_4
0.5	1/3	1/7	0.0	0.00	1.6	0.00	5.5
5	60	19	471	07	05	320	86
15	1/1	1/2	1.2	0.01	8.1	0.00	5.3
5	2	3	479	68	62	295	60
30	1/6	1/1	2.2	0.02	10.	0.00	5.1
0		1	390	94	798	273	49
45	1/4	1/7	3.0	0.03	12.	0.00	4.9
5			566	92	468	254	52
60	1/3	1/5	3.7	0.04	13.	0.00	4.7
0			507	70	658	238	66
75	5/1	5/1	4.3	0.05	14.	0.00	4.5
5	2	9	532	34	560	224	88
90	1/2	1/3	4.8	0.05	15.	0.00	4.4
0			853	88	270	210	16
105	7/1	7/1	5.2	0.06	15.	0.00	4.2
0	2	7	098	33	847	196	28
120	2/3	1/2	5.7	0.06	16.	0.00	4.0
20			969	71	325	187	84
130	13/18	13/23	6.0	0.06	16.	0.00	3.9
0			660	94	600	180	75

145	29/36	29/43	6.4	0.07	16.	0.00	3.8
5			447	25	963	170	12
160	8/9	4/5	6.7	0.07	17.	0.00	3.6
60			981	52	276	160	49
175	35/36	35/37	7.1	0.07	17.	0.00	3.4
5			306	76	549	151	85

Heat Transfer Coefficient, h_x :

Substituting the value of $\delta_t(x)$ from equation (18b) to the governing equation (9c),

$$h_x = \frac{2k}{x} \left(\frac{R_{ex}^{\frac{1}{2}} P_r^{\frac{1}{3}}}{C_4} \right) \left[1 - \left(\frac{x_0}{x} \right)^{\frac{3(m+1)}{4}} \right]^{-\frac{1}{3}} \quad (20a)$$

Substituting value of C_4 in equation (20a),

$$h_x = \frac{2k}{x} \left(\frac{m+1}{30} \right)^{\frac{1}{3}} \left\{ \frac{m}{\Lambda(x)} \right\}^{\frac{1}{6}} \left(R_{ex}^{\frac{1}{2}} P_r^{\frac{1}{3}} \right) \left[1 - \left(\frac{x_0}{x} \right)^{\frac{3(m+1)}{4}} \right]^{-\frac{1}{3}} \quad (20b)$$

Expanding local Reynolds number R_{ex} ,

$$h_x = \frac{2k}{C_4} \left(\frac{c}{v} \right)^{\frac{1}{2}} P_r^{\frac{1}{3}} \left(x^{\frac{m-1}{2}} \right) \left[1 - \left(\frac{x_0}{x} \right)^{\frac{3(m+1)}{4}} \right]^{-\frac{1}{3}} \quad (20c)$$

Expressing in terms of local Reynolds R_{ex} and Nusselts number N_{ux} equation (20c) yields,

$$N_{ux} = 2 \left(\frac{m+1}{30} \right)^{\frac{1}{3}} \left\{ \frac{m}{\Lambda(x)} \right\}^{\frac{1}{6}} \left(R_{ex}^{\frac{1}{2}} P_r^{\frac{1}{3}} \right) \left[1 - \left(\frac{x_0}{x} \right)^{\frac{3(m+1)}{4}} \right]^{-\frac{1}{3}} \quad (21)$$

RESULTS AND DISCUSSION

Considering, air is flowing over the wedge surface at 20°C i.e. $T_\infty = 20^\circ\text{C}$. Properties of air at 20°C are,

Density of air, $\rho = 1.2 \frac{\text{Kg}}{\text{m}^3}$

Specific heat at constant pressure, $C_p = 1.005 \frac{\text{KJ}}{\text{Kg K}}$

Viscosity of air, $\mu = 1.82 \times 10^{-5} \frac{\text{Kg}}{\text{m s}}$

Kinematic viscosity, $\nu = 15.2 \times 10^{-6} \frac{\text{m}^2}{\text{s}}$

Thermal conductivity, $K = 0.0257 \frac{\text{W}}{\text{m K}}$

Prandtl number, $Pr = 0.712$

Boundary Layer Thickness $\delta(x)$:

The boundary layer thickness, $\delta(x)$ is plotted in **Fig.-2(a)** and **Fig.-2(b)** from the equation (14b) for various wedge angle factors β and velocity constant $c = 50$ or local velocity over the wedge surface, $U(x) = 50 x^m$.

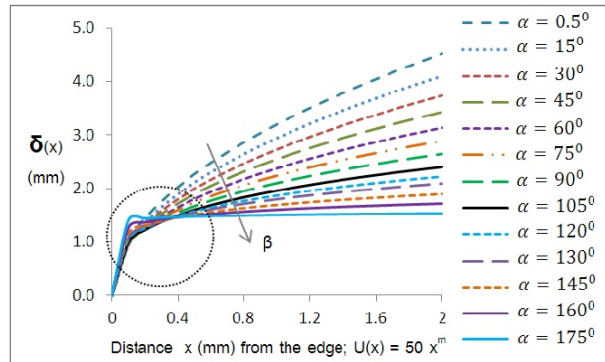


Fig.-2(a): Boundary Layer Thickness $\delta(x)$.

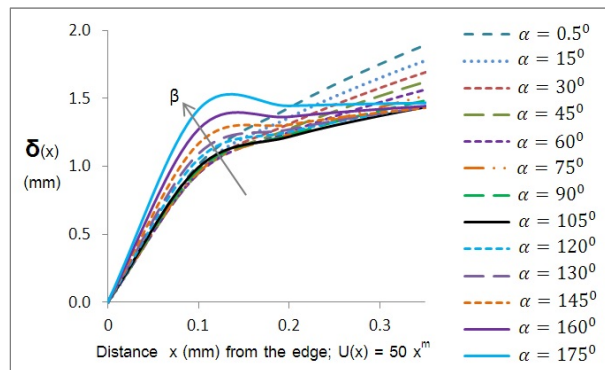


Fig.-2(b): Close View of Fig.-2(a).

From **Fig.-2(a)** and **2(b)**, it is observed that boundary layer thickness $\delta(x)$ increased with increasing of wedge angle factor β and

flow separated earlier with increasing of β , which makes agreement with the real situation. Flow is separated quickly with increasing of wedge angle to 105° and beyond. Substituting the value of $\Lambda(x) = 0.0471$ and $m = 1/719$ for wedge angle $\alpha = 0.5^\circ$ from **Table-1** to the equation (14a), the equation of boundary layer thickness $\delta(x)$ becomes,

$$\frac{\delta(x)}{x} = \frac{5.82}{\sqrt{Re_x}} \quad (22)$$

Solution of boundary layer thickness $\delta(x)$ of flat plate with zero incidences by Von Karman-Pohlhausen's momentum integral method and Blasius's exact solution² are given by the following equations respectively,

$$\frac{\delta(x)}{x} = \frac{5.84}{\sqrt{Re_x}} \quad (23)$$

$$\frac{\delta(x)}{x} = \frac{5.0}{\sqrt{Re_x}} \quad (24)$$

The equation (22) makes good agreement with equation (23) and also makes satisfactory agreement with equation (24).

Momentum Thickness $\delta_2(x)$:

The momentum thickness $\delta_2(x)$ is plotted in **Fig.-3(a)** and **Fig.-3(b)** from the equation (10c) for various wedge angle factors β and velocity constant $c = 50$ or local velocity over the wedge surface $U(x) = 50 x^m$.

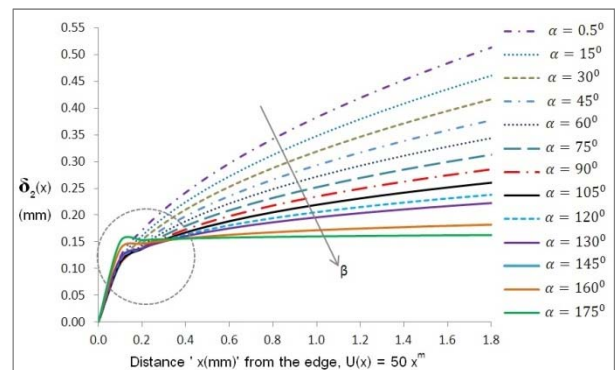


Fig.-3(a): Momentum Thickness $\delta_2(x)$.

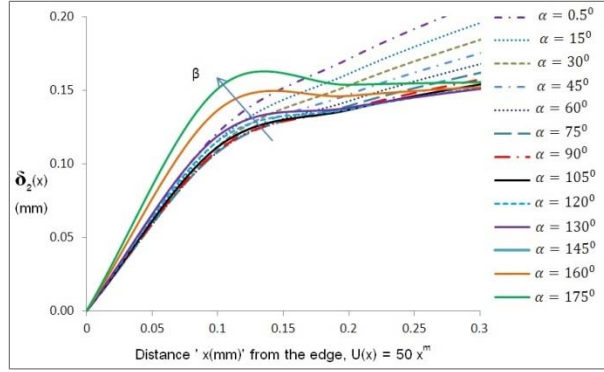


Fig.-3(b): Close View Fig.-3(a).

Form **Fig.-3(a)** and **3(b)**, it is observed that the momentum thickness $\delta_2(x)$ is analogous to the boundary layer thickness $\delta(x)$ for various wedge angle factors β ; which validates the acceptance of accuracy of the solution of momentum thickness $\delta_2(x)$. Substituting the value of m for wedge angle $\alpha = 0.5^\circ$ from **Table-1** to the equation (10d), the momentum thickness $\delta_2(x)$ becomes,

$$\frac{\delta_2(x)}{x} = \frac{0.683}{\sqrt{R_{ex}}} \quad (25)$$

Solution of momentum thickness $\delta_2(x)$ for flat plate with zero incidence by Von Karman-Pohlhausen's momentum integral method and Blasius's exact solution are given by the following equations respectively,

$$\frac{\delta_2(x)}{x} = \frac{0.686}{\sqrt{R_{ex}}} \quad (26)$$

$$\frac{\delta_2(x)}{x} = \frac{0.664}{\sqrt{R_{ex}}} \quad (27)$$

The equation (25) makes very good agreement with equation (26) and also satisfactory agreement with equation (27).

Velocity Distribution in Laminar Boundary Layer:

The velocity distribution in the laminar boundary layer is found by solving governing equation (4). Substituting value of $\Lambda(x)$ for different wedge angles from **Table-1** to the

governing equation (4) and numerically solve equation (4) for different values of $\eta = \frac{y}{\delta(x)}$ and $\frac{u}{U_\infty}$ respectively. The velocity distribution for laminar flow over wedge surface is shown in the **Fig.-4(a)** and **Fig.-4(b)**.

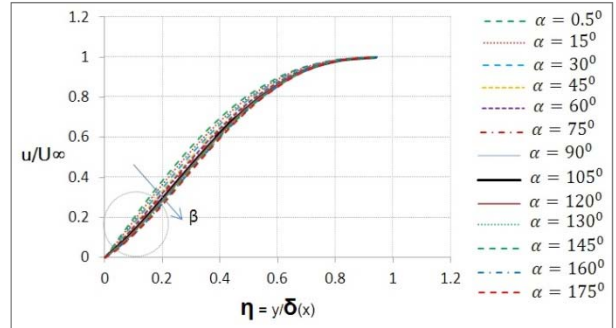


Fig.-4(a): Velocity Distribution for $U(x) = 50x^m$.

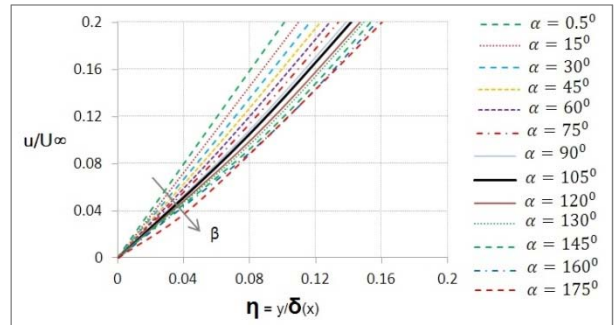


Fig.-4(b): Close View of Fig.-4(a).

From **Fig.-4(a)** and **4(b)**, it is observed that the boundary layer separated earlier with increasing of wedge angle to 105° and beyond. The profiles of velocity distribution over wedge surface for different wedge angles are found realistic and it makes good agreement with the velocity distribution of Blasius's exact solution for flow over wedge surface for laminar flow².

Thermal Boundary Thickness $\delta_t(x)$:

If the value of local Reynolds number, R_{ex0} at the end of the insulation is known then value of x_0 can be found from equation (19b).

The thermal boundary thickness $\delta_t(x)$ is plotted in **Fig.-5** by substituting the value of x_0 for local Reynolds number $Re_{x0} = 1000$, Prandtl number $Pr = 0.712$ and value of C_4 from **Table-1** to the equation (17b).

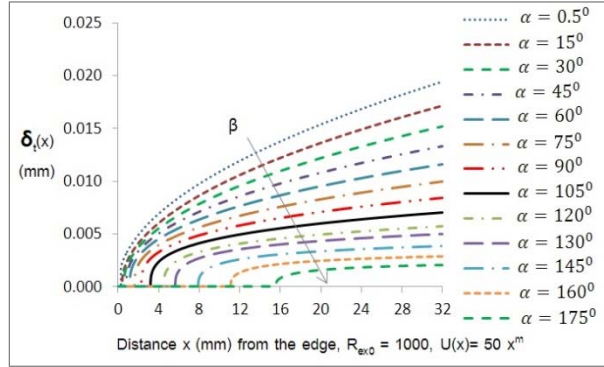


Fig.-5: Thermal Boundary Layer Thickness $\delta_t(x)$ for $Re_{x0} = 1000$; $Pr = 0.712$

If there is no insulation in the wedge surface i.e. $x_0 = 0$, the equation (18b) yields,

$$\delta_t(x) = C_4 \left(\frac{1}{R_{ex}^2 P_r^{1/3}} \right) x \quad (28)$$

Substituting value of C_4 for wedge angle $\alpha = 0.5^\circ$ from the **Table-1** to the equation (28),

$$\delta_t(x) = \frac{5.586 x}{P_r^{1/3} \sqrt{R_{ex}}} \quad (29)$$

Exact solution of thermal boundary layer for flow over flat plate with zero incidences is given by the following equation²,

$$\delta_t(x) = \frac{5.0 x}{P_r^{1/3} \sqrt{R_{ex}}} \quad (30)$$

The equation (29) makes satisfactory agreement with equation (30).

Heat Transfer Coefficient, h_x :

The heat transfer coefficient h_x is plotted in **Fig.-6(a)** and **Fig.-6(b)** by substituting value of x_0 for local Reynolds number $Re_{x0} = 1000$,

Prandtl number $Pr = 0.712$ and value of C_4 from **Table-1** to the equation (20c).

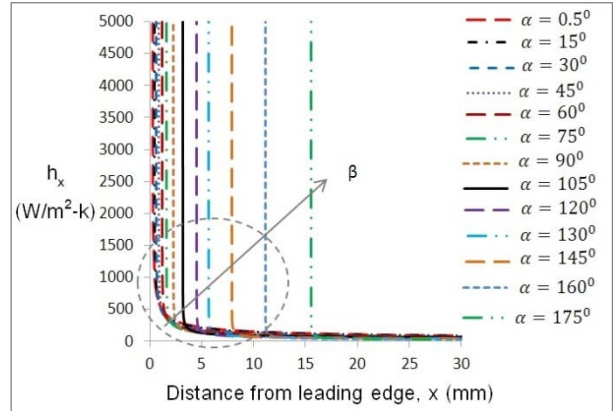


Fig.-6(a): Heat Transfer Coefficient, h_x for $Re_{x0} = 1000$, $Pr = 0.712$ for $U(x) = 50 x^m$.

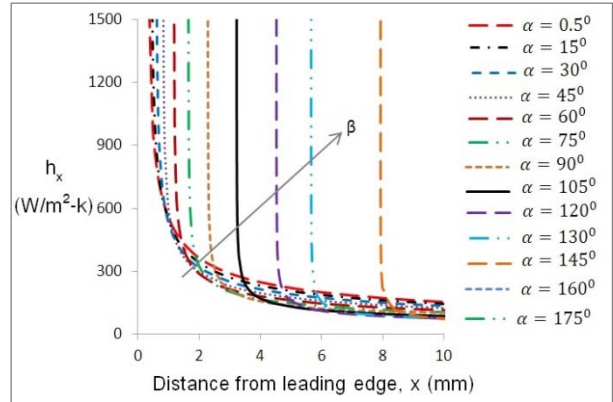


Fig.-6(b): Close View of Fig.-6(a)

Substituting value C_4 and $\Lambda(x)$ for $\alpha = 0.5^\circ$ from the **Table-1** to equation (21),

$$N_{ux} = 0.358 \left(R_{ex}^2 P_r^{1/3} \right) \left[1 - \left(\frac{x_0}{x} \right)^4 \right]^{-1/3} \quad (31)$$

If there is no insulation on the web surface, i.e. $x_0 = 0$ then equation (31) becomes,

$$N_{ux} = 0.358 \left(R_{ex}^2 P_r^{1/3} \right) \quad (32)$$

The numerical solution of heat transfer for flow over flat plate² is given by,

$$N_{ux} = 0.332 \left(R_{ex}^{\frac{1}{2}} P_r^{\frac{1}{3}} \right) \quad (33)$$

The equations (31) and (32) make very good agreement with Zhang, Yuwen (2010)⁸ and also with numerical solution of heat transfer over flat plate equation (33).

The variations of solutions of boundary layer thickness $\delta(x)$, momentum layer thickness $\delta_2(x)$, thermal boundary layer thickness $\delta_t(x)$ and heat transfer coefficient h_x from the Blasius's exact solutions or numerical solutions are within acceptable limit. Because solutions presented in this paper for 0.5° angle wedge surface are compared with Blasius's exact solutions for flat plate.

Boundary Layer Thickness $\delta(x)$, Thermal Boundary Layer Thickness $\delta_t(x)$ and Heat Transfer Coefficient h_x :

The relative characteristics of heat transfer coefficient h_x , boundary layer thickness $\delta(x)$ and thermal boundary layer thickness $\delta_t(x)$ for wedge angles $\alpha = 0.5^\circ$, $\alpha = 30^\circ$, $\alpha = 75^\circ$ and $\alpha = 120^\circ$ are shown in the Fig.-7(a) and Fig.-7(b).

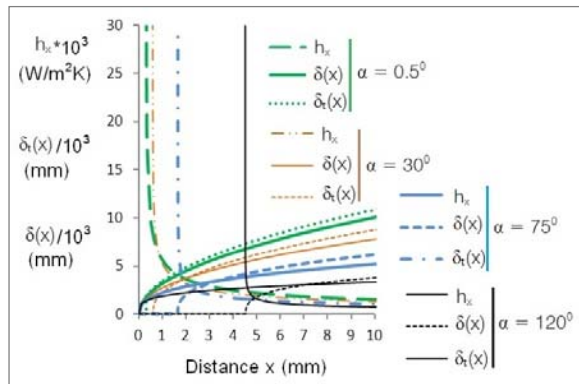


Fig.-7(a): Heat Transfer Coefficient, h_x ; Boundary Layer Thickness $\delta(x)$ and Thermal Boundary Layer Thickness $\delta_t(x)$.

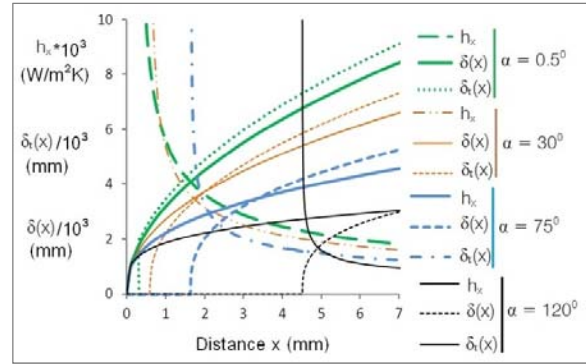


Fig.-7(b): Close View of Fig.-7(a).

From Fig.-7(a) and 7(b), it is observed that the boundary layer thickness $\delta(x)$ and thermal boundary layer thickness $\delta_t(x)$ increases gradually with decreasing of heat transfer coefficient h_x or with increasing of length of insulation.

CONCLUSION

From the analysis, presented in this paper the following conclusions are made:

- (1). The flow characteristics over wedge surface for wedge angle, $\alpha = 0.5^\circ$ are found consistence with Von Karman-Pohlhausen's integral methods for flat plate, as well as, with Blasius's exact solution for flat plate.
- (2). The boundary layer thickness and momentum thickness increase with increasing of wedge angle and boundary layer separates earlier with increasing of wedge angle to 105° and beyond.
- (3). The thermal boundary layer thickness and heat transfer coefficient decrease with increasing of length of insulation over wedge surface. In other words, length of insulation should be increased with increasing of wedge angle to keep the same amount of heat flux.
- (4). Von Karman-Pohlhausen's momentum integral method is the most simple and robust tool, which could be used to solve flow around complex or any arbitrary shaped object, as well as, it could be used for validation of test data and other solution methods.

ACKNOWLEDGMENT

The author would like to acknowledge Prof. Dr. A. Haji-Sheikh, UTA, Arlington, TX for his valuable suggestions and guidelines to complete this research work.

NOMENCLATURE

C_p	Specific heat of fluid at constant pressure
$\delta(x)$	Boundary layer thickness is function x
$\delta_2(x)$	Momentum thickness function of x
$\delta_t(x)$	Thermal boundary thickness function of x
$H(\xi)$	Universal function of ξ
U_∞	Free stream velocity
$U(x)$	Velocity of over wedge, $U(x) = c x^m$
c	Velocity constant
m	Exponent of velocity
$\Lambda(x)$	Shape factor and function of $\delta(x)$ and x
$K(x)$	Shape factor and function of $\delta_2(x)$ and x
q_w	Heat transfer through wall
h_x	Heat flux or coefficient of heat transfer
P_r	Prandtl number, $P_r = \frac{\mu C_p}{K}$
Re_{x_0}	Reynolds number at distance x_0
Re_x	Local Reynolds number at distance x
T_w	Temperature of the wedge surface
T_∞	Temperature of free stream fluid
k	Thermal conductivity
N_{ux}	Nusselt Number, $N_{ux} = \frac{h x}{k}$
$\frac{u}{U_\infty}$	Dimensionless ratio of velocity

GREEK SYMBOLS

μ	Absolute viscosity of fluid
ρ	Density of the fluid
ν	Kinematic viscosity of fluid ($\nu = \frac{\mu}{\rho}$)
β	Wedge angle factor
α	Wedge angle in degree
η	Dimensionless ratio, $\frac{y}{\delta(x)}$

$\xi = \frac{\delta_t(x)}{\delta(x)}$ ($\xi < 1$ for this particular situation)

REFERENCES

- [1] Anderson Jr., D. John, 2005, "Ludwig Prandtl's Boundary Layer", American Institute of Physics.
- [2] Schlichting, Dr. Hermann, 1979, "Boundary Layer Theory", McGraw Hill.
- [3] Schlichting, H., 1949, "Lecture Series—Boundary Layer Theory- Part I — Laminar flows", NACA.
- [4] Kackac, S. Sadik, 1994, "Convective Heat Transfer", CRC Press.
- [5] Eckert, E. R., and Drake, 1986, "Analysis of Heat and Mass Transfer", CRC Press.
- [6] Jiji, Latif M, 2006, "Heat Convection", Springer.
- [7] Helmy, K., A, 2001, "An Integral Method for the Solution of the Boundary Layer Equation for Power-Law MHD Fluid", Indian Journal of Pure Applied Math.
- [8] Zhang, Yuwen, 2010, "Integral solution of boundary layer equation", Thermal fluid central (www.thermalfluidscentral.org).
- [9] Basu, B., 2011, "Chaotic behavior in the flow along a wedge modeled by the Blasius equation", Nonlin. Processes Geophys.
- [10] Keshtkar, Mohammad, 2014, "The Falkner-Skan Flow over a Wedge with Variable Parameters", American-Eurasian Network for Scientific Information (AENSI).
- [11] Akcay, Mehmet, 2009, "Flow of power-law fluids over a moving wedge surface with wall mass injection", Springer-Verlag.
- [12] Ashwini, G., 2015, "Unsteady MHD Deceleration Flow over Wedge with Heat Generation/Absorption", American Institute of Science.
- [13] Padet, J, 2004, "Transient Convective Heat Transfer", Presented at 10th Brazilian

Congress of Thermal Sciences and Engineering.

[14] Butt, S., Adnan; Ali, Asif, 2013, "Thermodynamical Analysis of the Flow and Heat Transfer over a Static and a Moving Wedge", Hindawi Publishing Corporation.

[15] M. A. Seddeek, 2009, "Similarity Solutions for a Steady MHD Falkner-Skan Flow and Heat Transfer Over a Wedge Considering the effects of variable Viscosity and Thermal Conductivity", Applications and Applied Mechanics.

[16] Mukhopadhyay, Swati; Mandal, C, Iswar; 2014, "Boundary layer flow and heat transfer of a Casson fluid past a symmetric porous wedge with surface heat flux", Chinese Physical Society and IOP Publishing Ltd.

[17] Kousar, Nabeela; Liao, Shijun; 2010, "Series Solution of Non-similarity Boundary-Layer Flows Over a Porous Wedge", Springer Science and Business Media.

[18] Mutlag, A., A.; Uddin, J., Md.; 2013; "Heat Transfer Analysis for Falkner-Skan Boundary Layer Flow Past a Stationary Wedge with Slips Boundary Conditions Considering Temperature-dependent Thermal Conductivity", Sains Malaysiana.

[19] Bararnia, H.; 2012; "Flow analysis for the Falkner-Skan Wedge Flow"; Current Science.

[20] Weybume, W., David; 2010; "A Realistic Theoretical Model for Laminar Flow over a Flat Plate"; Air Force Research Laboratory, MA.

STUDY ON DIFFERENT PROPERTIES OF LOW DENSITY POLYETHYLENE COMPOSITES REINFORCED WITH PINEAPPLE LEAF FIBER

Habibur Rahman, Muhamad Borhan Uddin, Ruhul Amin Khan

Institute of Radiation and Polymer Technology (IRPT)

Bangladesh Atomic Energy Commission, Bangladesh

Corresponding Email: borhan_cef@yahoo.com

Abstract: *Pineapple leaf fiber (PALF) is one of the abundantly available agro wastes materials in Bangladesh. PALF reinforced low density polyethylene (LDPE) based composites were fabricated by compression molding with randomly oriented fiber loading 10-60% interval of 10%. In this study the influence of the addition of fiber contents on the mechanical properties such as tensile strength (TS) and tensile modulus (TM), Elongation at break (EB%), bending strength (BS) and bending modulus (BM), impact strength (IS). Based on the fiber loading 50/50% composite yielded better mechanical and other properties compared to the others. Impact strength increases with the increases of fiber loading in composite till 50% then it decrease in case of more fiber loading. To improve the compatibility between fiber and matrix, 50/50% PALF-LDPE composites were irradiated with gamma rays (Co-60) of doses varied from 2.5kGy to 10kGy where, composites irradiated with 7.5kGy dose delivered the best results.*

Keywords: *Composite, PALF, LDPE, Mechanical properties, gamma radiation*

INTRODUCTION

The word ‘composite’ means a substance which are the engineered materials made from two or more constituent materials, with significantly different physical and chemical properties and which remain distinct and separated at the microscopic level within the finished structure. These are becoming more and more important because of its increased utility. Considerable growth has been seen in the production and use of composites made from natural fiber in the construction and automotive industry, but application in other sectors has been limited. The unconventional fibers and other bio-renewable resources offer an almost limitless supply of renewable and potentially sustainable raw materials for the production of composites. Also the introduction of new fibers, with different bio-resins and additives may well result in an expansion in their use

into more diverse, and technically demanding application areas [1]. In the development of modern technology, Fiber Reinforced Polymer (FRP) composites play a vital role in day to day life due to its low cost, processing advantage of lower density and possessing good mechanical behavior over traditional reinforcement materials [2]. Renewable natural fibers such as oil palm, flax, and pineapple leaf can be used to acquire high performance polymer materials. The renewable natural fiber as reinforcement for polymer is a sustainable choice to the environment [3]. Composites materials are becoming very important in our daily life because of its growing utility. A composite poses the properties which could not be attained by either of the constituent materials alone. These are used in furniture, aerospace, aircraft, boats, automobiles, bridges, towers and light poles, pipelines, buildings, turbine

blades, roads, sports equipments and many other products. Various experiments are being made to upgrade the qualities of composites so that these may be further strong, lightweight, prolonged and economical to manufacture.

Composites are comprised of a hard material with discontinuous reinforcement that is embedded in a weaker, continuous matrix. The reinforcement provides strength and rigidity, in order to help to support the structural load [4]. The regulatory assessment and monitoring procedures as per the National/International guidelines are required to be reviewed wherever needed. They must be updated periodically depending upon the composition, intended usage conditions in order to promote clean processing, applications, biodegradation, recycling and reprocessing [5].

Natural fiber-reinforced (NFR) composites have many advantages as they are lightweight, biodegradable, renewable, economic, environmental friendly, and have reasonable strength and stiffness. In addition, comparing to glass fiber reinforced composites; the NFR composites reduce dermal and respiratory irritation during handling as well as reduce tool wear [6]. The disadvantages of natural fiber composites are lower durability than for synthetic fiber composites, but can be improved considerably with treatment, high moisture absorption, which results in swelling and lower strength in particular impact strength compared to synthetic fiber composites [7].

The composites are developed by using hand lay-up technique with heat compress machine. The developed composites are used to conduct the mechanical tests like tensile test, flexural test and bending test. The water uptake percentage and density of these composites also has been measured. The obtained values of mechanical properties of each volume ratio is tabulated and compared. The optimum volume ratio for which the

composite show better mechanical properties is concluded. Then the best ratio of PALF and LDPE composites were radiated by gamma ray and further the mentioned properties had been evaluated. In order to achieve the aim, the following objectives have been identified:

- To fabricate biodegradable, environment friendly, and low cost PALF-LDPE composites.
- To evaluate various properties, such as tensile, bending strength, impact strength of the composites.
- To evaluate the best effect of pineapple leaf fiber volume fraction on the above mentioned properties of the composites.
- Then the best ratio of PALF and LDPE is identified and radiated for better cohesion between fiber and polymer.
- Further the mentioned properties are evaluated to identify the increasing percentage of values.

METHODOLOGY

Tensile tests were conducted according to ASTM D638-01 using a Universal Test Machine (Model: H50KS-0404, HOUNSFIELD Series S, UK). In the present study impact strength of composites was conducted on notched mood according to ASTM D256 standard using a Universal Impact Tester (Hung Ta Instrument Co. Ltd. Taiwan), model-HT-8041B IZOD. The nominal energy of the pendulum was 150 kg-cm, lifting angle (α) was 150°, force torque (WR) was 80.811kg-cm. First of all, the specimen was clamped into the pendulum impact test fixture with the notched side facing the striking edge of the pendulum. Then the pendulum was released and allowed to strike through the specimen. It has been observed that gamma treated PALF/LDPE composites showed the best mechanical properties, such as tensile properties, bending properties and impact strength than untreated

composites. The PALF/LDPE composite field incorporated can easily be explored for better commercial decoration, structural and other associated applications. Due to the use of low-cost gamma treatment as a modification technique and good balance of mechanical properties, this type of composite can primarily be used for low-cost housing and automotive interior component applications.

RESULTS AND DISCUSSION

The reason for this distinct value is because at the composition of (PALF/LDPE) 50/50, a higher value of composite has resulted a high tensile strength due to the appropriate proportions of reinforced fiber and matrix polymer where bonding between these happened properly. Hence, it has held that the PALF firm and this affected their mechanical properties.

The introduction of 50wt-% fiber content in the LDPE matrix increased the tensile modulus by more than two times compared to the 10% fiber loading, which is attributed to the higher modulus of the PALF and LDPE ratio.

The increase in strength of the composites indicates an increase in the rigidity of PALF related to the restriction of the mobility in LDPE matrix due to the presence of fiber content. The high values of strength observed in these experiments may be due to the fair distribution of the PALF in the LDPE matrix resulting in fiber reinforced-LDPE matrix interaction.

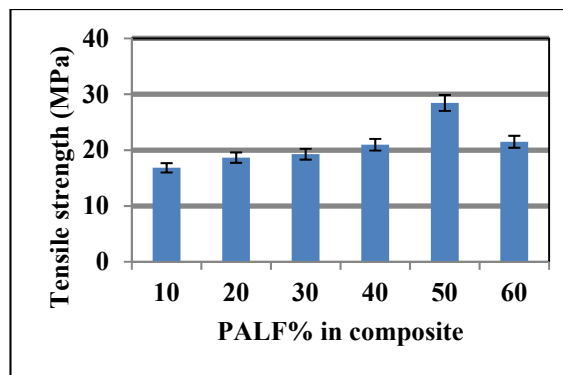


Figure 1: Tensile strength (MPa) of PALF/LDPE composites varying fiber loading

It can be clearly seen from the figure that values of BS composites were increased with the increase of PALF up to 50%. The maximum value of BS were found to be 78.42MPa for 50% PALF reinforced composite and further increasing of fiber content decreased the values.

Bending Modulus (BM) is another mechanical property of composites. It was measured as a function of PALF loading percentage in composite.

Izod impact strength of the PALF-LDPE shows increase in impact strength with filler loading, because of the increase of reinforcement fiber content in the composites. From the figure it was observed that values of IS of PALF/LDPE composites claimed linearly with the increase of fiber content up to 50% in composite.

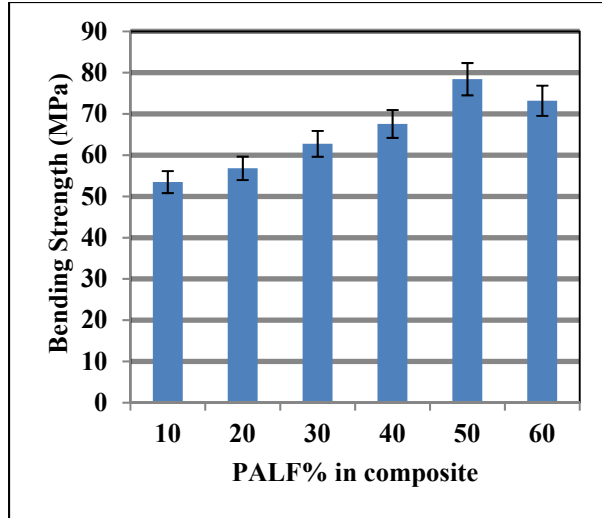


Figure 2: Bending Strength (MPa) of PALF/LDPE composites varying fiber loading

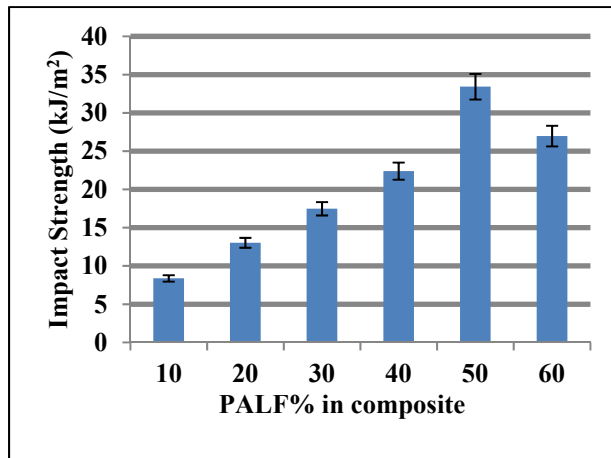


Figure 3: Impact strength (kJ/m²) of PALF/LDPE composites varying fiber loading

It is observed that mechanical and physical properties of PALF/LDPE composites increased with gamma radiation up to a certain dose and then decreased due to the two opposing phenomena, namely, photo

cross-linking and photo degradation that took place simultaneously under γ radiation. At lower doses, free radicals are stabilized by a combination reaction as a result photo cross-linking occurs. The higher the number of active sites generated on the polymeric substrate, the greater the grafting efficiency. But at higher radiation, the main chain may be broken down and polymer may degrade into fragments as a result mechanical and physical properties will decrease after certain gamma doses.

Tensile properties of the composites were found to be improved significantly after irradiation. TS, TM, IS, BS, BM and ρ of these composites increased maximum 35.34%, 16.01%, 32.94%, 26.17%, 26.87% and 8.85% respectively at 7.5kGy. But the elongation at break and water uptake percentage have been decreased the maximum 45.63% and 52% respectively in case of 7.5kGy due to radiation.

CONCLUSIONS

Based on the results of tensile strength, hardness and density, it can be concluded that the PALF/LDPE composite with the composition ratio of 50/50 has shown the best mechanical properties comparable to others composition ratios. However, for PALF/LDPE composites with PALF loading of less than 50% and more than 50% not appropriate for composite materials because comparatively it shows the lowers mechanical properties. Furthermore this type (50/50) of composite was irradiated with different doses of gamma ray. From this investigation it was found that tensile, bending and impact strength of composites were increased significantly after application of gamma radiation. In the 7.5 kGy dose showed better mechanical properties compared to the best for above properties. After radiation the

tensile strength, tensile modulus, elongation at break, bending strength, bending modulus, impact strength, water absorbency and density of 50/50 PALF/LDPE composites were found 38.49 MPa, 966.22 MPa, 36.17%, 98.94 MPa, 7313.93 MPa, 44.43 kJ/m², 9.33%, 1.23 gm/cc respectively in 7.50kGy dose. It revealed that gamma irradiation formed better cross-linking between PALF and LDPE matrix. Finally to summarize, the study has demonstrated the optimum fiber loading for peak performance is at 50 wt%. Fiber matrix interaction is well adhered and compatible with the radiation of gamma ray at this concentration of fiber of 7.5 kGy. PALF is widely accepted in textile sector and already used in our daily life materials but we attribute that further study will enhance the application in various other exiting products.

REFERENCES

- [1] Kesarwani, P., Jahan, S., & Kesarwani, K. (2015). Composites: Classification and its manufacturing process. *International Journal of Applied Research*, 1(9), 352-358.
- [2] Wang, W., Cai, Z., & Yu, J. (2008). Study on the chemical modification process of jute fiber, *Journal of Engineered Fibers and Fabrics*, 3(2), 1-11.
- [3] Abilash, N., Sivapragash, M. (2013). Environmental benefits of eco-friendly natural fiber reinforced polymeric composite materials. *International Journal of Application or Innovation in Engineering & Management (IJAIEEM)*, 2(1), 53 – 59.
- [4] Hull, D. & Clyne, T. W. (1996). An introduction to composite materials. Cambridge: *Cambridge University Press*, 67.
- [5] Sharma, V.P., Agarwal, V., Umar, S. & Singh, A. K. (2011). Polymer composites sustainability: environmental perspective, future trends and minimization of health risk. *2nd International Conference on Environmental Science and Development IPCBEE*, Singapore, 1(4), 259.
- [6] Arbelaiz, A., Fernandez, B., Ramos, J.A., Retegi, A., Llano-Ponte, R. & Mondragon, I. (2008). Mechanical properties of short flax fiber bundle/propylene composites: influence of matrix/ fiber modification, fiber content, water uptake and recycling. *Compos. Sci. Technology*, 65, 1582-1592.
- [7] Lee, B.H., Kim, H.J. & Yu, W.R. (2009). Fabrication of long and discontinuous natural fiber reinforced polypropylene bio-composites and their mechanical properties. *Fibers Polym*, 10(1), 83–90. Laboratory, MA.

MACHINABILITY STUDY OF A KEVLAR AND GLASS REINFORCED POLYESTER COMPOSITE UNDER DRY AND COMPRESSED AIR-COOLING CONDITION

Mohammad Shahadath Hossain*, Nikhil Ranjan Dhar

Department of Industrial and Production Engineering (IPE)

Bangladesh University of Engineering and Technology (BUET), Bangladesh

Corresponding Email: shahadath.hera@gmail.com

Abstract: Modern manufacturing industries are continuously seeking for products which will be light weight, robust, less costly and possess good quality in terms of surface finish and dimensional accuracy. To attain the needs, material engineers are constantly striving to develop new metal alloys as well as composite materials. Composite materials' light weight, high specific strength and high specific modulus are being regarded as some gifted properties which are largely facilitating their applications in different engineering sectors. High speed machining is often considered as an accurate manufacturing process for making fiber reinforced plastic (FRP) products. It is also established that with high cutting speed and feed productivity increases but high tool wear also takes place hence cost increases. It is found that compressed air-cooling environment has been very effective in machining FRPs when surface roughness and cutting force are taken into consideration. In this research work, turning operation has been performed on a hybrid composite i.e. Kevlar and glass reinforced polyester under both dry and compressed air-cooling condition. Investigation has been carried upon due to compare the performances of two machining environments. Cutting parameters in the machining process are cutting speed, feed and depth of cut and measured responses are surface roughness and cutting force.

Keywords: KFRP composites, GFRP composites, CFRP composites, Hybrid composites.

INTRODUCTION

Machining of fiber-reinforced plastic (FRP) materials has become very popular these days despite their relatively high cost. FRP composites pronounce a number of distinguished advantages over conventional engineering materials such as aluminum, steel etc. Among these high specific strength and high specific modulus are of great significance. They have found their applications in high-performance products

which need to be lightweight yet strong enough to work on harsh loading conditions such as aerospace components, automobiles, car bodies, portable bridges, offshore structures, containers, corrosion resistant goods [1]. Since, composite materials are inhomogeneous and anisotropic in nature and protrusion of fibers occurs during their machining, the desired surface finish is often harmed. During machining whenever the

cutting tool gets subjected to severe load fluctuations cutting flanks get damaged [2]. Again, Santhanakrishnam et al. [3] affirmed that a combination of plastic deformation, shearing and bending rupture would take place during machining of FRP composites. After performing face turning operation on glass fiber reinforced plastic (GFRP), carbon fiber reinforced plastic (CFRP) and Kevlar fiber reinforced plastic (KFRP) they found, CFRP gave a surface of better quality compared to other FRP composites. KFRP exhibited poor surface finish due to their higher toughness. Bhattacharya et al. [4] studied cryogenic machining of Kevlar composites and they concluded, with the increase in cutting force, surface roughness increased. The degrees of fiber pull out and fiber protrusion depended on various cutting parameters. Better surface quality was found under cryogenic condition even though tool wear slightly appeared to be of higher growth. Sonbaty et al. [5] performed drilling operation on GFR-epoxy composite. The drilling processes were carried out on epoxy resin and glass fiber reinforced epoxy composite (GFREC) with back plate. It was found that, for epoxy resin, increasing cutting speed had not any considerable effect on thrust force. On the other hand, torque decreased with increasing cutting speed. Isik [6] performed turning operation on Kevlar fiber reinforced plastic and found decreased surface roughness with increasing cutting speed whereas increased surface roughness with increasing feed rate. Controlled parameters such as cutting condition and non-controlled parameters such as work-piece non-homogeneity, tool wear, machine motion errors, chip formation and other random

disturbances; all have effects on surface roughness. It is proved that both controlled and non-controlled parameters cause relative vibrations in the cutting tool and work-piece. Gill et al. [7] performed machining operation in unidirectional glass fiber reinforced epoxy composite. Turning operation was done on a workpiece of diameter 42 mm and length 840 mm in both dry and wet environment. The cutting tool used in the experiment was carbide insert (K10). The objective of the experiment was to predict cutting force while cutting speed, feed rate, tool nose radius and tool rake angle were varied during the whole operation. Three levels of cutting speeds, three levels of feed rates, two nose radii and three different rake angles were used in the experiment. It was found that depth of cut was the major parameter that can be attributed to high cutting force. It was also found that the tangential, feed and radial force decreased with decrease in tool nose radius. The tangential, feed and radial force increased with decrease in tool rake angle. Shahrajabian and Farahnakian [8] performed drilling operation on CFRP with varying spindle speed, feed rate and point angle of the twist drill bit. The spindle speeds used in the experiment were 1250 rpm, 2625 rpm and 4000 rpm; while feed rates were 50 mm/min, 425 mm/min and 800 mm/min and point angles were 60° , 10° and 140° . The objective of the experiment was to determine optimal cutting parameters keeping surface roughness, thrust force and delamination constrained up to certain level. Response surface methodology (RSM) has been used coupled with genetic algorithm to determine the optimal condition. Minimum surface roughness ($R_a = 0.685 \mu\text{m}$) was achieved at

spindle speed of 4000 rpm, feed rate of 50 mm/min, tool angle point of 140° and the maximum surface roughness ($R_a = 2.542 \mu\text{m}$) was achieved at spindle speed of 1250 rpm, feed rate of 800 mm/min, point angle of 100° . The minimum delamination ($F_d = 1.02$) was achieved at spindle speed of 4000 rpm, feed rate of 50 mm/min, point angle of 100° , and the maximum delamination ($F_d = 2$) was achieved at spindle speed of 1250 rpm, feed rate of 800 mm/min, point angle of 140° . Kumar et al. [9] performed turning operation in glass fiber reinforced plastic using carbide (10) cutting tool where the process parameters selected for the study were tool nose radius, tool rake angle, feed rate, cutting speed, depth of cut, and cutting environment. The cutting speeds used in the experiment were 55.42 m/min, 110.84 m/min and 159.66 m/min, the feed rates were 0.05 mm/rev, 0.10 mm/rev and 0.15 mm/rev, chosen depth of cuts were 0.2 mm, 0.8 mm and 1.4 mm and the cutting environments were dry, wet and cooled. They found that the developed model based on the Taguchi approach and the utility concept was effective to achieve good performance characteristics. The depth of cut, cutting speed, and feed rate had a significant effect on the utility function based on the ANOVA significant process parameters for multiple performances. The optimal condition was cutting speed 110.84 m/min, feed rate 0.1 mm/rev and the depth of cut was 1 mm.

EXPERIMENTAL RESULTS

During the experimental investigation, the main cutting force was measured by a lathe tool dynamometer and the magnitude of the main cutting force was displayed by the charge amplifier in 'kg' unit. After performing the cutting operation surface

roughness was measured respectively using a Talysurf (Surtronic 3+ Roughness checker, Taylor Hobson, UK) using a sampling length of 4.00 mm.

Fig. 2.2 to Fig. 2.4 present the variation of main cutting force (P_z) with feed (S_o) whereas from Fig. 2.5 to Fig. 2.7 present the variation of main cutting force (P_z) with cutting speed (V_c) while machining FRP by coated carbide insert (SNMG) under both dry and compressed air-cooling condition. The figures from Fig.2.8 to Fig.2.10 present the variation of surface roughness (R_a) with feed (S_o) while from Fig.2.11 to Fig.2.13 present the variation of surface roughness (R_a) with cutting speed (V_c) while machining FRP by coated carbide insert (SNMG) under both dry and compressed air-cooling condition (CAC).



Nozzle position

Fig. 2.1 Photographic view of the experimental setup

DISCUSSION ON RESULTS

Cutting Force

According to the graphical representations of the variation of main cutting force with feed rate, it is evident that for almost every cutting condition; reasonable values of cutting force are found. Fig. 2.2 to Fig. 2.4 affirms that cutting force is increased with increased feed rate regardless of the machining environment. Combining both of the environments along with all the cutting conditions, compressed air cooling provided the best result under 213 m/min. cutting speed. One notable thing is that for increased depth of cut the value of the cutting force increased drastically.

2.1 Table. Experimental conditions

Machine Tool	:	KL-3280C/2000 (Sunlike Engine Lathe, 7.5 kW).
Work Material	:	Kevlar and glass reinforced Polyester
Dimension	:	300 mm length and 100 mm diameter.
Cutting Insert	:	Titanium nitride coated tungsten carbide (SNMG)
Cutting Tool Geometry	:	-6°, -6°, 6°, 6°, 15°, 75°, 0.8 (mm)

Process Parameters		
Cutting Speed, V_c	:	74, 106, 149 and 213 (m/min)
Feed, S_o	:	0.10, 0.12, 0.14 and 0.16 (mm/rev.)
Depth of cut, t	:	1.0, 1.5 and 2.0 (mm)
Machining Environment	:	Dry and Compressed air cooling (Air pressure- 20 Bar)

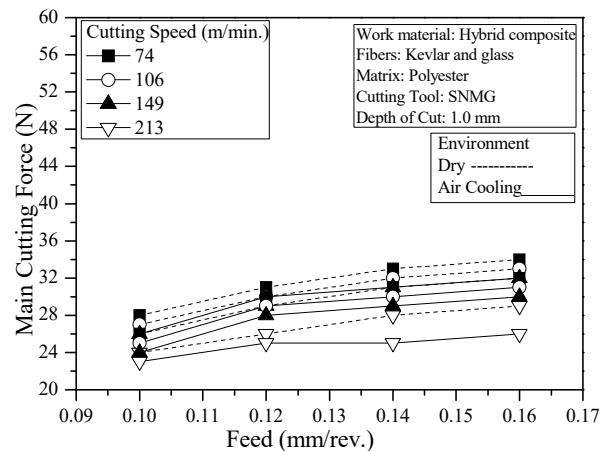


Fig 2.2 Variation of P_z with S_o at different V_c and 1.0 mm depth of cut under both dry and CAC condition

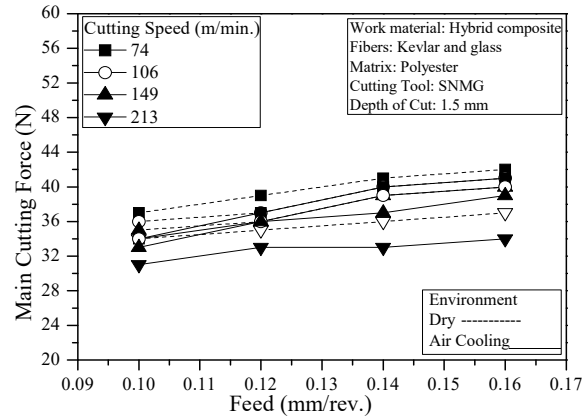


Fig. 2.3 Variation of P_z with S_o at different V_c and 1.5 mm depth of cut under both dry and CAC condition

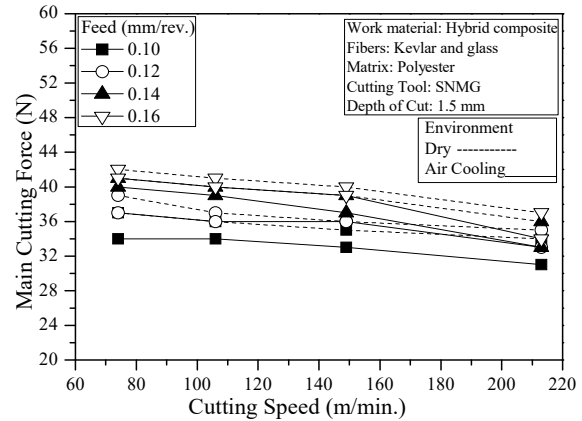


Fig. 2.6 Variation of P_z with V_c at different S_o and 1.5 mm depth of cut under both dry and CAC condition

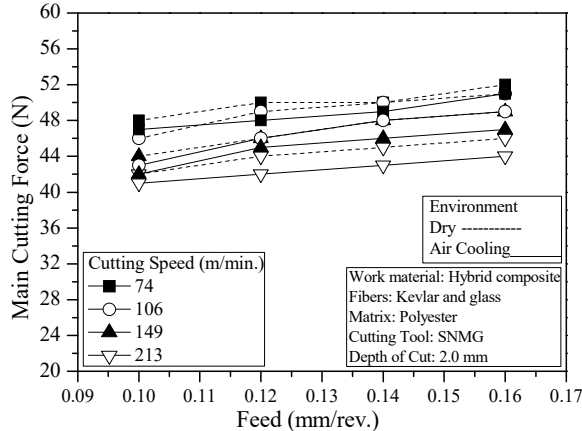


Fig. 2.4 Variation of P_z with S_o at different V_c and 2.0 mm depth of cut under both dry and CAC condition

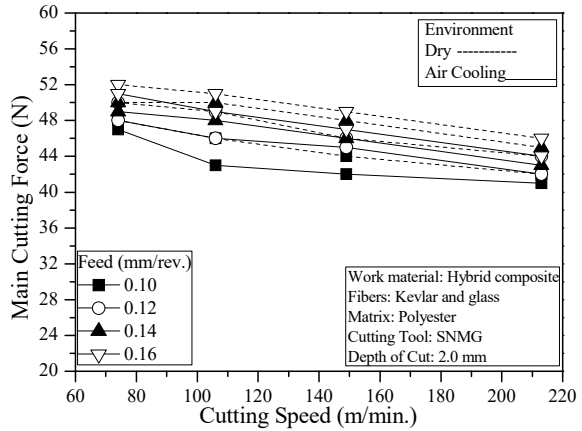


Fig. 2.7 Variation of P_z with V_c at different S_o and 2.0 mm depth of cut under both dry and CAC condition

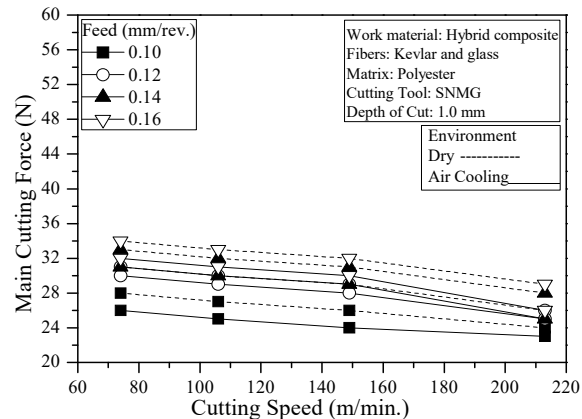


Fig. 2.5 Variation of P_z with V_c at different S_o and 1.0 mm depth of cut under both dry and CAC condition

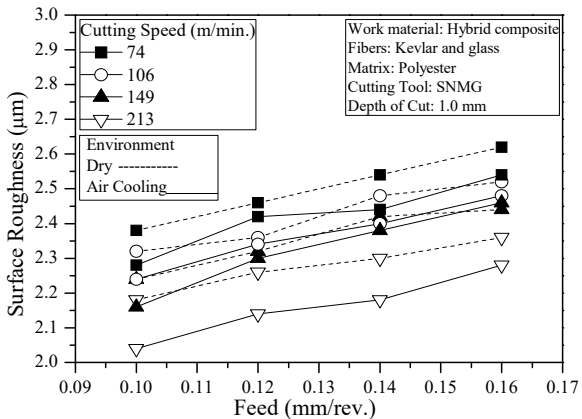


Fig. 2.8 Variation of R_a with S_o at different V_c and 1.0 mm depth of cut under both dry and CAC condition

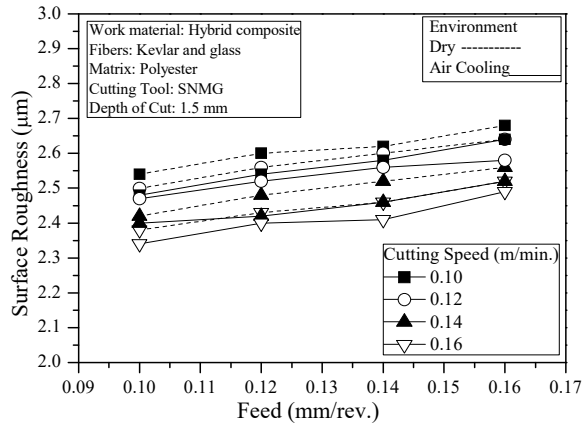


Fig. 2.9 Variation of R_a with S_0 at different V_c and 1.5 mm depth of cut under both dry and CAC condition

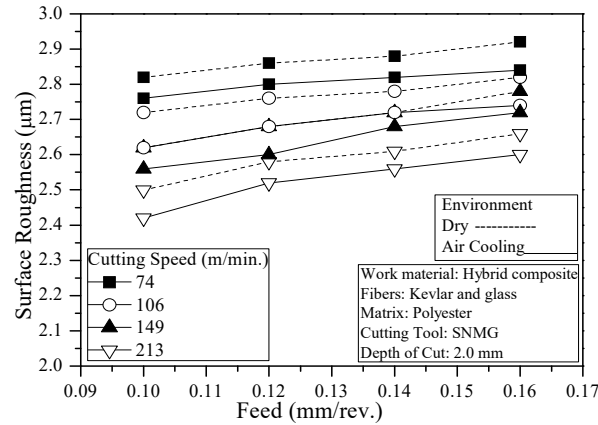


Fig. 2.10 Variation of R_a with S_0 at different V_c and 2.0 mm depth of cut under both dry and CAC condition

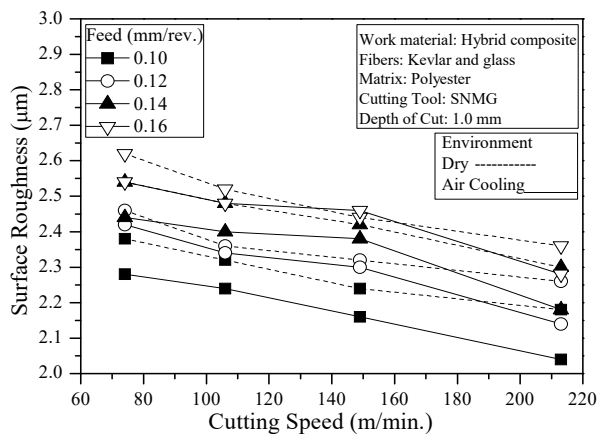


Fig. 2.11 Variation of R_a with V_c at different S_0 and 1.0 mm depth of cut under both dry and CAC condition

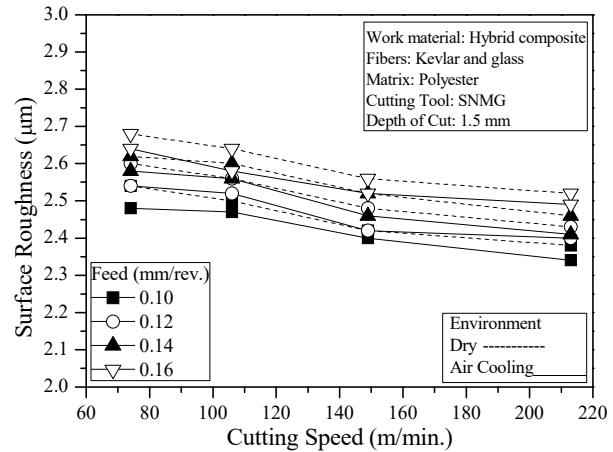


Fig. 2.12 Variation of R_a with V_c at different S_0 and 1.5 mm depth of cut under both dry and CAC condition

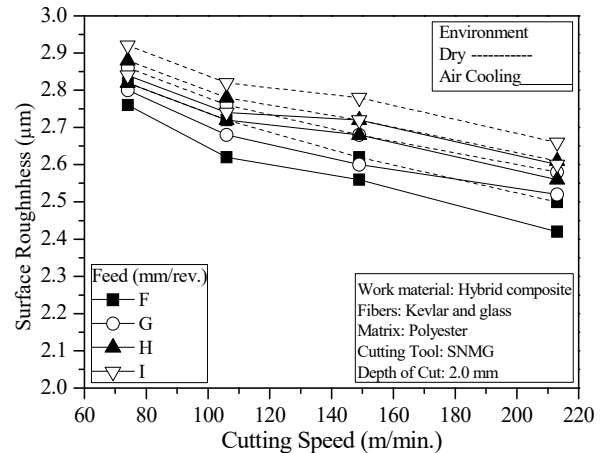


Fig. 2.13 Variation of R_a with V_c at different S_0 and 2.0 mm depth of cut under both dry and CAC condition

The reason is with increased depth of cut, the cutting tool penetrates more and removes more amount of material resulting increased cutting force. With varying feed and keeping the cutting speed constant, the optimal result has been obtained when the material is machined under cutting speed of 213 m/min. and feed rate of 0.10 mm/rev. and depth of cut of 1 mm.

The reason of increased cutting force with increased feed is that more amount of

material is cut per revolution of the workpiece and this requires higher amount of energy which ultimately leads to generate higher cutting force. Fig. 2.5 to Fig. 2.7 mainly displays the variation in main cutting force with varying cutting speed while feed rate is kept constant. It is evident as Fig. 2.6 to Fig. 2.8 present, for almost every cutting condition reasonable values of cutting force are found regardless of the machining environment. The trend of cutting force is mainly decreasing with increased cutting speed. In any machining process with the increase in cutting speed, shearing of the material becomes a very easy phenomenon and during the experiment the higher the cutting speed was the easier the shear became which generated lesser cutting force. When the results of two machining environments are compared to each other, it is found that compressed air-cooling condition has produced much better result than dry condition in terms of lower cutting force as presented in Fig. 2.2 to Fig. 2.7. The degree of improvement in cutting force under compressed cooling was not consistent in all the cutting conditions but lower cutting forces were found nonetheless. The reason behind improvement of cutting force under compressed air cooling is mainly due to the continuous cooling of chip tool interface. The process of forced cooling helped the machining process to get a lower value of cutting force as well as lesser temperature generation. Very few anomalies have been found during machining which do not conform to established knowledge to the machining of steels and FRP composites. Since, composite materials possess at least two different materials suggesting two materials that have completely different sets

of mechanical and thermal properties, complex phenomenon can often occur during their machining. Different materials can also have different amount of thermal expansion during machining which can lead to unexpected results sometimes. Result also depends on how well the work material has been manufactured such as blow hole can deteriorate the machining quality.

Surface Roughness

According to the graphical representations of variation of surface roughness in different cutting conditions, it is evident that for almost every cutting condition, reasonable surface roughness is found. From Fig. 2.8 to Fig. 2.10, it is evident that the trend of surface roughness is mainly increasing with increased feed regardless of the cutting speed and machining environment. The higher the feed, the more the tool covers an axial distance per revolution of the workpiece and wavy surfaces tend to produce. When the cutting speed is in concern, surface roughness is mainly decreased with increased cutting speed regardless the values of feed as shown in Fig. 2.11 to Fig. 2.13. Each one of the graphs of surface roughness vs. cutting speed is showing without any major deviation from the trend that with increasing cutting speed, surface roughness is decreased regardless of the feed rate. With increased cutting speed the deformation of the work material becomes very easy and in general a lower surface roughness is produced. In this investigation, lower surface roughness is found in general with increased speed and easy deformation of the work material might have worked as a reason. Few anomalies to the established knowledge of machining

metals have been found. Since composite material is inhomogeneous in and its fiber distribution may not be well distributed within the matrix so anomalies might have found during the machining operation. Again, another important thing to notice was the increase of surface roughness with the increase in depth of cut. It is obtained from the figures, maximum depth of cut produced maximum surface roughness, the reason might be that due to the increase in cutting force and higher tool wear also took place with increased depth of cut and deteriorated the surface quality.

CONCLUSIONS

- i. In depth investigation of the machinability of Kevlar and glass reinforced polyester has been performed under both dry and compressed cooling air condition from the perspectives of surface roughness and cutting force.
- ii. Surface roughness has been found to improve while the work was turned under compressed air cooling in comparison that of dry machining.
- iii. Different cutting condition provided different degrees of improvements. In terms of surface roughness, the best result was obtained under compressed air-cooled environment when the cutting speed was 213 m/min., feed 0.10 mm/rev. and depth of cut was 1 mm. The value of the surface roughness was 2.04 μm .
- iv. The maximum surface roughness was found under dry condition when the cutting speed was 74 m/min., feed 0.16 mm/rev. and depth of cut was 2 mm. The value of the maximum surface

roughness was found to be 2.92 μm .

- v. Cutting force was also substantially reduced while machined under compressed air-cooling environment as compared to that of dry machining.
- vi. Again, different cutting condition showed different degrees of improvements. When cutting force is in concern, the best result was found under compressed air-cooled environment when the cutting speed was 213 m/min., feed 0.10 mm/rev. and depth of cut was 1 mm. The value of the minimum cutting force was found to be 23 N.
- vii. The maximum main cutting force was found under dry condition when the cutting speed was 74 m/min., feed 0.16 mm/rev. and depth of cut was 2 mm. The value of the cutting force obtained was 52 N.

REFERENCES

- [1] Tandon, S., Jain, V.K., Kumar, P. and Rajurkar, K.P., Investigations into Machining of Composites, Precision Engineering, Vol. 12(4), pp.227–238, 1990
- [2] Santhanakrishnan, G., Krishnamurthy, R. and Malhotra S.K., High Speed Steel Tool Wear Studies in Machining of Glass-Fiber-Reinforced Plastics, Wear, Vol. 132(2), pp.327–336, 1989
- [3] Santhanakrishnan, G., Krishnamurthy, R. and Malhotra, S.K., Machinability Characteristics of Fiber Reinforced Plastics Composites, Journal of Mechanical Working Technology, Vol. 17, pp.195–204, 1988

- [4] Bhattacharya, D., Allen, M.N. and Mander, S.J., Cryogenic Machining of Kevlar Composites, Materials and Manufacturing Processes, Vol. 8(6), pp.631-651, 1993
- [5] Sonbaty E., Khashaba U.A. and Machaly T., Factors affecting the Machinability of GFR/Epoxy Composites, Composite Structures, Vol. 63(3-4), pp.329–338, 2004
- [6] Isik, B., Experimental Investigations of Surface Roughness in Orthogonal Turning of Unidirectional Glass-Fiber Reinforced Plastic Composites, International Journal of Advanced Manufacturing Technology, Vol. 37(1-2), pp.42-48, 2007
- [7] Gill, S.K., Gupta, M. and Satsangi, P.S., Prediction of Cutting Forces in Machining of Unidirectional Glass Fiber Reinforced Plastics Composite, Frontiers of Mechanical Engineering, Vol.8(2), pp.187-200, 2013
- [8] Shahrajabian, H. and Farahnakian, M., Modeling and Multi-Constrained Optimization in Drilling Process of Carbon Fiber Reinforced Epoxy Composite, International Journal of Precision Engineering and Manufacturing, Vol. 14(10), pp.1829-1837, 2013
- [9] Kumar, S., Meenu, Satsangi, P.S., Multiple-Response Optimization of Turning Machining By the Taguchi Method and the Utility Concept Using Uni-Directional Glass Fiber-Reinforced Plastic Composite and Carbide (K10) Cutting Tool, Journal of Mechanical Science and Technology, Vol. 27(9), pp.2829-2837, 2013

EFFECT OF DIFFERENT ANTIOXIDANTS ON PHYSIO-CHEMICAL PROPERTIES WITH BIODIESEL BLENDS

M.M. Rashed and Bengir Ahmed Shuvho

Centre for Energy Sciences, Department of Mechanical Engineering

Faculty of Engineering, University of Malaya

E-mail: rashed.duet31@gmail.com

Abstract: *Stability of biodiesel is an important parameter for biodiesel users in worldwide due to the increasing transportation system. The present study focused is on the effect of antioxidants (synthetic and aromatic) addition on Moringaolefera biodiesel. The changes in physico-chemical properties were observed for both synthetic and aromatic amine antioxidants. In this study, two aromatic antioxidants N, N'-diphenyl-1, 4-phenylenediamine (DPPD) and N-phenyl-1, 4-phenylenediamine (NPPD) and three synthetic antioxidants butylatedhydroxy toluene (BHT), tert-butylhydroxyquinone (TBHQ) and diphenylamine (DPA) were used. Due to the addition of both antioxidants to moringa biodiesel, the rate of change of kinematic viscosity and density were less comparing to pure biodiesel. The addition of antioxidants with biodiesel, oxidation stability of biodiesel increased significantly. It was also found that, for higher blends aromatic amine antioxidants (AAAO) shows better oxidation stability (OS) and for lower blends synthetic antioxidants (SAO) shows better OS. However, in some rare cases may act pro-oxidants. The outcome showed that by adding all the antioxidants to diesel fuel blends affected most of the crucial fuel properties.*

Keywords: *biodiesel, antioxidants, MB-5, MB-10, TBHQ, blends*

INTRODUCTION

In global prospects, use of biodiesel is growing rapidly. Meeting the growing demand of energy in a safe and environmentally responsible manner is one of the key challenges. Expanded ecological concern brought the nature of biodiesel and its mixes into core interest. Likewise it is crucial acknowledged that clean ignition in diesel engine can be proficient just by engine change combined with diesel fuel reformulation or added substance presentation [1, 2]. Biodiesel, is a blend of methyl esters with long chain unsaturated fats got from vegetable

oil and animal fats, and is same as trades diesel oil as far as fuel quality and burning properties [3, 4]. At the point when contrasted with petroleum diesel, it has various favorable circumstances, for example, biodegradability and non-poisonous quality [5]. Biodiesel additionally has an optimum combustion–emission profile, creating significantly low carbon monoxide, sulfur oxides, nitrogen hydride, particulate matter, and unburned hydrocarbons contrasted with the petroleum-based diesel [6]. Subsequently, it is gainful to utilize biodiesel as an optional fuel to substitute the petroleum-based diesel to

decrease air contamination and reduce the discharge of greenhouse gas [7]. On the other hand, a noteworthy downside with biodiesel is that it is more defenseless to oxidation corruption. Composition of fatty acid in oil is the main parameter to stabilize the biodiesel. In oxidation, the amount of unsaturation in oil is more prone [8]. For instance, it has been accounted for that the relative rate of oxidation of methyl ester of oleic corrosive (18:1) linoleic corrosive (18:2) & linolenic corrosive (18:3) is in the proportion of 1:12:25 [9, 10], that outcomes in the development of by item that expands viscosity of biodiesel [11]. The essential fatty acid chain stay same amid the procedure of transesterification of vegetable oils [12-14]. It has additionally been accounted for that the rate of oxidation is directly proportional to the quantity of bisallylic carbons present [15]. Oxidation is an intricate procedure, because of which the methyl ester gets transformed into a mixed of sorts including smaller chain unsaturated fat and aldehyde furthermore to high atomic weight species through oxidative polymerization. The initial step is the arrangement of free radical adjoining a twofold bond. Free radical being profoundly receptive responds with barometrical oxygen prompting arrangement of peroxy radical. By abstracting "H" from new unsaturated fat methyl ester, peroxy free radical gets settled and subsequently making new free radical. The procedure keeps bringing about the development of aldehyde liquor and carbonic corrosive [16]. In the indicated parent oil these reaction are quite pronounced because of the vicinity of antioxidants which get incompletely lost amid refining consequently decreasing the oxidation dependability [17].

The fuels stability can enhance by using different antioxidants concentration with different blends of biodiesel. A few previous studies have reported the impact of different antioxidant like synthetic [3, 18-25] but no researches have yet studied on the oxidation stability of biodiesel, density and viscosity with aromatic amine antioxidants. The aromatic amine AO was most beneficial for higher blends of biodiesel for long period of time. Be that as it may, constrained work has been done on the stability conduct of biodiesel mixes with pure diesel and in addition on the effect of antioxidant agents on storage of biodiesel/diesel mixes [26-31].

In this work, the storage stability of distinctive biodiesel mixes with automated diesel treat with different phenolic antioxidants agents were researched over a stockpiling time of 90 days. Investigation of fuel properties, for example, induction period, density, kinematic viscosity were produced using specimens taken from every capacity holder. The objective was to recognize the properly added substance which could essentially enhance the strength of biodiesel mixes over a long stockpiling period and to give a superior comprehension of the impact of capacity conditions on the nature of biodiesel mixes with diesel fuel.

EXPERIMENTAL PROCEDURE

Blending of biodiesel

MOME was mixed with diesel at 5%, 10%, 20%, 30%, and 40% by volume utilizing an attractive stirrer (model: IKA® C-MAG HS 7) at 2000 rpm for 30 min and a shaker (model: IKA® KS 130 fundamental) at 400

rpm for 30 min. Therefore, the physical properties of the biodiesel and its mixes were assessed according to the ASTM standards. Table 1. shows the physio-chemical properties of MOME and pure diesel.

Table 1. Physiochemical properties of MOME

Properties	Units	Standards	Pure Diesel	MOM E	ASTM D6751
Kinematic viscosity at 40°C	mm ² /s	ASTM D7042	3.2333	5.0537	1.9-6
Density at 40° C	kg/m ³	ASTM D7042	827.2	859.6	860-900
Flash point	°C	ASTM D93	68.5	150.5	>130
Cloud point	°C	ASTM D2500	8	19	-
Pour point	°C	ASTM D97	0	19	-
Cold filter plugging point	°C	ASTM D6371	5	18	-
Calorific value	MJ/kg	ASTM D240	45.304	40.052	-
Iodine value	g I/100g	EN 14111	-	77.5	120 max
Oxidation stability	h	EN ISO 14112	-	5.05	>3

Fatty acid and composition

Fatty acid composition of (*Moringa oleifera* methyl ester) MOME was measured by using gas chromatography (GC) (Agilent 6890 model, USA). Biodiesel sample 1μL was pushed into the GC adjusted with FID (flame Ionization Detector) and a BPX70 capillary column dimension (30m×0.25μm×0.32 mm inner diameter). Primary temperature was kept at 140.0°C for two minute and then temperature increase rate was 8.0°C/min to 165.0°C-192.0°C and lastly 8.0°C /min to 220.0°C kept this temperature five minute. During the operation the temperatures set at 140.0°C, 240.0°C, and 260.0°C for oven, injector and detector ports (DP) respectively. Carrier gas was helium with the linear velocity 24.4 cm/sec and column flow rate (1.10 mL/min) with head pressure 56.9 kPa. Table 2. Shows the FAC of MOME.

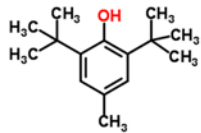
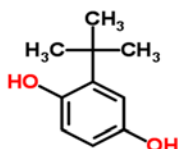
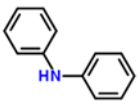
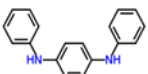
Table 2. Fatty acid composition (FAC) of MOME.

Sl. no.	Fatty acid	Molecular weight	Structure	Formula	MOME
1	Lauric	200	12:0	C ₁₂ H ₂₄ O ₂	0
2	Myristic	228	14:0	C ₁₄ H ₂₈ O ₂	0.1
3	Palmitic	256	16:0	C ₁₆ H ₃₂ O ₂	7.6
4	Palmitoleic	254	16:1	C ₁₆ H ₃₀ O ₂	1.2
5	Stearic	284	18:0	C ₁₈ H ₃₆ O ₂	5.8
6	Oleic	282	18:1	C ₁₈ H ₃₄ O ₂	74.1
7	Linoleic	280	18:2	C ₁₈ H ₃₂ O ₂	4.6
8	Linolenic	278	18:3	C ₁₈ H ₃₀ O ₂	0.2
9	Arachidic	312	20:0	C ₂₀ H ₄₀ O ₂	2.3
10	Eicosanoic	310	20:1	C ₂₀ H ₃₈ O ₂	1.3
11	Behenic	340	22:0	C ₂₂ H ₄₄ O ₂	2.8
12	other				0
Saturated					19.2
Monounsaturated					76.6
Polyunsaturated					4.3
Total					100

Use of Antioxidant (AO)

In this present study the two types of antioxidant are used one is synthetic antioxidant e.g. butylatedhydroxy toluene (BHT), tert-butylhydroxyquinone (TBHQ) and diphenylamine (DPA) and another one is aromatic antioxidant e.g. N, N'-diphenyl-1, 4-phenylenediamine (DPPD) and N-phenyl-1, 4-phenylenediamine (NPPD). Table. 3 represent the structure of different antioxidant and their chemical formula.

Table 3. Structure of different antioxidant and their chemical formula.

Name of Antioxidant	Structure	Chemical formula
BHT		C ₁₅ H ₂₄ O
TBHQ		C ₁₀ H ₁₄ O ₂
DPA		C ₁₂ H ₁₁ N
DPPD		C ₁₈ H ₁₆ N ₂

Condition of storage

The samples of biodiesel and diesel blend were kept in ambient temperature 18° C and 28° C in a closed brosil glass bottles volume of 500 ml. The bottle capacity was 1 liter and occupied by air. Every 10 days later the samples were taken out for taking data and find out the effect of antioxidant with blends.

Rancimat Method

To characterize the stability of biodiesel, there are various process to evaluate the behave of oxidation in biodiesel and its blends. This incorporate rancimat period acid value, density, kinematic consistency and so on. A large portion of the studies have utilized rancimat system [27, 32-35]. The present work is not quite the same as past studies around there since immaculate diesel or pure diesel is a low sulfur diesel detail and the mixes with biodiesel are in this manner moderately sulfur free, and till date next to no data is accessible on these mixes. Also, the oxidation steadiness was evaluated as far as rancimat period, kinematic viscosity and density. The rancimat period was measured utilizing 873 Rancimate" instrument made in Switzerland. The rancimat period was assessed likewise the standard strategy EN ISO 14112 "Oxidation dependability of fuel". The Rancimat strategy is a standout amongst the best strategies for deciding the oxidation dependability of biodiesel. For the Rancimat system at fig. 1 FAMES of the specimens are at first oxidized to peroxides as the essential oxidation items. To frame the optional oxidation items, the peroxides are totally decayed. The decay items are for the most part made out of formic corrosive, acidic corrosive, unstable natural mixes, and low

atomic weight natural acids. In this technique, the temperature extent is normally constrained to a greatest of 130 °C. In a brief analysis, the specimen is initially warmed at 110 °C. In this procedure, the oxidation of the example happens on the bubbles that the air is risen in the specimen, along these lines discharging some gasses with the air. In this manner, deionized water is gone in the flagon. The flagon is associated with a terminal to quantify the conductivity of the arrangement. The IP is measured in this procedure. For this situation, the IP is noted as the time at which the conductivity begins to increase rapidly. The constant estimation of conductivity results in an oxidation bend or curve. The indicated intonation in this bend or curve is known as the IP. Unpredictable acidic gasses, for example, formic corrosive, acidic corrosive, and different acids, are created by oxidation and ingested in water, which is the fundamental purpose behind the augmentation in conductivity and IP estimation. Rancimat period were measured for biodiesel and its mixes with business immaculate diesel fuel utilizing the strategy depicted previously. Every one of the determinations were performed in copy and the mean worth is accounted for with a mistake of $\pm 2\%$. Kinematic viscosity of biodiesel and its mixes, with and without different antioxidants, were measured at 40 °C and half torque by fungi lab expert series Viscometer, as indicated by ASTM-D 7042 system. Density of diesel tests were measured at 15 °C utilizing SVM 3000-programmed, by D 7042 system. All the information acquired were all around upheld [36] and inside of the reach according to ASTM standard.

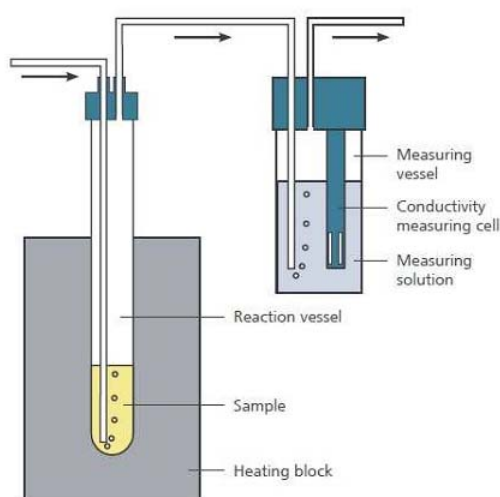


Figure 1. Rancimate method.

Antioxidant (AO) Screening

For screening reason the impacts of three (3) synthetic antioxidants (BHT, DPA TBHQ) and two (2) aromatic amine antioxidants were explored on pure MOME with diverse mixes. The study was finished by including 2 mL of 500 and 600 ppm (w/w) of every antioxidant agent in MOME. The changes of rancimat period with diverse concentration of antioxidant agents is indicated in Fig. 2. It is clear from the information acquired that the rancimat period gets upgraded, more with TBHQ when contrasted with different antioxidants and the best result is gotten with 600 ppm focus. BHT and DPPD were observed to be less effective contrasted with TBHQ, hence the effect of DPA and NPPD were minimum compare with other used antioxidants. For this reason DPA and NPPD were not utilized for further study. After the investigation is clear that synthetic antioxidants are more effective as compared aromatic amine antioxidant. Besides, viability of TBHQ intend that the antioxidant capacity

has an immediate connection with the quantity of $-OH$ gatherings present in the aromatic ring. As effective hydroxyl group effortlessly gives free proton to restrain the composition of free radicals or intrudes on the engendering of free radical and accordingly backs off the rate of oxidation [37, 38] and [39]. Low instability of BHT and DPPD likewise assumes a significant part in their poor execution [38]. In this way in light of the outcomes got from screening investigation of antioxidants substances, 600 ppm of TBHQ is utilized as the advanced focus for further studies for oxidation strength of diesel/biodiesel mixes.

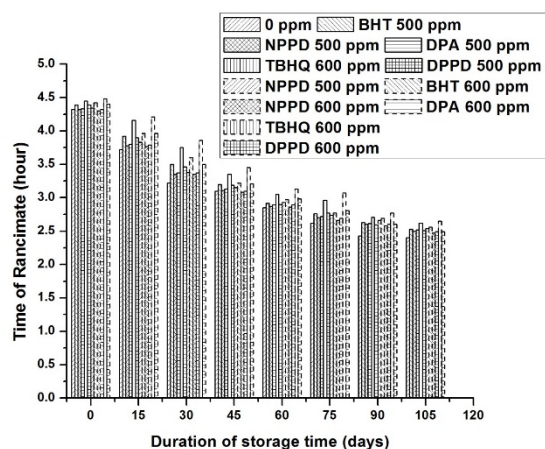


Figure 2. Measurement of oxidation stability (OS) of MOME with different concentration of AO.

Studies of different Stabilities

Taking into account screening test mixes demonstrated in Table 4 with two diverse concentration i.e. 600 ppm & 700 ppm of synthetic and aromatic amine antioxidant were inspected in point of interest by measuring their rancimat time, kinematic viscosity and density. At first, we examined oxidation stability of distinctive mixes without antioxidant for a particular interval

time of 90 days and the outcome uncovered that there is a number of connections between biodiesel concentration and stability. As biodiesel concentration enhance, biodiesel stability is found to diminishing as demonstrated in Fig. 3. Most extreme rancimat period is gotten with MB-5 and least with MB-40.

Table 4: Concentration of different antioxidants with different blends

Antioxidants	MB-5	MB-10	MB-20	MB-30	MB-40
BHT (Synthetic)	600 ppm	600 ppm	600 ppm	600 ppm	600 ppm
	700 ppm	700 ppm	700 ppm	700 ppm	700 ppm
TBHQ(Synthetic)	600 ppm	600 ppm	600 ppm	600 ppm	600 ppm
	700 ppm	700 ppm	700 ppm	700 ppm	700 ppm
DPPD(Aromatic)	600 ppm	600 ppm	600 ppm	600 ppm	600 ppm
	700 ppm	700 ppm	700 ppm	700 ppm	700 ppm

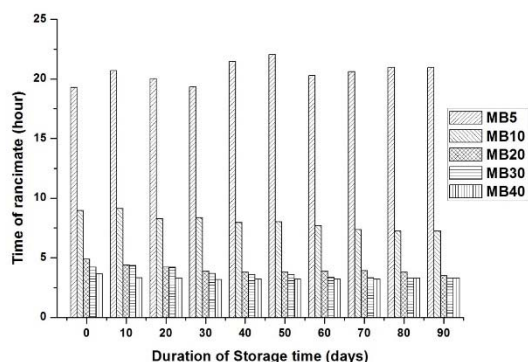


Figure 3. Impact of stabilities of different blends without AO.

RESULTS AND DISCUSSION

The following given graph Fig. 4, Fig. 5, Fig. 6, Fig. 7, Fig. 8, Fig. 9, Fig. 10, Fig. 11, Fig. 12, Fig. 13, Fig. 14 and Fig. 15, Fig. 16, Fig. 17 and Fig. 18 shows impact of various concentration of different antioxidants concentration on distinctive mixes MB-5, MB-10, MB-20, MB-30 and MB-40 as far as rancimat period, density and viscosity for period of 90 days.

Measuring the Rancimat period (RP) of diesel biodiesel blends with different AO concentration

Fig 4-8. shows execution of different specimens as far as RP. For JB-5 the optimize and remarkable execution was found with 600 ppm TBHQ with rancimat time of 47 h. With the same centralization of TBHQ enhancements were likewise seen in viscosity and additionally density similar trends was seen with JB-10. So for mixes with 5% and 10% biodiesel (MB-5 and MB-10) TBHQ was observed to be more fruitful than BHT and DPPD. This may be because of the appearance of two hydroxyl ($-OH$) community appended to aromatic ring. The activity of $-OH$ community is to give proton that hinder the create of free radical or interfere with spread of free radical therefore postpone the rate of oxidation. Additionally because of more electro antagonism TBHQ offers more destinations for form of complex between free radical and antioxidant radical for the stabilization of ester chain. The poor execution of BHT and DPPD can be because of their high volatility which causes their misfortune amid the investigation. For mixes with higher segment of biodiesel (MB-20, MB-30 and JB-40), the outcomes got are as opposed to those got with JB-5 and JB-10, thus the solidness execution of TBHQ was observed to be less than that of BHT, which may be because of pro-oxidant connection of TBHQ [21]. The reason may be credited to diverse structure of MOME when contrasted with non-polar hydrocarbon which may associate with the exceedingly upset polar phenol gathering of BHA to diminish their AO abilities.

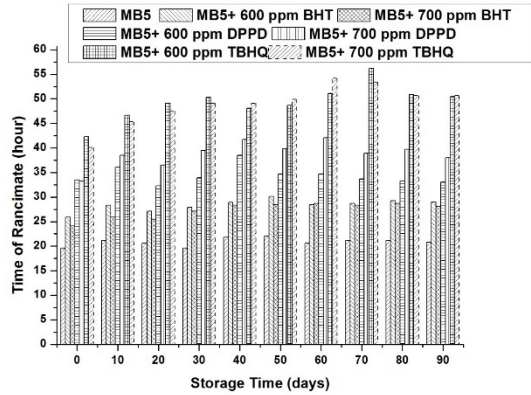


Figure 4. Impact of induction period (IP) of MB-5 with different AO concentration

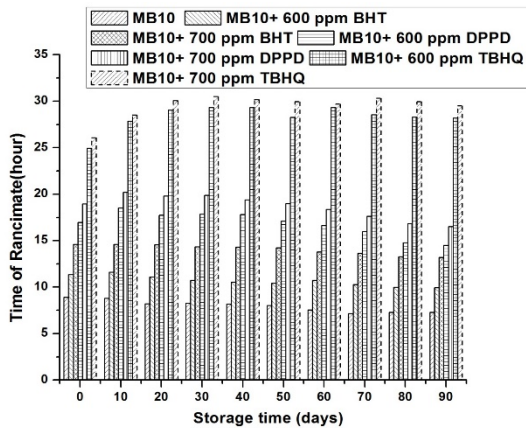


Figure 5. Impact of induction period (IP) of MB-10 with different AO concentration

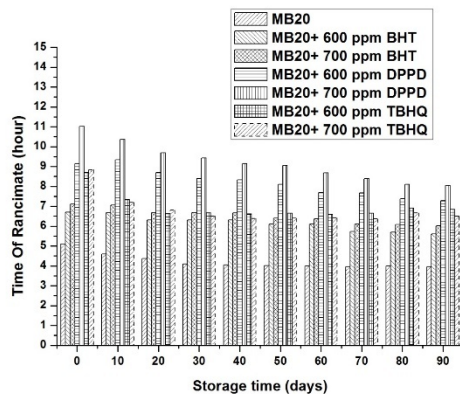


Figure 6. Impact of induction period (IP) of MB-20 with different AO concentration

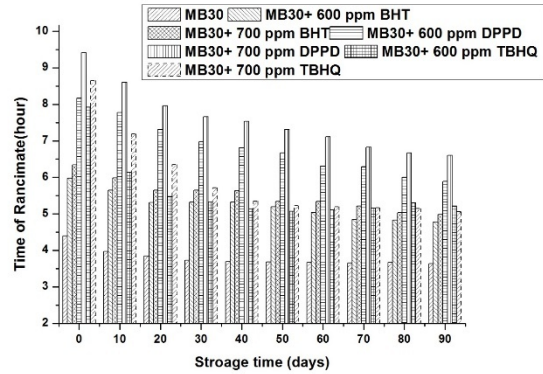


Figure 7. Impact of induction period (IP) of MB-30 with different AO concentration

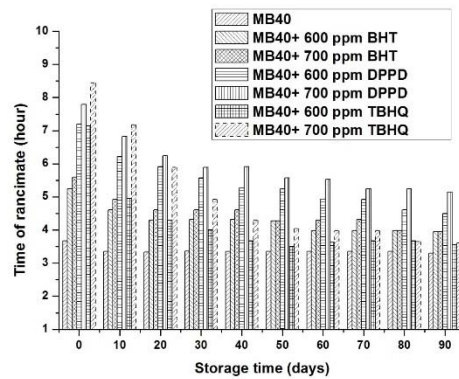


Figure 8. Impact of induction period (IP) of MB-40 with different AO concentration

Measuring the Density of diesel biodiesel blends with different AO concentration

Density estimation is a property for creating sufficient storage techniques for diesel biodiesel mixes [40, 41]. In diesel biodiesel mixes the density of fuel enhance with enhancing quantity of biodiesel in the blend. The density of the considerable number of mixes was seen limit of range said by standard ASTM-D 7042. The starting value range of density for net biodiesel blends (MB5, MB10, MB20, MB30 and MB40) was observed to be 831.87 kg/m^3 - 849.77 kg/m^3 and the average starting density limit of 838.56 kg/m^3 whilst as last density grade for

the equal were limit from 833.86 kg/m^3 with an average of 840.28 kg/m^3 .

Correspondingly, by adding aromatic and amine antioxidant with various blends of biodiesel were also monitored and the outcomes are focused from fig 9-13. For the MB10 blends the starting density with antioxidants range from 831.63 kg/m^3 to 833.42 kg/m^3 with a mean value of 832.16 kg/m^3 , on the other hand MB-30, the initial density limit 845.16 kg/m^3 to 847.23 kg/m^3 and the MB-40, ranged 849.85 kg/m^3 to 852.21 kg/m^3 . By adding synthetic and aromatic amine antioxidant shows the optimize density with the increase storage duration of biodiesel. By comparing with synthetic and aromatic antioxidant, synthetic antioxidant shows better property.

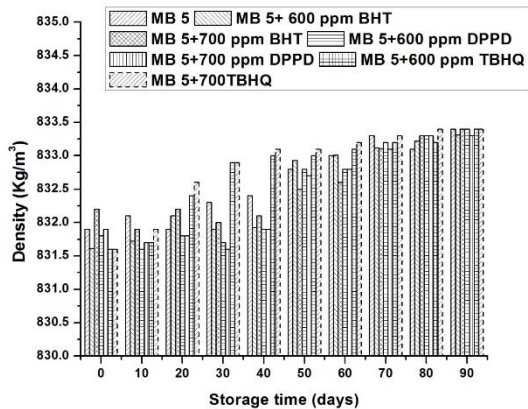


Figure 9. Impact of density MB-5 with different AO concentration

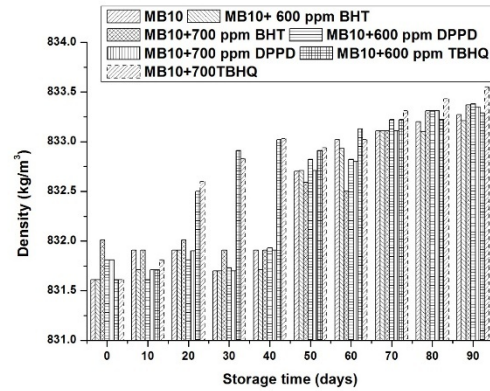


Figure 10. Impact of density MB-10 with different AO concentration

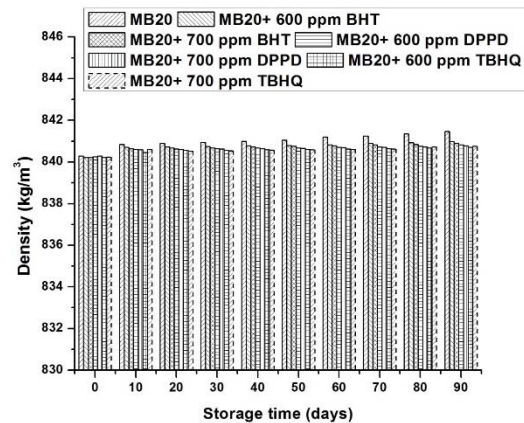


Figure 11. Impact of density MB-20 with different AO concentration

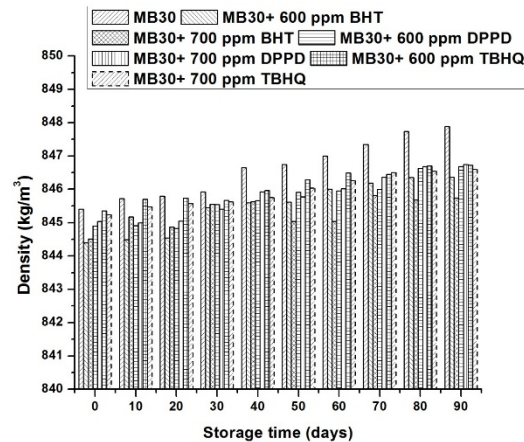


Figure 12. Impact of density MB-30 with different AO concentration

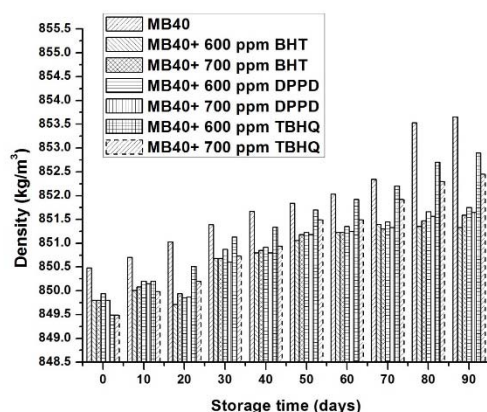


Figure 13. Impact of density MB-40 with different AO concentration

Measuring the kinematic viscosity of diesel biodiesel blends with different AO concentration.

Fig. 14-18 demonstrate the effect of viscosity with and without two different categories antioxidants SAO (synthetic antioxidant) and AAAO (aromatic amine antioxidant) and the summarized the outcomes with the period of 90 days. During the storage of biodiesel over period of 90 days, the viscosity increase with the increasing blends and this increase is in marginal. In normally, the viscosity increase, by formatting the oxidized products and which lead to the sediments and gums formation [42]. For this present study there is no degradation products formation of biodiesel mixes. Long term storage, greater temperature, direct expose to daylight are the crucial parameter for formation of oxidation products as well as the affect the viscosity in the blends. From the above figure it is seen that the primary kinematic viscosity for pure blends (MB-5, MB-10, MB-20, MB-30 and MB-40) values ranged $2.90 \text{ mm}^2/\text{s}$ to $3.46 \text{ mm}^2/\text{s}$ and the average value $3.14 \text{ mm}^2/\text{s}$ for the period of 90 days. On the other hand, last

results of these blends value range $2.96 \text{ mm}^2/\text{s}$ to $3.27 \text{ mm}^2/\text{s}$. Similarly, with the addition different concentration of two different categories AO and investigated the effect of these antioxidants with different blends of biodiesel. It is point out noted that, the starting value range of all blends of moringa biodiesel with diesel $2.93 \text{ mm}^2/\text{s}$ to $3.47 \text{ mm}^2/\text{s}$ and the final outcomes value ranged $3.01 \text{ mm}^2/\text{s}$ to $3.54 \text{ mm}^2/\text{s}$. over all the synthetic antioxidants with blend shows lower viscosity compare with AAAO. TBHQ shows the optimum results compare with DPPD and BHT.

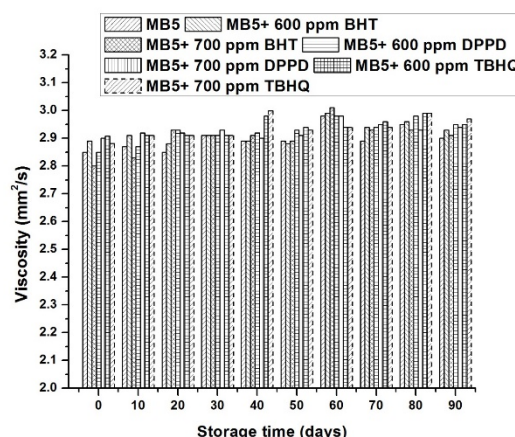


Figure 14. Impact of viscosity MB-5 with different AO concentration

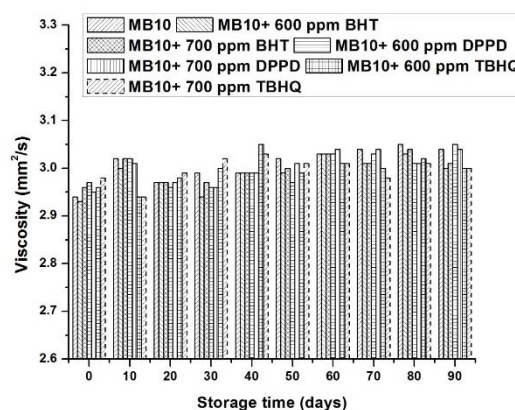


Figure 15. Impact of viscosity MB-10 with different AO concentration

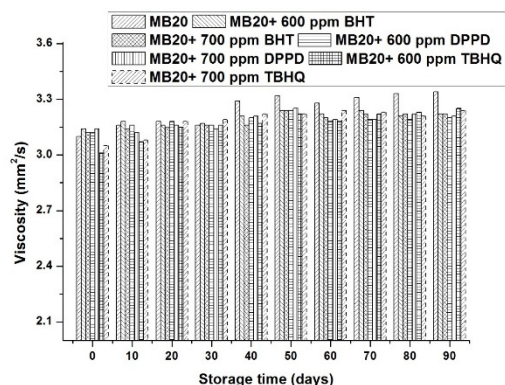


Figure 16. Impact of viscosity MB-20 with different AO concentration

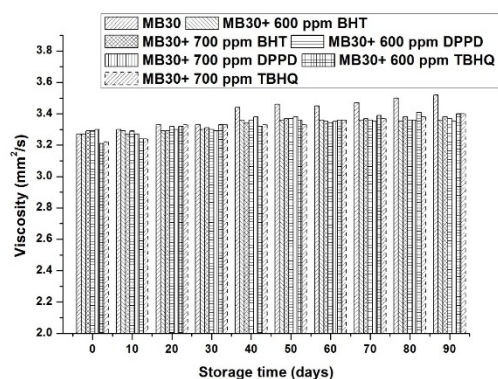


Figure 17. Impact of viscosity MB-30 with different AO concentration

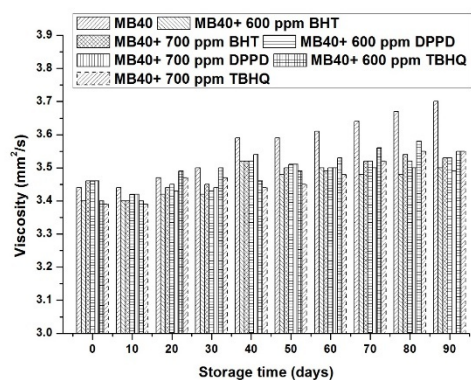


Figure 18. Impact of viscosity MB-40 with different AO concentration

CONCLUSION

Present study investigated the two categories of antioxidant of SAO (BHT, TBHQ, DPA) and AAAO (DPPD, NPPD) with different concentration and with the different proportion of moringa biodiesel (MB-5, MB-10, MB-30, MB-40) blends (%vol.) to determine the optimum storage stability of biodiesel over the period of 90 days. From the outcome results shows that, among both of five antioxidant TBHQ, BHT and DPPD shows better stability in neat methyl ester, on the other hand, DPA and NPPD shows lower performance on the stability compare with rest antioxidant. The addition of antioxidant led to important difference in density and limited effect in kinematic viscosity. A remarkable correlation was found with addition of antioxidant with the stability of biodiesel blends and with number of blends. Hence, the stability of biodiesel decreases with the increase of biodiesel blends. From this investigation, this investigation showed, pure lower biodiesel blends (MB-5 and MB-10) with synthetic antioxidant (TBHQ) shows most effective antioxidant among these antioxidant as well as compare with AAAO (DPPD). But, for higher blends (MB-20, MB-30, and MB-40), AAAO (DPPD) was found more effective compare to SAO. Moreover, SAO shows better stability over the period of time.

ACKNOWLEDGMENT

The authors would like to thank University of Malaya for financial support through High Impact Research grant titled: "Development of alternative and renewable energy carrier (DAREC)" UM.C/HIR/MOHE/ENG/60.

REFERENCES

- [1] Banerjee A, Chakraborty R. Parametric sensitivity in transesterification of waste cooking oil for biodiesel production—a review. *Resources, Conservation and Recycling*. 2009;53:490-7.
- [2] He B-Q, Shuai S-J, Wang J-X, He H. The effect of ethanol blended diesel fuels on emissions from a diesel engine. *Atmospheric Environment*. 2003;37:4965-71.
- [3] Rashed MM, Kalam MA, Masjuki HH, Rashedul HK, Ashraful AM, Shancita I, et al. Stability of biodiesel, its improvement and the effect of antioxidant treated blends on engine performance and emission. *RSC Advances*. 2015;5:36240-61.
- [4] Ulrich A, Wichser A. Analysis of additive metals in fuel and emission aerosols of diesel vehicles with and without particle traps. *Analytical and Bioanalytical Chemistry*. 2003;377:71-81.
- [5] Leung DY, Wu X, Leung M. A review on biodiesel production using catalyzed transesterification. *Applied energy*. 2010;87:1083-95.
- [6] Zheng S, Kates M, Dubé M, McLean D. Acid-catalyzed production of biodiesel from waste frying oil. *Biomass and Bioenergy*. 2006;30:267-72.
- [7] Patil PD, Deng S. Optimization of biodiesel production from edible and non-edible vegetable oils. *Fuel*. 2009;88:1302-6.
- [8] Dunn RO. Antioxidants for improving storage stability of biodiesel. *Biofuels, Bioproducts and Biorefining*. 2008;2:304-18.
- [9] Gunstone FD, Hilditch TP. The union of gaseous oxygen with methyl oleate, linoleate, and linolenate. *Journal of the Chemical Society (Resumed)*. 1945:836-41.
- [10] Igbokwe JO, Nwifo OC, Nwaiwu CF. Effects of blend on the properties, performance and emission of palm kernel oil biodiesel. *Biofuels*. 2015:1-8.
- [11] Ramos MJ, Fernández CM, Casas A, Rodríguez L, Pérez Á. Influence of fatty acid composition of raw materials on biodiesel properties. *Bioresource technology*. 2009;100:261-8.
- [12] Smith MB, March J. *March's advanced organic chemistry: reactions, mechanisms, and structure*: John Wiley & Sons; 2007.
- [13] Ramesha D, Bangari AS, Rathod CP, Chaitanya R S. Combustion, performance and emissions characteristics of a biogas fuelled diesel engine with fish biodiesel as pilot fuel. *Biofuels*. 2015:1-11.
- [14] Xin J, Saka S. Test methods for the determination of biodiesel stability. *Biofuels*. 2010;1:275-89.
- [15] Cosgrove JP, Church DF, Pryor WA. The kinetics of the autoxidation of polyunsaturated fatty acids. *Lipids*. 1987;22:299-304.
- [16] Jain S, Sharma M. Study of oxidation stability of *Jatropha curcas* biodiesel/diesel blends. *Int J Energy Environ*. 2011;2:533-42.
- [17] Rawat DS, Joshi G, Lamba BY, Tiwari AK, Mallick S. Impact of additives on storage stability of Karanja (*Pongamia Pinnata*) biodiesel blends with conventional diesel sold at retail outlets. *Fuel*. 2014;120:30-7.
- [18] Schober S, Mittelbach M. The impact of antioxidants on biodiesel oxidation stability. *European Journal of Lipid Science and Technology*. 2004;106:382-9.
- [19] Dunn RO. Effect of antioxidants on the oxidative stability of methyl soyate (biodiesel). *Fuel Processing Technology*. 2005;86:1071-85.
- [20] Ryu K. The characteristics of performance and exhaust emissions of a diesel engine using a biodiesel with antioxidants. *Bioresource technology*. 2010;101:S78-S82.
- [21] Fattah IR, Masjuki H, Kalam M, Mofijur M, Abedin M. Effect of antioxidant on the performance and emission characteristics of a diesel engine fueled with palm biodiesel blends. *Energy Conversion and Management*. 2014;79:265-72.
- [22] Fattah IR, Kalam M, Masjuki H, Wakil M. Biodiesel production, characterization,

engine performance, and emission characteristics of Malaysian Alexandrian laurel oil. *Rsc Advances*. 2014;4:17787-96.

[23] Tang H, De Guzman RC, Salley SO, Ng SK. The oxidative stability of biodiesel: Effects of FAME composition and antioxidant. *Lipid Technology*. 2008;20:249-52.

[24] Shahabuddin M, Kalam M, Masjuki H, Bhuiya M, Mofijur M. An experimental investigation into biodiesel stability by means of oxidation and property determination. *Energy*. 2012;44:616-22.

[25] Chen Y-H, Chen J-H, Luo Y-M, Shang N-C, Chang C-H, Chang C-Y, et al. Property modification of jatropha oil biodiesel by blending with other biodiesels or adding antioxidants. *Energy*. 2011;36:4415-21.

[26] Karavalakis G, Karonis D, Stournas S. Evaluation of the oxidation stability of diesel/biodiesel blends using the modified rancimat method. *SAE International Journal of Fuels and Lubricants*. 2009;2:839-49.

[27] Knothe G. Some aspects of biodiesel oxidative stability. *Fuel Processing Technology*. 2007;88:669-77.

[28] Domingos AK, Saad EB, Vechiatto WWD, Wilhelm HM, Ramos LP. The influence of BHA, BHT and TBHQ on the oxidation stability of soybean oil ethyl esters (biodiesel). *Journal of the Brazilian Chemical Society*. 2007;18:416-23.

[29] Xin J, Imahara H, Saka S. Kinetics on the oxidation of biodiesel stabilized with antioxidant. *Fuel*. 2009;88:282-6.

[30] Karavalakis G, Hilari D, Givalou L, Karonis D, Stournas S. Storage stability and ageing effect of biodiesel blends treated with different antioxidants. *Energy*. 2011;36:369-74.

[31] Lamba BY, Joshi G, Tiwari AK, Rawat DS, Mallick S. Effect of antioxidants on physico-chemical properties of EURO-III HSD (high speed diesel) and Jatropha biodiesel blends. *Energy*. 2013;60:222-9.

[32] Obadiah A, Kannan R, Ramasubbu A, Kumar SV. Studies on the effect of antioxidants on the long-term storage and oxidation stability of Pongamia pinnata (L.) Pierre biodiesel. *Fuel Processing Technology*. 2012;99:56-63.

[33] Saldaña MD, Martinez-Monteagudo SI. Oxidative stability of fats and oils measured by differential scanning calorimetry for food and industrial applications: INTECH Open Access Publisher; 2013.

[34] Nascimento JA, Araújo KL, Epaminondas PS, Pontes AL, Souza AL, Queiroz N, et al. Ethanolics extracts of Moringa. *Journal of Thermal Analysis and Calorimetry*. 2014;117:265-8.

[35] Mittelbach M, Schober S. The influence of antioxidants on the oxidation stability of biodiesel. *Journal of the American Oil Chemists' Society*. 2003;80:817-23.

[36] Mofijur M, Masjuki HH, Kalam MA, Rasul MG, Atabani AE, Hazrat MA, et al. Effect of Biodiesel-diesel Blending on Physico-chemical Properties of Biodiesel Produced from Moringa Oleifera. *Procedia Engineering*. 2015;105:665-9.

[37] De Guzman R, Tang H, Salley S, Ng KYS. Synergistic effects of antioxidants on the oxidative stability of soybean oil- and poultry fat-based biodiesel. *JAOCs, Journal of the American Oil Chemists' Society*. 2009;86:459-67.

[38] Liang YC, May CY, Foon CS, Ngan MA, Hock CC, Basiron Y. The effect of natural and synthetic antioxidants on the oxidative stability of palm diesel. *Fuel*. 2006;85:867-70.

[39] Karavalakis G, Stournas S. Impact of antioxidant additives on the oxidation stability of diesel/biodiesel blends. *Energy and Fuels*. 2010;24:3682-6.

[40] Alptekin E, Canakci M. Determination of the density and the viscosities of biodiesel-diesel fuel blends. *Renewable Energy*. 2008;33:2623-30.

[41] Geller DP, Adams TT, Goodrum JW, Pendergrass J. Storage stability of poultry fat and diesel fuel mixtures: Specific gravity and viscosity. *Fuel*. 2008;87:92-102.

[42] Das LM, Bora DK, Pradhan S, Naik MK, Naik SN. Long-term storage stability of biodiesel produced from Karanja oil. *Fuel*. 2009;88:2315-8.

PRODUCTIVITY IMPROVEMENT OF GRID CASTING IN A BATTERY MANUFACTURING COMPANY - A CASE STUDY

Raihanul Haq and Abdullahil Azeem*

Department of Industrial and Production Engineering

Bangladesh University of Engineering and Technology, Dhaka-1000, Bangladesh

*Corresponding email: aazeem.05@gmail.com

Abstract: Productivity is the key important factor to every industry as it helps quick response to customer demand as well as optimizes the usages of resources. Utilization of the properly allocated resources leads to better productivity and enhances the efficiency as well as effectiveness. Grid is considered the core of the battery industry. So, focusing on this critical component by improving its productivity is the main concern of the related industry. Improved efficiency bears a positive impact on the costs of goods manufactured, as same output is produced consuming less input or provides same inputs to produce more output. Kaizen events are sometimes referred to as rapid improvement tools. It involves small groups of individuals in the company that are brought together to address a particular area. The present study focuses on improving grid casting productivity and reducing the problems related to low productivity and efficiency in the production arena. Other sections regarding plate preparation are also highlighted for subsequent observation. Capacity study of individual processes and production procedure have also been considered for further improvement.

Key Words: Productivity Improvement, Kaizen, Optimization, Resource Utilization.

INTRODUCTION

In today's increasingly competitive world, it is important to improve continuously, manufacturing or service industry. Manufacturing industry is one of the sectors which can takes turns under all types of economic systems such as free market economy and collectivist economy. All of the products generated is competing to gain demand and satisfaction from customers. Dealing with continuous competition, company not only needs to produce quality products but also excellence in production systems. At the present stage of economic development, one of the main components of successful industrial organizations is planning productivity. Study of the productivity growth is becoming more important against a backdrop of market relations, because it allows company to stay competitive on the market and strengthen the social component in the development of society. The term productivity can be used to examine efficiency and effectiveness of any activity conducted in an economy, business, government or by individuals. Efficiency, effectiveness and productivity can also be evaluated for performance, business in service sector. Increased productivity reduces the cost of work on the production unit or an increase in output and prevent waste. Productivity is also confused with terms like efficiency and effectiveness and these terms are wrongly considered synonymous to productivity. Efficiency and effectiveness are two different terms. Productivity becomes the dominant issues in the

market place where customer demand is high and are willing to pay more for what they required in timely manner.

The main intention is to study the current capacity, analyze it to find areas of improvement, identify the flaws and make an improvement proposal to meet the forecasted increase in demand and improve the productivity in an industry of battery manufacturing production floor. This case study presents the current performance of outputs and capacity of the plant calculated using continuous data collected in shop floor. In each workstation the processing time and pattern is different and various industrial engineering technique and tools is implementing in this study in order to investigate and recommend actions. Different organizations within the same industry have different strengths and weaknesses and choose to compete in different ways. Dissimilar production "systems" have altered operating characteristics and each involves a different set of trade-offs. A production system must have a customized design that reflects the priorities and trade-offs inherent in the firm's own competitive situation and strategy.

The research process begins with serious reflection directed toward productivity and identifying a topic or topics worthy of a plate preparation. Considering the incredible demands on tight schedule, no activity is worth doing unless it promises to make the central part of an operators work more successful and satisfying. This study aims to analyze and give suggestions of improvements on the production and

monitoring procedure of grid casting in order to improve the productivity.

LITERATURE REVIEW

For over 150 years, the lead acid battery technology has developed and become one of the main portable sources of electric power with wide application in man's everyday life (transport vehicles, telecommunications, information technologies, etc.). It has won a dominating position in energy storage and load-levelling applications (reserve electric power supply and remote area energy systems). The lead acid battery is a complex dynamic system. This 'living' organism exists due to the simultaneous operation of two electrochemical systems: the lead system (Pb/PbSO_4 and $\text{PbO}_2/\text{PbSO}_4$) and the water system ($\text{H}_2\text{O}/\text{H}_2$ and $\text{H}_2\text{O}/\text{O}_2$). The latter is thermodynamically supported, but kinetically suppressed. These two systems are in continuous competition with each other, the lead system playing the dominating role, which makes the lead acid battery functional and useful to mankind. [1]. 19th-century illustration of Planté's original lead-acid cell up to this point, all existing batteries would be permanently drained when all their chemical reactions were spent. In 1859, Gaston Planté invented the lead-acid battery, the first-ever battery that could be recharged by passing a reverse current through it. Planté's first model consisted of two lead sheets separated by rubber strips and rolled into a spiral. In 1881, Camille Alphonse Faure invented an improved version that consisted of a lead grid lattice into which a lead oxide paste was pressed, forming a plate. Multiple plates could be stacked for greater performance. This design was easier to mass-produce. The basic principle has not changed since 1859. In the early 1930s, a gel electrolyte (instead of a liquid) produced by adding silica to a charged cell was used in the LT battery of portable vacuum-tube radios. In the 1970s, "sealed" versions became common (commonly known as a "gel cell" or "SLA"), allowing the battery to be used in different positions without failure or leakage. Today cells are classified as "primary" if they produce a current only until their chemical reactants are exhausted, and "secondary" if the chemical reactions can be reversed by recharging the cell. The lead-acid cell was the first "secondary" cell.[2,3]. The process of making changes in a company, is usually slow, regarding the layout, the machines or the organization. Therefore, it is important that all the choices which is made, strives towards the same goal, this is where the manufacturing strategy plays its part. By clearly stating a manufacturing strategy, it is possible to make the right choices, at the right time [4]. Productivity data are used to investigate the impact of product and labor market regulations on economic performance. It also allows analysts to determine capacity utilization, which in turn allows

one to gauge the position of economies in the business cycle and to forecast economic growth. If it continuously measured, it is possible to show the effects of changes in the production, and which choices have the desired effect [5]. One of the most important things for measure production is the productivity. Productivity is, according to Hannula, defined as how well a company uses its resources, which can be expressed by the formula, where the output is the output from the system and the input is all the resources that has been used [6]. To standardize a work method, is to specify which operations and in which order they should be performed to complete a work task. Effect of standardized work is a reduction of the variance in both quality and operation time. There are several factors that needs to be considered to achieve a standard, these factors are: all the operations required to complete a task, all safety procedures needed in each operation, a visual representation of where each operation takes place, the timing for each operation, and proper method of doing that. By using standardized work and constantly improving it, the productivity will be improved, which also leads to reduced costs [7]. Kaizen is a system of continuous improvement in quality, technology, processes, company culture, productivity, safety and leadership. Kaizen is a system that involves every employee - from upper management to the cleaning crew. It is continuous. In most cases these are not ideas for major changes [8]. Maintenance is an important factor in quality assurance, which is another basis for the successful competitive edge. Beyond just preventing break downs, it is necessary to keep equipment's operating within specifications (i.e. process capability) that will produce high level of quality [9]. 5S is an approach which helps to identify the problems that cannot be clearly seen when the work place is unorganized. Cleaning and organizing the workplace helps the team to uncover problems. Making problems visible is the first step of improvement [10]. Work Study is the systematic examination of the methods of carrying out activities such as to improve the effective use of resources and to set up standards of performance for the activities carried out [11]. The performance appraisal is the process of assessing employee performance by way of comparing present performance with already established standards which have been already communicated to employees, subsequently providing feedback to employees about their performance level for the purpose of improving their performance as needed by the organization. It is the process of evaluating the performance and qualifications of the employees in terms of the requirements of the job for which he is employed, for purposes of administration including placement, selection for promotions, providing financial rewards and other actions which require differential treatment among the members of a group as distinguished from actions affecting all

members equally. Performance appraisal includes all formal procedures used to evaluate personalities and contributions and potentials of group members in a working organization. [12, 13].

CURRENT STATE MAPPING

Actual monthly production data is collected from the work floor. Data analysis, identify pattern is also done to understand the current scenario. All grid types are considered same to reduce the complicity of calculation. This is done under the assumption of considering after analyzing and identifying all the production quantity for various grid type is almost same. Production data was collected, analyzed on different issues to compare & study the pattern to identify the current & critical scenario. Shift & Machine wise production quantity is summarized & graphical representation is along with that for easy observation as well as for better understanding. Loss Time was collected for each machine in six categories the way it reported in Grid Casting Activity Report. Here Shift wise, categorized & Machine wise loss time was classified & calculated. Graphical representation is also provided for better visual understanding. Efficiency of overall grid

casting is also cumulated & updated instantly to pursue & take necessary actions to improve. Machine capacity study was done under current circumstances which are compared to other monthly production data & used to estimate the overall production capacity & production quantity. Reasons are accumulated for the low productivity of Grid castings on FBD sheet. Overall comparisons are done in the Overview sheet. In this the Capacity portion the total capacity of grid casting is calculated considering the average production found by machine capacity study. This is tentative & may vary with the actual production capacity. That's why secondary verification is done with the factory actual data.

OVERVIEW OF CURRENT STATE

The following data are the accumulated data from the production floor to access the current condition. Production capacity, Machine utilization, Loss time & actual production scenario is represented here. All data provided here are the primary data collected directly from the ongoing process so that the actual scenario could be estimated clearly and the flaws could be identified.

Table 1: Capacity of the Grid casting Production floor

Production Data			Production/ Machine				Total Capacity (Grid Casting)
			Min	Prd/Hr	Prd/Shift	Wt/AIW	
Time	480	Min/shift	14	1680	13440	10080	1874880
Shift	3	Shift/ day					
Days	31	Days/month					
Machine	2	Each Shift					
Avg Prod Allowance	14 15	Mc/ min Min/Hr					

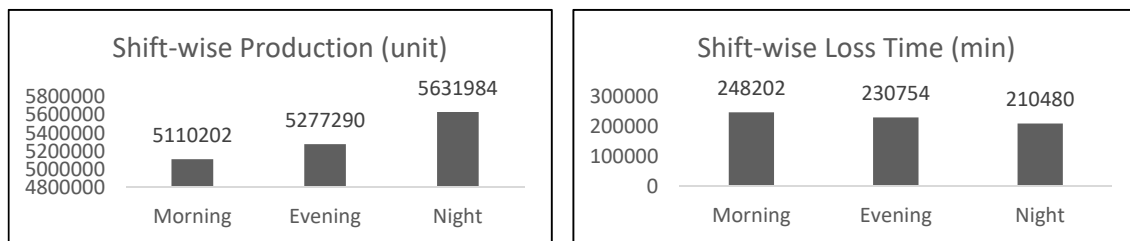


Figure 1: Shift wise production and Loss Time

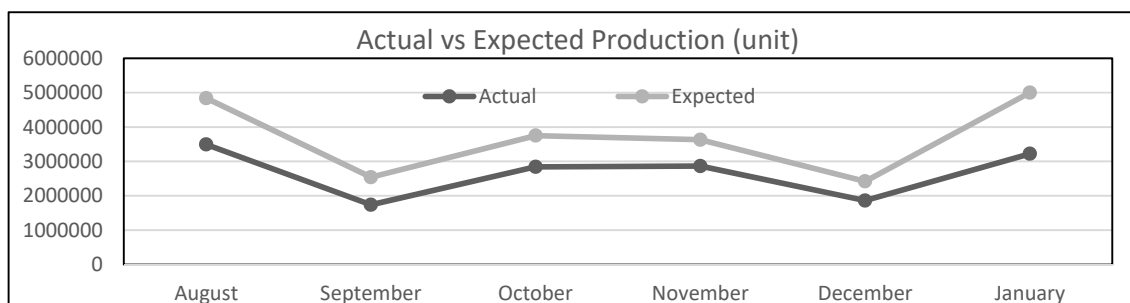


Figure 2: Actual Vs Expected Production (unit)

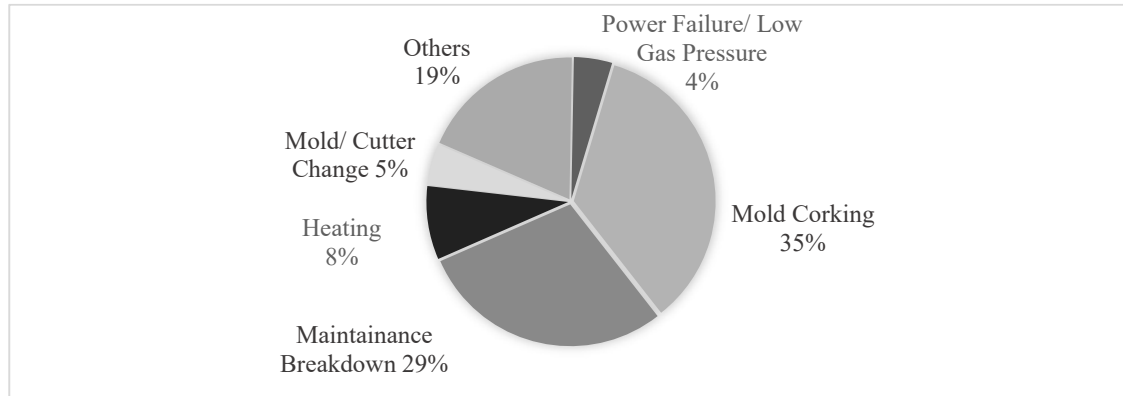


Figure 3: Cumulative percentage of Loss Times

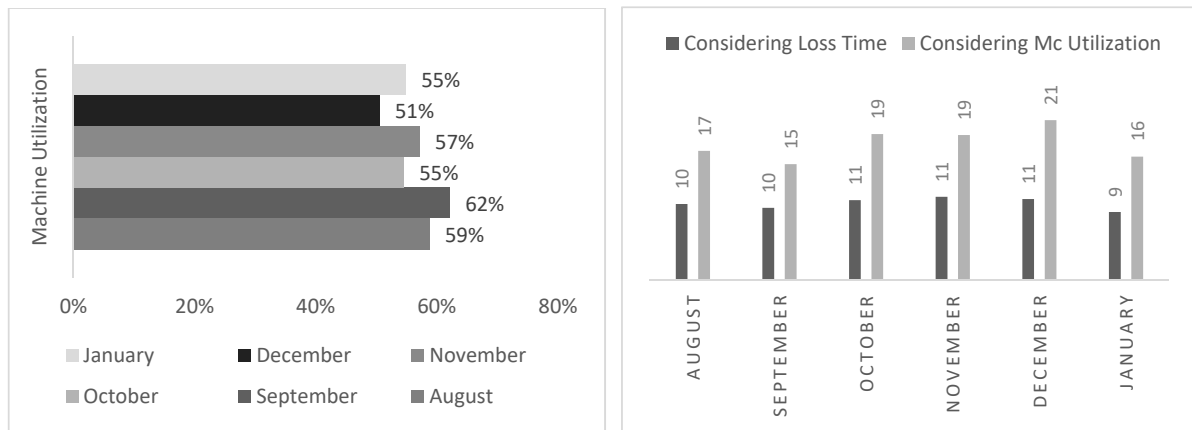


Figure 4: Machine Utilization & Productivity considering Loss time as well as Machine Utilization

FUTURE STATE MAPPING

Based on the collected data mentioning the time span the future state was developed. Production condition, production quantity & the area of small and medium improvements was identified considering existing capacity of grid production. Compared the actual & existing scenario observations are made. Made those as suggestions which are under consideration and verifying with the existing procedure.

All detailed work done are enclosed here and the detailed calculations are attached at the groceries. According to the data and observation, suggestions are made for monitoring production floor, tracking work, productivity & preventive maintenance work shows the estimation of capacity considering the average production found in the previous study. Where the other parameters and considerations remains same. Afterwards, the comparison is also shown in here.

Table 2: Estimated capacity calculation

Production Data			Production/ Machine				Total Capacity (Grid Casting)
			Min	Prd/Hr	Prd/Shift	Wt/AlW	
Time	480	Min/shift	15	1800	14400	10800	9039600
Shift	3	Shift/ day					
Days	31	Days/month					
Machine	9	Each Shift					
Avg Prod	15	Mc/ min					
Allowance	15	Min/Hr					

Existing capacity: 7066817 units; obtained by the average output/min using 6 months' production data
 Estimated Capacity: 9039600 units; considering m/c utilization time and proper monitoring on each shift
 1972783 units can be increased with improved productivity and proper m/c utilization, i.e., around 28% capacity improvement

Table 3: Production Scenario Comparison after implementing of Hourly Monitoring

	Previous	Current	Difference
Production (Pcs)	156900	174800	17900
Productivity/ min	8	9	1
Efficiency	65%	72%	7%
Loss time (min/ day)	491	422	69
Utilization (min/ day)	949	1018	69

Table 4: Improved scenario of Grid Casting production

			Target	Production		Daviation		Productivity		Efficiency		Losstime		Utilization	
Sl	Date	Shift		Shift	Day	Shift	Day	Shift	Day	Shift	Day	Shift	Day	Shift	Day
1	10/2/2016	Morning	11500	9400	27400	2100	7100	10	10	82%	79%	135	395	345	1045
		Eveneing		9350		2150		10		81%		120		360	
		Night		8650		2850		9		75%		140		340	
2	11/2/2016	Morning	11500	6350	24800	5150	9700	7	9	55%	72%	240	410	240	1030
		Eveneing		8450		3050		9		73%		110		370	
		Night		10000		1500		10		87%		60		420	
3	12/2/2016	Morning	11500	6900	26150	4600	8350	7	9	60%	76%	195	360	285	1080
		Eveneing		9650		1850		10		84%		90		390	
		Night		9600		1900		10		83%		75		405	
4	13/2/2016	Morning	11500	6400	19550	5100	14950	7	7	56%	57%	225	620	255	820
		Eveneing		3750		7750		4		33%		320		160	
		Night		9400		2100		10		82%		75		405	
5	14/2/2016	Morning	11500	6000	25350	5500	9150	6	9	52%	73%	265	415	215	1025
		Eveneing		9650		1850		10		84%		90		390	
		Night		9700		1800		10		84%		60		420	
6	15/2/2016	Morning	11500	8650	27400	2850	7100	9	10	75%	79%	110	320	370	1120
		Eveneing		9400		2100		10		82%		135		345	
		Night		9350		2150		10		81%		75		405	
7	16/2/2016	Morning	11500	8850	24150	2650	10350	9	8	77%	70%	130	435	350	1005
		Eveneing		9350		2150		10		81%		75		405	
		Night		5950		5550		6		52%		230		250	
Grand Total			80500		174800		66700		9		72%		422		1018

RESULTS AND DISCUSSIONS

Current capacity of the grid casting production floor considering the parameters on the left column of the Table 1. We calculated the shift wise production and loss time what showed in Figure 1 and this helps us to get the expected output considering the current capacity which is shown in Figure 2 along with the actual output. Here we found the deviation of production and thus we tracked all the reason behind it. Loss time is identified individually and shown in

Figure 3 where we can visualize its impact clearly. Machine Utilization & Productivity considering Loss time and machine utilization is shown in Figure 4 where we can see the capacity usages throughout the time period of analysis. In Table 2 considering the same parameters of table 1 and the capacity we found the estimated capacity of production floor. To enhance that production rate must be improved to atleast 15 grids/ min which will lead to a capacity escalation to 1972783 grids/ each month. However, it

is not possible to calculate how much exactly for such bound. Besides, there are significant other fact which can't be neglected in the findings. Chasing this capacity applying proper monitoring we found the changes and improvement which are shown in the Table 3. In Table 4 we see the improved scenario of a week-long Data where we can see the significant changes.

From the beginning the goals included, optimizing the resource utilization of the work floor in the production line utilization was measured to about below 12%. We know higher productivity leads to sustainable growth. Since none of the improvements have been tested in the system directly, the exact effect of them is not known yet. But by having breaks in shifts and making sure that the external part of the calculations is done in time, it would be possible to increase the utilization of the machine and resource 7~8 % and productivity about 21 % which may cause an overall improvement by 28 %. It is found that 35% of total loss time is consumed by corking and 29% machine breakdown as well as contributing 19% to other issues. It has been clearly seen that 14% overall deviation in expected production considering average production/ Hour (each machine output/ min) and machine utilization time. The average overall efficiency was found around 56%.

CONCLUSIONS

This paper focuses on finding and solving the problems that exists in the production floor of grid casting unit. The problems derive mostly from the lack of standardization and the lack of measurements. In order to have standardized work methods, the staffing needs to be the same in both shift teams. For the Grid casting department to reach its full potential, it is important that the rest of the supportive departments also start working with standardization. As from the machine utilization time we get that the capacity is much higher than what we are getting in production. If the standardized work division and worksheets are used; it should be possible to improve the current scenario from an average of 12 grids/ min to 15 grids/ minutes, leading to a total production increase to 28 %. However, the production increase is only possible if there is a viable production plan and the needed components are available. After the standardization changes, the largest losses remaining are, mold corking related issues. It remains the key obstacle which hinder the productive time. Both the suggestions and observation are remaining as a guideline to follow but it should be a benefit if applied as a standardize change, however, the effect is not measurable while the changes are not implemented. Therefore, this improvement is not included in the results. In order to minimize the remaining losses, it is necessary to find out the other underlying reasons by measuring

and documenting the occurring breakdowns. That will lead to further possible improvements in the grid casting and related production area.

REFERENCES

- [1] Kathryn R.B., "Lead Acid Batteries.", Journal of Power Sources, Volume 51, Issues 1–2, pp 1-17, August–September 1994.
- [2] Richard S. T., "The Lead-Acid Battery: Its Voltage in Theory and in Practice", Journal of Chemical Education, Volume 79, Issue 3, pp 334, March 1, 2001.
- [3] John B. G., "Evolution of Strategies for Modern Rechargeable Batteries." Accounts of Chemical Research, Volume 46, Issue 5, pp 1053–1061, 2013.
- [4] Miltenburg, J., "Setting Manufacturing Strategy for A Company's International Manufacturing Network.", International Journal of Production Research, Volume 47, Issue 22, pp 6179–6203, 2009.
- [5] Peter T. W., John K. Mc., Larry P. R., Deven S., "Competitive Priorities in Operations Management", Journal of the Decision Sciences Institute, Volume 29, Issue 4, pp 1035-1046, September 1998.
- [6] Hannula, M., "Total productivity measurement based on partial productivity ratios.", International Journal of Production Economics, Volume 78, Issue 1, pp 57–67, 2002.
- [7] Felicity J., Lea W., Paul D., "Perceived acceptance and work standards as predictors of work attitudes and behavior and employee psychological distress following an internal business merger", Journal of Managerial Psychology, Volume 25, Issue 1, pp 22-43, 2010.
- [8] Bhoi A. J., Desai A. D. and Patel M. R., "The Concept & Methodology of Kaizen", International Journal of Engineering Development and Research, Volume 2, Issue 1, pp 813-818, 2014.
- [9] Jerry P. Allen Jr. "Safety Management Systems for Maintenance Organizations", Symposium on Human Factors in Aviation Maintenance, Volume 3, Issue 4, pp 151-176, 2001.
- [10] Günther Z., Hubert M., "New concepts for production planning and control", European Journal of Operational Research, Volume 67, Issue 3, pp 297-320 pp 382-452, 25 June 1993.
- [11] Mahto D., "Productivity Improvement through Process Analysis for Optimizing Assembly Line in Packaging Industries", Global Journal of Researches in Engineering Industrial Engineering, Volume 13, Issue 3, pp 11-25, 2013.
- [12] Osabiya B. J., "Effectiveness of Performance Appraisal as a Tool to Measure Employee Productivity in Organizations.", Journal of Public Administration and Governance, Volume 4, Issue 4, pp 135 - 148, 2014.
- [13] Michael A., Melanie E. L., Dinesh C. J., "Employee Performance Measurement and Performance Appraisal Policy in an Organization", Mediterranean Journal of Social Sciences, Volume 5, Issue 9, pp 342 - 347, 2014.

EFFECT OF AROMATIC AMINE ANTIOXIDANTS ON EMISSION CHARACTERISTICS WITH MORINGA BIODIESEL BLEND IN A MULTI-CYLINDER DIESEL (MCD) ENGINE

M.M. Rashed¹, M. A. Kalam²

¹Department of Mechanical Engineering, University of Malaya, 50603, Kuala Lumpur, Malaysia

²Senior Lecturer, Department of Mechanical Engineering, University of Malaya, 50603, Kuala Lumpur, Malaysia

Corresponding Email: rashed.duet31@gmail.com

Abstract: Two most effective aromatic amine antioxidants *N*, *N'*-diphenyl-1, 4-phenylenediamine (DPPD) and *N*-phenyl-1, 4-phenylenediamine (NPPD) were used at a volume of 2000 ppm concentration. The impact of antioxidant on engine emissions were analyzed in a multi-cylinder diesel engine fuelled with MB20 (20% Moringa oil methyl ester and 80% diesel fuel blend) biodiesel blends. Addition of antioxidants showed no remarkable negative impact on biodiesel physicochemical properties, while the stability of biodiesel increased. Among these two aromatic amine antioxidants DPPD exhibits better stability. The results also showed decreased NOX emission of about 3.04%-7.4%, however the HC and CO increased for all blends. For this reason MB20 blends with amine antioxidants can be used in diesel engine without any modification.

Keywords: *Moringa oleifera*; Physico-chemical properties; Emissions, amine antioxidants.

INTRODUCTION

Production of biodiesel from vegetable oils as a sources of edible oil were considered as one of the potential feedstocks [1]. Storage stability and coarse oxidative are the significant disadvantage of biodiesel fuel [2]. It is all around record that auto-oxidation occur due to the presence of oxygen comes from atmosphere and that is why biodiesel goes to degrades [3]. There are various investigated literature for stability of biodiesel blends [4, 5]. Varatharajan et al [6] investigated the impact of adding two aromatic amine antioxidant (DPPD and NPPD) blended with soybean biodiesel on NOx emission in a single cylinder diesel engine. They found that CO and HC increases 10.52% and 9.096% respectively, while the NO reduce 9.35% added DPPD antioxidant. In another study, Varatharajan et al [7] observed the effect of antioxidants on NOx emission of jatropha biodiesel with different antioxidants additives like as 0.025%-m of additives, p-phenylenediamine, ethylenediamine, l-ascorbic acid, α -Tocopherol acetate, and BHT in a single cylinder diesel engine (SCDE) and found that p-phenylenediamine produce 43.55% average lower NOx compare with pure biodiesel. The objectives of this study is to experimentally find out the effect of two most promising aromatic amine antioxidant (DPPD and NPPD) on engine emission in a multi cylinder diesel (MCD) engine fuelled with Moringa biodiesel blends. There are no experimental work have been found on the basis of MCD engine by using two aromatic amine antioxidant (DPPD and NPPD) with Moringa biodiesel.

MATERIALS AND METHODS

In this present study, the tested engine was Mitsubishi pajero, 4D56T at 55 kW with multi-cylinder computerized radiator cooling system inline diesel engine. The engine specification is given in **table 1** and the experimental setup is shown in **fig 1**. The experimental investigation was carried out by using diesel and with different blends with and without antioxidant (MB0, MB20, MB20+DDPD and MB20+NPPD). All experiment were taken with variation of engine speed starting from 1000 rpm to 4000 rpm at an interval of 500 rpm at constant load condition.

Table 1. Specification of the engine

Model	4 cylinder inline diesel engine
Type	Four cylinder, four stroke
Displacement (cc)	2476
Cylinder bore x strok (mm)	92 x 96
Compression ratio	21:1
Maximum engine speed (rpm)	4200
Maximum power (kW)	55
Fuel system	Distribution type jet pump (indirect injection)
Lubrication System	Pressure feed and full flow system
Combustion chamber	Swirl type
Cooling system	Radiator cooling
Air flow	Turbocharged
Valve mechanism	SHOC

Table 2. Physico-chemical properties of used fuels

Properties	Diesel (B0)	MB10	MB2	MB20+DPP	MB20+NPP
Calorific value (Mj/kg)	45.453	40.36	44.02	44.10	44.08
Kinematic viscosity @ 40°C (cSt)	3.10	4.80	3.56	3.572	3.59
Density @ 40°C (kg/m ³)	828	862	837	833.2	833
Flash point (°C)	67	169	85.2	87.3	85.0
Oxidation stability (h)	58.2	3.79	5.28	22.3	18.9

RESULTS AND DISCUSSION

NOx Emission

Fig. 2 demonstrate the NOx variation with the speed. The NOx were increased linearly up to speed 3000 rpm and then decreased very slowly. By adding antioxidant (DPPD, NPPD) with MB20, the NOx emission comparatively shows lower. The average NOx emission in all tested fuels are 209.85 ppm, 248.28 ppm, 229.85 ppm and 240.71 ppm for the B0, MB20, MB20+DPPD, MB20 +NPPD accordingly and the average increase NOx emission 15.47%, 8.7%, and 12.82% compare to B0.

HC Emission

Fig. 4 demonstrates the fluctuation of HC emission with varying speed for all tested blends. The HC emission is gradually decreased with increasing speed. The maximum and minimum HC emission are shown at 1000 rpm and 4000 rpm respectively. It is point noted that the mean reduction of HC emission is 27.64%, 19.07% and 10.04 % for MB20, MB20 +DPPD and MB20 +NPPD respectively to compare with B0.

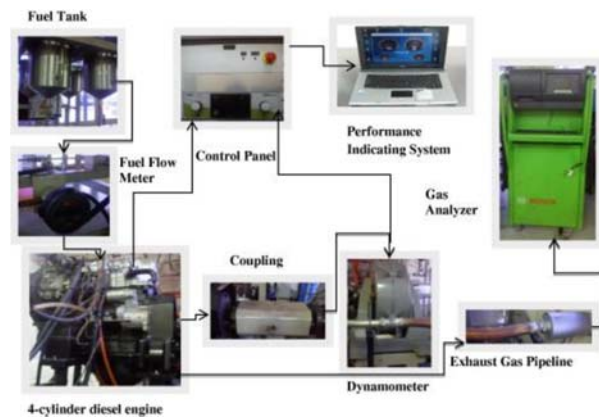


Fig 1: The experimental setup.

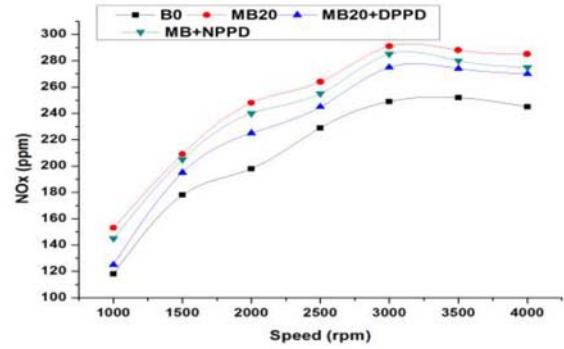


Fig 2: Fluctuation of NOx emission at different speed

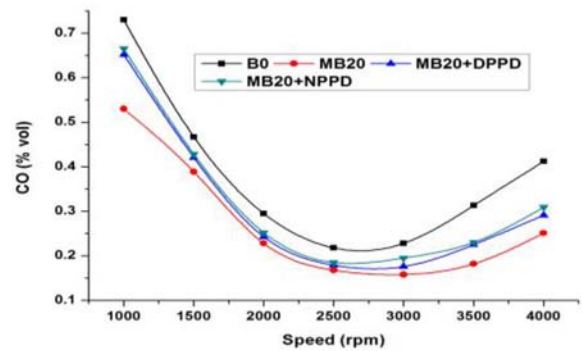


Fig 3: Fluctuation of CO emission at different speed

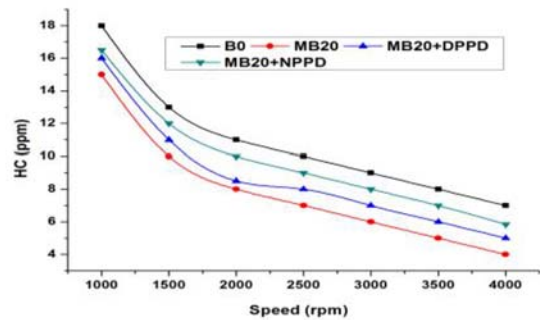


Fig 4: Fluctuation of HC emission with respect to speed

CO Emission

Fig. 3 demonstrate the fluctuation of CO emission with varying speed for all tested fuels with and without antioxidant in a multi cylinder diesel engine at full load condition. It was point out that, CO emission lessens adequately in all blends compare with pure biodiesel (B0). The maximum CO emission was found from pure biodiesel. The mean lessens of CO emission are

28.41%, 17.87% and 15.98% for MB20, MB20 +DPPD, MB20 +NPPD to compare with B0. However, the addition of antioxidant of 2000 ppm of DPPD and NPPD into the biodiesel enhanced the CO emission adequately. The amount CO emission is still less by adding antioxidant in biodiesel compared to pure diesel.

CONCLUSION

Moringa biodiesel (20% by volume) blends meets the ASTM specification standards. Addition of amine antioxidant additives (DPPD, NPPD), reduce the calorific value but enhance the kinematic viscosity, density, flash point and oxidation stability. By comparing two amine antioxidant (DPPD, NPPD), DPPD having higher oxidation stability with MB20. MB20 produces 15.57% higher NO_x compared to neat biodiesel. The addition of DPPD and NPPD with MB20 reduce the NO_x emission compared to MB20. The addition of DPPD and NPPD antioxidant additives in moringa biodiesel blends increase the CO emission adequately for MB20 blend. But this increase was comparatively lower than diesel. The additive lessens the oxidation capability of CO and for this reason, the CO emission increase. HC emission increased due to addition of DPPD and NPPD with MB20, but compared to diesel it was lower.

REFERENCES

- [1] Atabani, A., et al., Non-edible vegetable oils: a critical evaluation of oil extraction, fatty acid compositions, biodiesel production, characteristics, engine performance and emissions production. *Renewable and Sustainable Energy Reviews*, 2013. **18**: p. 211-245.
- [2] Serrano, M., et al., Oxidation stability of biodiesel from different feedstocks: influence of commercial additives and purification step. *Fuel*, 2013. **113**: p. 50-58.
- [3] Puna, J., et al., Advances on the development of novel heterogeneous catalysts for transesterification of triglycerides in biodiesel. *Fuel*, 2010. **89**(11): p. 3602-3606.
- [4] Mofijur, M., et al., Evaluation of biodiesel blending, engine performance and emissions characteristics of *Jatropha curcas* methyl ester: Malaysian perspective. *Energy*, 2013. **55**: p. 879-887.
- [5] Jain, S. and M. Sharma, Oxidation stability of blends of *Jatropha* biodiesel with diesel. *Fuel*, 2011. **90**(10): p. 3014-3020.
- [6] Varatharajan, K., M. Cheralathan, and R. Velraj, Mitigation of NO_x emissions from a *jatropha* biodiesel fuelled DI diesel engine using antioxidant additives. *Fuel*, 2011. **90**(8): p. 2721-2725.
- [7] Varatharajan, K. and M. Cheralathan, Effect of aromatic amine antioxidants on NO_x emissions from a soybean biodiesel powered DI diesel engine. *Fuel processing technology*, 2013. **106**: p. 526-532.

DESIGN OF INTEGRATED SUPPLY CHAIN NETWORK UNDER TRANSIENT DEMAND AND COST UNCERTAINTY

Ferdous Sarwar¹, Md Saiful Islam²

¹Department of Industrial and Production Engineering, Bangladesh University of Engineering and Technology, Dhaka-1000, Bangladesh

² Department of Mechanical and Industrial Engineering, Northeastern University, Boston, MA-2115, USA
Corresponding e-mail: ferdoussarwar@ipe.buet.ac.bd

Abstract: A supply chain network is dynamic in nature and is a function of different parameters. This study proposes a mixed integer linear programming model to design a supply chain network considering minimization of total supply chain cost and network flow time along with maximization of demand satisfaction rate and volume flexibility for multiple products and echelons. To reflect the dynamic nature of supply chain, this model addresses transient demand and cost uncertainty. The optimization model provides a set of trade-off solutions between the objectives with facility location decision. The model is illustrated with a simulated example and solved with NSGA-II algorithm to provide a robust solution.

Keywords: Supply chain network, Multi-objective optimization, Uncertainty in supply chain, NSGA-II, Pareto optimal solution

1 Introduction

Now a days, organizations are considering supply chain as an important area which can provide cost effectiveness and competitive edge over similar organizations¹. Shahparvari et al.² define the Supply chain management as, “the coordination and synchronization of the flow of resources in the network of suppliers, manufacturing facilities, distribution centres’ and customers”. Integration of these stakeholders/ echelons can help achieving profitability and avoid unnecessary events³. But the most challenging task is to design an integrated network optimizing all the echelons as they have different and conflicting objectives. Optimizing one of them will not result in maximum overall profitability which can be achieved by considering multiple aspects (i.e. cost, time, customer satisfaction, profit, flexibility etc.) of the supply chain and its dynamic nature⁴. Moreover, the competition between the organizations has been shifted to competition between supply chains. Involvement of multiple entities and multiple level decision making made the supply chain network design (SCND) a multi-objective optimization problem. In a review of facility location problems,

Melo et al.⁵ indicated that only 9% of the studies consider multiple objectives while 75% of the studies featured solely minimization of cost in Supply Chain Network Design. The objectives like responsiveness, network flow time, lead time, flexibility were not addressed although, several recent studies^{3,4,6,7} considered supply chain network design as a multi-objective problem.

In addition to the complexity of SCND, uncertainty in business environment makes supply chain more complex and requires close attention. Usually SCND involves strategic decision making for longer time period but, the initial considerations, constraints, and assumptions change over time⁸. Global economy, climate change, natural disaster, politics etc. anything can change or imbalance the perfect world assumption of supply chain. Moreover, rapid growth of technology is contributing to uncertainty in supply chain. To reflect this dynamic nature, mostly demand uncertainty was considered⁹. Uncertainty in cost, transportation time, supply disruption, labor etc. was paid less of less concern. To create a ‘close to real world’ model, supply chain network (SCN) should be considered as multi-objective problem with multiple source of uncertainty.

2 Literature Review

Supply chain is driven by a set of parameters, such as, cost, time, flexibility, resilience, service level etc. Different researchers considered different set of parameters in their optimization model, among them cost is the most common. Almost all the literature considers either cost or profit as one of the objectives^{3,10-16}.

Altıparmak et al.¹⁰ considered cost, service level and capacity utilization in their model. But, they only considered distribution costs and fixed costs in plant and distribution centers. Service level was modelled as the amount of demand satisfied within the acceptable time period. Wang et al.¹⁶ introduced a newer concept, environmental influence, in supply chain modelling. They presented a trade-off approach between cost and environmental effect to assist managerial decision and designing green supply chain. Some researchers^{3,17,18} used profit as an objective function instead of cost which is very similar to cost minimization because, profit is calculated by subtracting cost from total revenue and total revenue is constant for deterministic demand models. Another way to represent cost is to evaluate the financial performance of the organization which is adopted in¹⁹.

Other than cost, the most common objective function found in different study is customer satisfaction. Studies in^{4,6,20} use demand satisfaction rate/service level which is calculated as the ratio between products sold and existing demand in the market. Another popular objective used in supply chain optimization models is time. Some researchers consider lead time^{7,21}, some consider network flow time²² or delay on delivery¹¹. Objectives like flexibility, capacity utilization, responsiveness are often left unnoticed but, those are becoming very important as today's supply chain has to deal with a lot of uncertainty.

A good model can become irrational or can produce inaccurate result if the dynamic nature of the supply chain is not reflected. This dynamic nature or uncertainty is now increasing²³. In a review of supply chain planning under uncertainty, Lalmazloumian and Wong⁹ identified three major source of uncertainty. They are, "supply uncertainty, process/manufacturing uncertainty, and demand

uncertainty". In their analysis they found that only demand uncertainty was considered in most of the studies. Supply and process/manufacturing uncertainty were mostly ignored⁹. Pujawan et al.²⁴ also reported three sources of uncertainty - supply, demand, and operations, which they mentioned as causes of instability in scheduling. Lalmazloumian and Wong⁹ also categorized different approaches used to address the source of uncertainty. The categories are, Distribution based, Fuzzy based, Scenario based, Simulation based and Hybrid based approaches. Distribution based approach uses stochastic framework to formulate the optimization model wherein Fuzzy based approach use fuzzy set theory. Scenario based approach considers different possible scenarios which helps the organization to prepare for different situations. Simulation based approach use different simulation techniques like discrete event simulation, monte-carlo simulation etc. to internalize the dynamic behaviour and the Hybrid based approach uses a combination of analytic and simulation techniques.

Solving multi-objective SCND problem is a complex one. There are different algorithms, mostly heuristic algorithms used in literature to solve such complex problem. Altıparmak et al.^{10,20} used a genetic algorithm approach to solve three objective model wherein Yuce et al.⁷ used more advanced, swarm based, and comparatively new bee's algorithm to optimize their two objective model. Ant colony algorithm was used to optimize a three objective supply chain model⁴. Another heuristic based algorithm named as intelligent water drop algorithm was used to optimize bi-objective model in¹⁵. Each algorithm has its own advantages and disadvantages and there is no specific algorithm which can be efficiently used to optimize all sorts of problem⁷. In the multi-objective supplier selection model, Kazemi et al.²⁵ used fuzzy approach for solution purposes. In the search for widely used and tested algorithm in supply chain modelling, authors found that Non-dominated Sorting Genetic Algorithm II (NSGA-II) proposed by Deb et al.²⁶ can perform efficiently and has been used to solve multi-objective supply chain models. Apart from supply chain modelling, this algorithm has been successfully used in chemical process optimization²⁷ and electricity generation planning²⁸.

3 Model Formulation

Business world is currently becoming more and more complex because of globalization, intense competition, deregulation, and converging trend of industries²⁹. Moreover, rapid development of technology is creating highly variable and quick changing customer demand. To maintain good financial health and competitiveness, an organization should have SCN with optimized cost, time, product quality, flexibility. Our objective is to provide a realistic mathematical model to design a SCN optimized in several front.

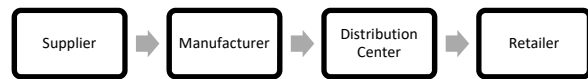
3.1 Problem Identification

A typical supply chain can be defined as an interconnected network between supplier, manufacturer, customer, and distribution network³⁰. The optimized network is achieved by selecting optimal resources in order to satisfy organization's specific objective/objectives. Literature shows that supply chain has multi-dimensional characteristics and some of these dimensions are conflicting in nature, such as, higher demand satisfaction rate or service level usually cause higher cost. A better way to resolve these conflicts is to provide a set of trade-off solutions (Pareto Optimal Solution) between the differing objectives.

3.2 Problem Statement

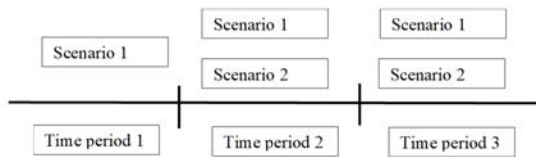
This research considers a generic SCN where manufacturing plant produce multiple products and use warehouses, and distribution centers (DC) to transfer products to customer zones. Therefore, it is a four echelon supply chain network which intends to minimize total cost and network flow time along with maximization of demand satisfaction rate and volume flexibility. An illustration of the echelons is given in the figure below.

Figure 1 Arrangement of echelons



Problem in this research assumes that an organization produces multiple products in multiple manufacturing plants. Each plant can produce all types of products. The finished products are then transferred to the warehouse for which the company has different options. It can choose any warehouse from the options depending upon the associated costs (i.e. fixed infrastructure cost, material handling cost and inventory holding cost), capacity, and goal. Then the products are transferred to fixed distribution centers, which will forward the products to different customer zones according to the demands. Demand of each customer zone is assumed to be uncertain. It varies according to time period and possible scenarios (i.e. economic growth or recession, weather, natural disaster, etc.) at each time period. From the historical data, the organization can forecast demand pattern of each product for each time period and scenario. The factors that change the demand pattern will surely impact the cost of production, transportation, material handling, and inventory holding. So, the costs associated with the process are also assumed to be uncertain for different time periods and possible scenarios. Similarly, cost can be estimated from the historical data available from similar situations. Transportation time remains same at different time period and scenario. As it is a universal truth that getting product faster will cost more, transportation costs are assumed higher for those warehouses which take lesser time to transport. The similar case is considered in the transportation of product from warehouse to the distribution center and distribution center to customer zone. Amount of product that can be transported from an echelon to another echelon has certain maximum and minimum value, amount of material transported must fall within this range.

Figure 2 Schematic representation of time period and scenario.



Moreover, parameters that are considered to be uncertain (demand and cost) do not change continuously. It changes after a certain time and remain almost same for a specific period of time. Hence, the uncertainty present in this problem is transient in nature. This study considers three time period based on three seasons in a year (winter, summer, and fall). At the first time period, demand and cost forecast is more accurate than the time period 2 and 3. So, only one possible scenario is considered in time period 1 and two possible scenarios are considered in time period 2 and 3. Number of time period and scenario can be changed for specific organization or fiscal year.

The trade-off between costs, network flow time, demand satisfaction level, and volume flexibility along with transient demand and cost leads the author of this work to formulate a mixed integer multi-objective supply chain network optimization model. One criterion tries to minimize the fixed infrastructure cost of warehouse, production cost, transportation cost in between echelons, material handling costs, and inventory holding cost. Another one tries to minimize total network flow time of a product while the rest two covers the maximization of demand satisfaction level and volume flexibility of the company.

Some assumptions have been considered while designing the multi-objective SCN optimization model. The main assumptions of the provided model are:

1. Work in progress has no holding cost
2. Fixed infrastructure cost does not depend on scenarios as it is a one-time cost.

3. Handling or processing time for a product is same for all warehouses and distribution centers.
4. Material handling cost at manufacturing plant is assumed to be zero.
5. Production rate can vary from scenario to scenario.
6. Each product takes same time to be manufactured at each plant.
7. The structure of the distribution network (i.e. transportation links between plant, warehouse, Distribution center, and customer zone) is independent of the scenarios.
8. Transportation time in between echelons is independent of the scenarios.
9. Each echelon takes same time to handle the material.

3.4 Nomenclature

3.4.1 Indices and Parameters

m = Product types

i = Manufacturing plants

j = Possible warehouse

k = Possible distribution centers

l = Customer zones

s = Possible demand and cost scenarios

t = Time period

C_j^W = Annual fixed cost to establish warehouse j .

C_k^D = Annual fixed cost to establish DC at location k .

NS = Number of possible scenarios in each time period

Ψ_s = Probability of occurring scenario s

C_{mit}^{Ps} = Unit production cost for product m in plant i during time period t under scenario s

C_{mjt}^{HWHs} = Unit material handling cost for product m in warehouse j during time period t under scenario s

C_{mkt}^{HDCs} = Unit material handling cost for product m in DC k during time period t under scenario s

C_{mit}^{IPS} = Inventory holding cost of product m at plant i during time period t under scenario s

C_{mjt}^{IWHs} = Inventory holding cost of product m at warehouse j during time period t under scenario s

C_{mkt}^{IDCs} = Inventory holding cost of product m at DC k during time period t under scenario s

C_{mijt}^{TRS} = Unit transportation cost of product m transferred from plant i to warehouse j during time period t under scenario s

C_{mjkt}^{TRS} = Unit transportation cost of product m transferred from warehouse j to DC k during time period t under scenario s

C_{mkl}^{TRS} = Unit transportation cost of product m transferred from DC k to customer zone l during time period t under scenario s

ΔT_t = Duration of time period t

T_{ij} = Transportation time for transferring product from plant i to warehouse j

T_{jk} = Transportation time for transferring product from warehouse j to DC k

T_{kl} = Transportation time for transferring product from DC k to customer zone l

D_{mlt}^s = Demand of product m from customer zone l during time period t under scenario s

W_j^{max} = Maximum capacity of warehouse j

W_j^{min} = Minimum capacity of warehouse j

DC_k^{max} = Maximum capacity of DC k

DC_k^{min} = Minimum capacity of DC k

M_i^{max} = Maximum product holding capacity at plant i

M_i^{min} = Minimum product holding capacity at plant i

$\alpha_1, \alpha_2, \alpha_3$ = Weight factor for capacity utilization [0, 1]

$Q_{mij}^{s,max}$ = Maximum rate of flow of product m that can be transferred from plant i to warehouse j under scenario s

$Q_{mjk}^{s,max}$ = Maximum rate of flow of product m that can be transferred from warehouse j to DC k under scenario s

$Q_{mkl}^{s,max}$ = Maximum rate of flow of product m that can be transferred from DC k to customer zone l under scenario s

$Q_{ij}^{s,min}$ = Minimum rate of flow of product m that can be transferred from plant i to warehouse j under scenario s

$Q_{jk}^{s,min}$ = Minimum rate of flow of product m that can be transferred from warehouse j to DC k under scenario s

$Q_{kl}^{s,min}$ = Minimum rate of flow of product m that can be transferred from DC k to customer zone l under scenario s

$P_{mit}^{s,max}$ = Maximum production capacity of plant i for product m at time period t under scenario s

$P_{mit}^{s,min}$ = Minimum production capacity of plant i for product m at time period t under scenario s

3.4.2 Continuous variables

P_{mit}^s = Production rate of product m for plant i during time period t under scenario s

Q_{mijt}^s = Rate of flow of product m transferred from plant i to warehouse j during time period t under scenario s

Q_{mjkt}^s = Rate of flow of product m transferred from warehouse j to DC k during time period t under scenario s

Q_{mkl}^s = Rate of flow of product m that can be transferred from DC k to customer zone l during time period t under scenario s

I_{mit}^s = Inventory level of product m being held at plant i at the end of time period t under scenario s

I_{mjt}^s = Inventory level of product m being held at warehouse j at the end of time period t under scenario s

I_{mkt}^s = Inventory level of product m being held at DC k at the end of time period t under scenario s

3.4.3 Binary variables

$Y_j = 1$ if warehouse j is established, 0 otherwise.

3.5 Objective function to optimize overall expected cost of supply chain network

Supply chain cost consists of various components. To avoid complexity, researchers often chose a particular set of cost elements. In a research¹⁴, authors considered training, hiring, manpower, and production cost wherein, Altiparmak et al.¹⁰ considered transportation cost and infrastructure cost of manufacturing plant and distribution centers. Sabri and Beamon³¹ considered fixed infrastructure cost, transportation cost, and material handling cost. In this model, the cost elements considered by Georgiadis et al.³² are adopted.

This problem considers warehouse would be established if a potential candidate is chosen. Fixed infrastructure cost of warehouse j if it is chosen (when $Y_j=1$) would be,

$$\sum_j C_j^w Y_j$$

Production cost of product m in produced in plant i at time period t under scenario s can be computed by

$$\sum_{s=1}^{NS} \psi_s \sum_j C_{mit}^{Ps} P_{mit}^s \quad \forall t, s = 1, \dots, NS$$

Material handling cost can be calculated by multiplying the amount of product processed in a warehouse and distribution centers with a fixed rate for time period t under scenario s .

$$\sum_{s=1}^{NS} \psi_s \{ \sum_{mj} C_{mit}^{WHs} (\sum_i Q_{mijt}^s) + \sum_{mk} C_{mkt}^{DCs} (\sum_j Q_{mjkt}^s) \} \quad \forall t, s = 1, \dots, NS$$

Inventory holding cost is also calculated in similar manner, cost rate multiplied by inventory on hand. Inventory on hand is calculated by taking the average of on hand product at the beginning and ending of a time period. As we assumed work in progress has no inventory cost, it is not included in this cost element.

$$\sum_{s=1}^{NS} \psi_s \{ \sum_{mi} C_{mijt}^{IPs} \frac{(I_{mit}^s + I_{mi,t-1}^s)}{2} + \sum_{mj} C_{mjt}^{IWHs} \frac{(I_{mjt}^s + I_{mj,t-1}^s)}{2} + \sum_{mk} C_{mkt}^{IDCs} \frac{(I_{mkt}^s + I_{mk,t-1}^s)}{2} \} \\ \forall t, s = 1, \dots, NS$$

In every time period and scenario, products are transferred from plants to warehouses, warehouses to distribution centers and distribution center to customer zones.

$$\sum_{s=1}^{NS} \psi_s (\sum_{mij} C_{mit}^{TRs} Q_{mijt}^s + \sum_{mjk} C_{mjk}^{TRs} Q_{mjkt}^s + \sum_{mkl} C_{mkl}^{TRs} Q_{mkl}^s) \\ \forall t, s = 1, \dots, NS$$

Total cost of the supply chain is achieved by taking the summation of all the cost elements mentioned above which leads to the first objective function (f_1).

$$\begin{aligned}
& \text{minimize } f_1 \\
& = \sum_j C_j^W Y_j \\
& + \sum_t \Delta T_t \left[\sum_{s=1}^{NS} \psi_s \sum_j C_{mit}^{Ps} P_{mit}^s \right. \\
& + \sum_{s=1}^{NS} \psi_s \left\{ \sum_{mj} C_{mit}^{WHS} \left(\sum_i Q_{mijt}^s \right) \right. \\
& + \left. \sum_{mk} C_{mkt}^{DCs} \left(\sum_j Q_{mjkt}^s \right) \right\} \\
& + \sum_{s=1}^{NS} \psi_s \left\{ \sum_{mi} C_{mit}^{IPs} \frac{(I_{mit}^s + I_{mi,t-1}^s)}{2} \right. \\
& + \sum_{mj} C_{mjt}^{IWHs} \frac{(I_{mjt}^s + I_{mj,t-1}^s)}{2} \\
& + \left. \sum_{mk} C_{mkt}^{IDCs} \frac{(I_{mkt}^s + I_{mk,t-1}^s)}{2} \right\} + \sum_{s=1}^{NS} \psi_s \left(\sum_{mij} C_{mijt}^{TRs} Q_{mijt}^s \right. \\
& + \left. \sum_{mjk} C_{mjkt}^{TRs} Q_{mjkt}^s + \sum_{mkl} C_{mkl}^{TRs} Q_{mkl}^s \right) \dots \dots \dots (1)
\end{aligned}$$

3.6 Objective function to minimize total network flow time

This model assumes that all the echelons take approximately same amount of time to handle the product, therefore, only transportation time is considered to calculate the network flow time. The target of this objective function (f_2) is to minimize total network flow time.

$$\text{minimize } f_2 = \sum_t \Delta T_t \left\{ \sum_{s=1}^{NS} \psi_s \left(\sum_{mij} T_{ij} Q_{mijt}^s + \sum_{mjk} T_{jk} Q_{mjkt}^s + \sum_{mkl} T_{kl} Q_{mkl}^s \right) \right\} \dots \dots \dots (2)$$

3.7 Objective function to maximize demand satisfaction rate

Demand satisfaction rate is the proportion of the demand fulfilled in time period t under scenario s . Hence, it is calculated by the ratio of product flow from DC to customer zone and demand of customer zone. As the demands are considered weekly demands, it is multiplied by the duration of the time periods in weeks. This objective function (f_3) maximizes the customer demand satisfaction rate.

$$\text{maximize } f_3 = \sum_t \Delta T_t \sum_{s=1}^{NS} \psi_s \left(\frac{\sum_{mkl} Q_{mkl}^s}{\sum_{mkl} D_{mkl}^s} \right) \dots \dots \dots (3)$$

3.8 Objective function for maximizing volume flexibility

Chod et al.³³ defines volume flexibility as the “ability to change production volume”, which can be expressed as the difference between available and utilized capacity. This objective function (f_4) represents the volume flexibility which is the sum of the excess capacity multiplied by a weight factor on each echelon.

$$\begin{aligned}
\text{maximize } f_4 = & \sum_t \Delta T_t \sum_{s=1}^{NS} \psi_s \{ (\sum_{mi} P_{mit}^s - \sum_{mij} Q_{mijt}^s) \alpha_1 + (\sum_j Y_j W_j^{\max} - \sum_{mjk} Q_{mjkt}^s) + \\
& (\sum_k DC_k^{\max} - \sum_{mkl} Q_{mkl}^s) \alpha_3 \\
& \dots \dots (4)
\end{aligned}$$

These objective functions (f_1, f_2, f_3, f_4) are subject to the following constraints:

$$Q_{mijt}^s \leq Q_{mij}^{s,\max} Y_j \quad \forall m, i, j, t, s = 1, \dots, NS \quad \dots \dots (5)$$

$$Q_{mjkt}^s \leq Q_{mjk}^{s,\max} Y_j \quad \forall m, j, k, t, s = 1, \dots, NS \quad (6)$$

$$Q_{mkl}^s \leq Q_{mkl}^{s,\max} \quad \forall m, k, l, t, s = 1, \dots, NS \quad (7)$$

$$Q_{mijt}^s \geq Q_{mij}^{s,\min} Y_j \quad \forall m, i, j, t, s = 1, \dots, NS \quad (8)$$

$$Q_{mjkt}^s \geq Q_{mjk}^{s,\min} Y_j \quad \forall m, j, k, t, s = 1, \dots, NS \quad (9)$$

$$Q_{mkl}^s \geq Q_{mkl}^{s,\min} \quad \forall m, k, l, t, s = 1, \dots, NS \quad (10)$$

$$I_{mit}^{Ps} = I_{mi,t-1} + (P_{mit}^s - \sum_j Q_{mijt}^s) \Delta T \quad \forall m, i, t, s = 1, \dots, NS \quad (11)$$

$$I_{mjt}^{WHS} = I_{mj,t-1} + (\sum_i Q_{mijt}^s - \sum_k Q_{mjkt}^s) \Delta T \quad \forall m, j, t, s = 1, \dots, NS \quad (12)$$

$$I_{mkt}^{DCs} = I_{mk,t-1} + (\sum_j Q_{mjkt}^s - \sum_l Q_{mkl}^s) \Delta T \quad \forall m, k, t, s = 1, \dots, NS \quad (13)$$

$$\sum_k Q_{mkl}^s \leq D_{mkl}^s \quad \forall m, l, t, s = 1, \dots, NS \quad (14)$$

$$P_{mit}^{s,\min} \leq P_{mit}^s \leq P_{mit}^{s,\max} \quad \forall m, i, t, s = 1, \dots, NS \quad (15)$$

$$\sum_m I_{mit}^{Ps} \leq M_i^{\max} \quad \forall i, t, s = 1, \dots, NS \quad (16)$$

$$\sum_m I_{mjt}^{WHS} \leq W_j^{\max} Y_j \quad \forall j, t, s = 1, \dots, NS \quad (17)$$

$$\sum_m I_{mkt}^{DCs} \leq DC_k^{max} \quad \forall k, t, s = 1, \dots, NS \quad (18)$$

$$P_{mit}^s, I_{mit}^{Ps}, I_{mjt}^{WHS}, I_{mkt}^{DCs}, Q_{mijt}^s, Q_{mjkt}^s, Q_{mkt}^s \geq 0 \\ \forall m, i, t, s = 1, \dots, NS \quad (19)$$

Equation 5 to 10 represents transportation flow constraints. Material flow from one echelon to another should be within some minimum and maximum value. Equation 11 to 13 ensures the balance of material. Inventory at an echelon at time period t should be equal to summation of inventory on hand at beginning and difference of incoming and outgoing product. Equation 14 is for material balance in customer zone, product transported from distribution centers to customer zone should be less or equal to customer demand. Equation 15 to 18 ensures that the process variables stay within specific capacity limit and equation 19 are to maintain the non-negativity of the process variables.

4 Multi-objective optimization with NSGA-II

The mathematical model formulated in the previous section is a multi-objective model with four objective functions. The solution of this model provides a set of solutions with possible trade-offs between the objectives which is called Pareto Optimal solutions. Researchers use different techniques to solve this kind of problems, i.e. by normalizing the objectives⁷, multi-level solution approach⁶. As discussed in the literature, different algorithms were used and among them different versions of Genetic Algorithm were used. For this model, NSGA-II proposed by Deb et al.³⁴ would be used. Following section would provide a brief overview of the algorithm.

4.1 NSGA-II: Overview

According to Deb et al.²⁶, at the t^{th} iteration, a set of population (size = $2N$) is formed by combining two sets of population P_t (parent) and Q_t (children) which are sorted based on no-dominations and provided a rank. The best set of the solutions F_1 is selected for the next iteration. If there is space for more population N , then the next ranked sets $\{F_2, \dots, F_l\}$ are taken into consideration. F_1, \dots, F_l creates the new parent set P_{t+1} for next iteration which goes through tournament selection, crossover, and mutation to create the children set Q_{t+1} . The whole process

continuous until it reaches to a certain stopping criteria. This algorithm ensures elitism because it considers solutions from both previous string (P_t) and current string (Q_t).

The main strengths of this algorithm, over the others, is the fast sorting of the population, which increases the efficiency, the elitist approach which permits good strings to proceed in the generations and contributes towards better solutions, as well as the better maintaining of the variety of solutions along the Pareto-optimal frontier. Moreover, the simplification of the constraints handling is an additional feature, which permits an easy practical usage. Therefore, the NSGA-II is used as a feasible and satisfactory solving algorithm for obtaining trade-off Pareto-optimal solutions in the following section. The optimality and applicability of the algorithm are discussed after the analysis of the solutions, where a better picture of the performance is available.

5 Illustrative Example

The mathematical model developed in section 3 must be tested for two reasons, to prove the functionality, and to analyze the conflicting outcomes. Therefore, an illustrative example is designed, solved using NSGA-II algorithm, and at the end results from the tests is analyzed. This section is divided into three subsections, namely- i) Design of a Use Case Example and Data population, ii) Solving Method Characteristics, iii) Solution and Analysis.

5.1 Design of a Use Case Example and Data Population

Designing the sample problem began with the search for availability of data, and the possibility of having real business examples. As the real case data was not available, authors were forced to create a hypothetical example. The challenge in working with hypothetical data is to make it close to real life and to make the example close to real life and select the structure of the assumption, authors researched several literature on similar topic. The case study presented by Georgiadis et al.³² provided a detailed data set which was used as the basis of the

assumption. The data population was randomly generated in MS Excel 2013 within an assumed minimum and maximum range. The scenarios are considered equally likely (Probability of a scenario in time period 2 and 3 are 0.50) but, it can be calculated based on historical data.

In particular, it is chosen a four level supply chain compiled out of two plants for converting raw materials to final product, four warehouse options among them any one, two, three, or all can be chosen to satisfy the objectives, three distribution centers (DC) and three customer zones to be served. The supply chain problem is assuming production of a two products, where two potential plants can be chosen for its production. In addition to the lack of real life case, the reason of these simplifications is the mathematical complexity of the model which lays a NP-hard linear problem. All the costs are represented as Relative Money Unit (rmu). All the demands and material flows are represented as tons per week (ton/week). Transportation time is represented in hours.

A part of simulated data population (Production Cost and Demand) is provided in table 1 and 2 as example.

Table 1 Production cost of producing product m in plant i during time period t under scenario s (C_{mit}^{Ps}), rmu/s

time period $t = 1$, scenario $s = 1$		
Product (m)	Plant (i)	
	1	2
1	102	105
2	79	76
time period $t = 2$, scenario $s = 1$		
Product (m)	Plant (i)	
	1	2
1	104	101
2	78	76
time period $t = 2$, scenario $s = 2$		
Product (m)	Plant (i)	
	1	2
1	105	103
2	81	78

time period $t = 3$, scenario $s = 1$		
Product (m)	Plant (i)	
	1	2
1	106	103
2	84	81
time period $t = 3$, scenario $s = 2$		
Product (m)	Plant (i)	
	1	2
1	107	104
2	83	84

Table 2 Demand of product m from customer zone l during time period t under scenario s (D_{mlt}^s), ton/week

time period $t = 1$, scenario $s = 1$			
Product (m)	Customer zone (l)		
	1	2	3
1	650	362	521
2	383	506	515
time period $t = 2$, scenario $s = 1$			
Product (m)	Customer zone (l)		
	1	2	3
1	507	466	422
2	408	671	455
time period $t = 2$, scenario $s = 2$			
Product (m)	Customer zone (l)		
	1	2	3
1	497	659	486
2	533	354	374
time period $t = 3$, scenario $s = 1$			
Product (m)	Customer zone (l)		
	1	2	3
1	529	341	498
2	570	467	385
time period $t = 3$, scenario $s = 2$			
Product (m)	Customer zone (l)		
	1	2	3
1	589	473	309
2	362	388	442

5.3 Solving Method Characteristics

As mentioned before in section 4, a fast and elitist Non-dominated Sorting Genetic Algorithm (NSGA-II) is used for solution purpose. In order to understand the behavior of the algorithm, the code was run several times with different parameter settings. Afterwards, the following parameters were set:

- Initial population is defined by using uniform distributed random numbers between the lower and upper bounds.
- Initial population size: 700
- Maximum number of generations: 200
- Number of objective functions: 4
- Number of variables: 4 integer (Binary) variables, and 400 continuous variables.
- Number of constraints: 875

The code is implemented in Matlab R2013b, on a personal computer with Intel core i7 processor and 8GB RAM.

5.4 Result analysis

Result was analysed at three levels as various tests was done to answer the research questions. In the process, initial population was set as 700 and termination flag was set at 200th iteration. At the second stage, the range of the objective function and the result of decision variables was analysed. At the last stage, ranges of the objective functions and solutions of 404 decision variables were analysed as it provides vital information to the decision maker about the desired level of the objectives along with number of warehouse established, production rate, material flow, and inventory level for each time period and scenario.

Table 3 Range of Total Supply Chain Cost function

Objective function	Range (<i>rmu</i>)	
	Minimum value	Maximum value
Total supply chain cost (f_1)	3077710	4277040

Table 3 and figure 4 depicts that the total supply chain cost varies within the range of 3,077,710 to 4,277,040 rmu. 140,000 solution sets

lies within this range with different and spread values of variables. The graph shows that around 4,000,000 rmu, total supply chain cost becomes stable. An appreciable number of Pareto fronts lie in that area. The decision maker can choose any value from this range of costs along with the corresponding values of other objective functions.

The second function is the summation of the required time for all the products to reach in all customer zones for all time periods and scenarios. From this function one cannot tell the specific time duration that a certain product require to reach a certain customer zone at a specific time period under a specific scenario but, one can compare the solution sets and decide which will require lowest time to deliver a product. This function varies from 2,333,080 hours to 3,049,880 hours, represented in table 4 and figure 5.

Figure 4 Range of total supply chain cost

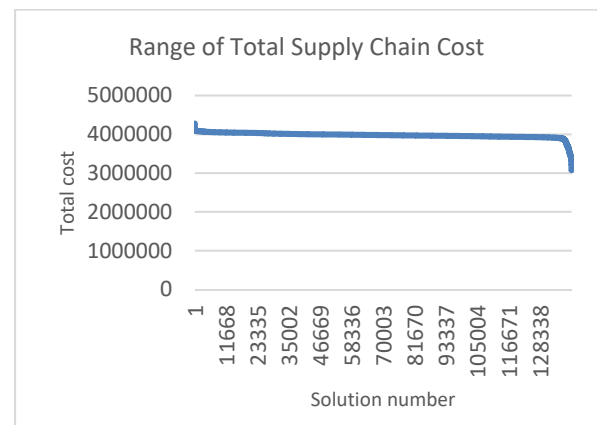


Table 4 Range of Network Flow Time function

Objective function	Range (hour)	
	Minimum value	Maximum value
Total network flow time (f_2)	2,333,080	3,049,880

There is the option to make trade off by selecting any value within this range and obviously to do that the decision maker has to choose different value of other three functions respectively. If this function is given priority then decision maker can select the solution for which total network flow time

is the lowest but, it will cause the cost function to increase.

Figure 5 Range of Network Flow Time

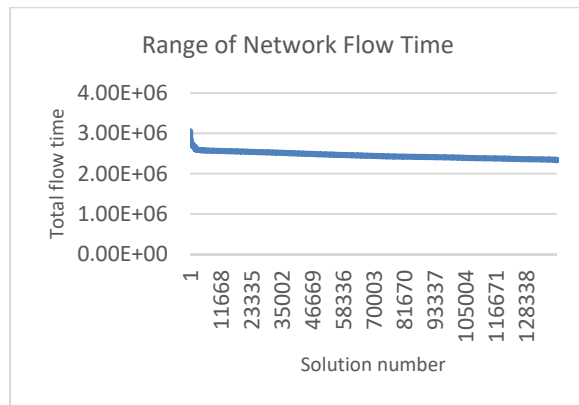


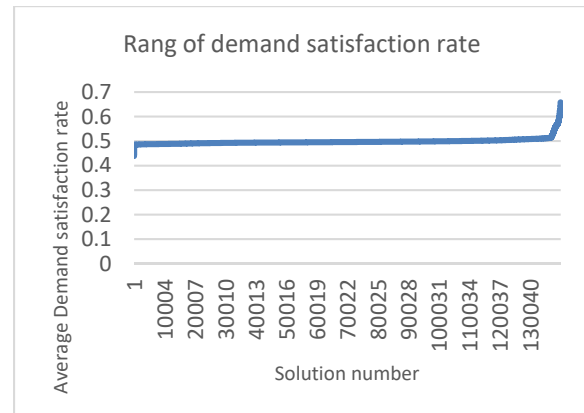
Table 5 Range of Demand satisfaction level function

Objective function	Range	
	Minimum value	Maximum value
Demand satisfaction level (f_3)	47.4507	69.0927
Average Demand satisfaction level for a specific customer zone during a week	0.439358	0.65806

Unlike the previous two objective functions, this function tries to maximize its value. The ranges of this function are presented in table 5. It ranges from 47.4507 to 69.0927. From this value the percentage of demand satisfied cannot be understood because, this objective function value is the summation of the entire weekly demand satisfaction rate for all the customer zones, products and time periods. Further calculation was done (f_3 / 4 weeks per time period/ 3 time period/ 3 customer zone) to determine the average demand satisfaction level for each product at each customer zone in a week and their range is 0.439358 to 0.65806, presented in figure 6. That means maximum 66% (approximately) demand can be satisfied for a solution set. Decision maker can select among this range according to business target. As demand satisfaction level

increase, cost function will increase surely and there is an option of trade-off for the decision maker.

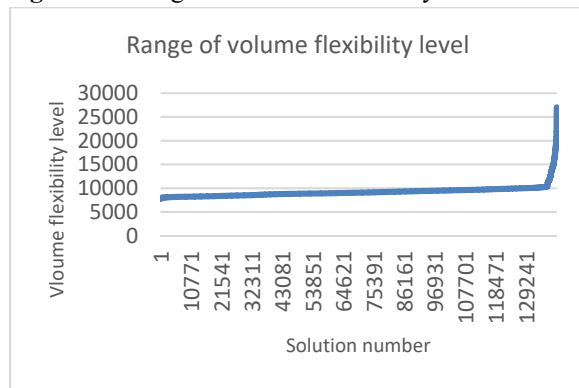
Figure 6 Range of Demand Satisfaction Level



Volume flexibility is the available capacity which can be used to handle the uncertainty. This objective function represents the total volume flexibility for the complete time frame and all the echelons. If average volume flexibility is calculated $\{f_4/ 4 \text{ weeks per time period}/ 5 \text{ scenarios}/ (2 \text{ plants} \times 4 \text{ warehouse} \times 3 \text{ Distribution center})\}$ for a plant or warehouse or distribution center, its range will be 16 to 56 (approximately) ton per week. The reason behind very low volume flexibility can be explained by the low demand satisfaction rate. As the organization cannot satisfy all the demands, there would be very low chance of flexibility. For this example, this object seems insignificant as the demand fluctuation is not very high. But, in situations like high demand-low demand scenario, this objective will help significantly in decision making. Decision maker can trade-off the flexibility with the other objective functions according to the situation or policy.

Table 6 Range of Volume Flexibility function

Objective function	Range (ton)	
	Minimum value	Maximum value
Volume Flexibility (f_4)	7770.732	27001.43
Average volume flexibility in each establishment for a week	16.18	56.25

Figure 7 Range of Volume Flexibility

Presenting the characteristic of the objective functions individually, the process of analysis provides a basis for continuing and analysing the conflicted trade-offs between the objectives. Clearly, the aim of this model is to analyse the interaction between the objective functions, and to serve the decision-making process with data that will offer a variety of different solutions. Even though at this stage, the decision maker should step up with higher-level criteria for selecting solutions, the analysis is proceeding without it. For example, the decision maker can set the priorities of having the most cost effective supply chain by ensuring minimum transportation time, while the customer service level and volume flexibility can have secondary importance. It can be even chosen the lowest cost solution for selecting cost effective options and for employing the low cost warehouse and without paying attention to the customer service level and flexibility. However, for this research that kind of data is not necessary, in fact presenting the ability of the optimization has nothing to do with the higher-level criteria. Therefore, out of the non-dominated set of solution, for the analysis of the multi-objective optimization model, it is decided to pick up the solutions that are giving an equal importance to all four of the objectives.

In addition to the previous discussion, some graphs with the Pareto-Optimal solutions are presented. From figures 10 - 14, it can be seen how the solutions are initiating with a bigger population as highlighted by the figures attached below for lower generations, and afterwards are converging towards the most optimal line/surface. Objective function 3 and 4 has lower value compared to the objective

function 1 and 2. For the purpose of scalarization, objective function 3 and 4 is multiplied by 10^8 . Moreover, NSGA-II always minimize the objective functions so, objective function 3 and 4 is represented in invers form. At the last stage of analysis, 404 decision variables has been elaborated one solution set taken from the Pareto front generated at 200th generation and presented in table 7.

Table 7 Value of objective functions for a set of solution

Objective functions	Values
Total supply chain cost (f_1)	4016149.799
Network flow time (f_2)	2348823.428
Demand satisfaction level (f_3)	52.85
Volume flexibility (f_4)	8333.33

The value of four objective functions are given in the table 7 and to acquire these values the decision variables are presented in appendix A with their related values. X1 to X4 are the four binary decision variables used for warehouse selection decision. If any of these variables results 1, then that warehouse is selected for establishment.

Variables X5 to X24 represents the production rate of each product at each plant for all the time periods and possible scenarios. Variable X5 to X14 denotes production rate of product one and X15 to X24 are for production rate of second product in the sequence of time period and scenario.

X25 to X104 has been used to denote the material flow from plant to warehouse. Among these variables, X25 to X64 represent the flow rate of product one from both the plants at time period t under scenario s . Variables X25, X30, X35 and X40 symbolize the flow rate of product one produced at plant one and transferred to four selected warehouse during time period one and scenario one. Similarly other variables represents production rates of products at different time period and scenarios.

X105 to X224 has been used to represent the flow rate of both the products from warehouses to the distribution centers where X105 to X164 are used for

product number one and rest of the variables are used for product number two. X165, X180, X195, X210 represent the flow rate of product one to distribution center one from all the warehouses.

Variable X225 to X314 denotes the product flow rate from distribution centers to customer zones which is driven by demand at different customer zones. X225 to X269 are used for flow rate of product one and among them X225 to X239 are transferred from distribution center one, X240 to X253 represent the flow rate of product one to different customer zones from distribution center two during all three time periods and corresponding scenarios.

Variable X315 to X319 represents the inventory level of product one at plant one, X320 to X324 at plant two. X325 to X329 has been used for inventory level of product two at plant one and X330 to X334 denote inventory level of product two at plant two.

Similarly, variables X335 to X375 represents inventory level of products at different warehouses during all three time periods and corresponding time periods and X375 to X404 has been used to denote inventory level at distribution centers similarly.

The variables represents here represents how much to produce, how much to transport from one specific point to another, how much product should be as inventory in a certain time period and scenario. Moreover, it also shows where and how many warehouses is required to achieve this objective. This model provides a good deal of flexibility as number of products, manufacturing plants, distribution centers, customer zones and warehouse options can be changed to accommodate a specific problem. In addition, establishment of manufacturing plant and distribution center can be considered as decision variables. For this example, we assumed that the supply chain already has two plant and three distribution centers. Instead of that, suitable locations can be considered for the establishment of plants and distribution centers. That will make the model a facility location model for multiple echelon and inclusion of uncertainty will make it very close to real world.

6 Conclusion and Recommendation

The objective of this research was to develop a new supply chain network design model which can help decision making by providing trade-off solutions. After comprehensive literature review research gaps in the field of supply chain network optimization was identified and the objectives for the research design were formed. The proposed model was formulated as MILP model with four objective functions. The objective functions are minimizing total supply chain cost and network flow time along with maximizing demand satisfaction level and volume flexibility considering multi-period demand and cost uncertainty. The model is applied to a hypothetical case example designed to test the functionality of the model and to analyse the result. NSGA-II algorithm was used to solve the model. The model provides a large number of trade-off solutions with corresponding material production, flow, and inventory level for each echelon. Currently this model provides strategic level decision but, with further modification it can be used to provide tactical level decisions. Moreover, it provides facility location decision only for warehouse which can be changed for other echelons.

For future studies, authors recommend considering supplier uncertainty and use of stochastic framework for uncertainty. Moreover, more advanced solution techniques should be explored to achieve better quality solution within shortest possible time.

References

- [1] Childerhouse P, Towill DR. Simplified material flow holds the key to supply chain integration. *Omega*. 2003;31(1):17-27.
- [2] Shahparvari S, Chiniforooshan P, Abareshi A. Designing an integrated multi-objective supply chain network considering volume flexibility. In: *Proceedings of the World Congress on Engineering and Computer Science*. Vol 2.; 2013:1168-1173.
- [3] Guillén G, Mele FD, Bagajewicz MJ, Espuna A, Puigjaner L. Multiobjective supply chain design under uncertainty. *Chem Eng Sci*. 2005;60(6):1535-1553.

- [4] Mittal AK, Thaker CS, Sutaria GN. Multi-objective supply chain model through an ant colony optimization approach. In: *International Conference on Computer Communication and Networks CSI-COMNET-2011*. ; 2011.
- [5] Melo MT, Nickel S, Saldanha-Da-Gama F. Facility location and supply chain management—A review. *Eur J Oper Res*. 2009;196(2):401-412.
- [6] Sabri EH, Beamon BM. A multi-objective approach to simultaneous strategic and operational planning in supply chain design. *Omega*. 2000;28(5):581-598. doi:10.1016/S0305-0483(99)00080-8.
- [7] Yuce B, Mastrocinque E, Lambiase A, Packianather MS, Pham DT. A multi-objective supply chain optimisation using enhanced Bees Algorithm with adaptive neighbourhood search and site abandonment strategy. *Swarm Evol Comput*. 2014;18:71-82.
- [8] Baghalian A, Rezapour S, Farahani RZ. Robust supply chain network design with service level against disruptions and demand uncertainties: A real-life case. *Eur J Oper Res*. 2013;227(1):199-215.
- [9] Morteza L, Kuan YW. A review of modelling approaches for supply chain planning under uncertainty. In: *ICSSSM12*. IEEE; 2012:197-203.
- [10] Altıparmak F, Gen M, Lin L, Paksoy T. A genetic algorithm approach for multi-objective optimization of supply chain networks. *Comput Ind Eng*. 2006;51(1):196-215. doi:10.1016/j.cie.2006.07.011.
- [11] Dzupire NC, Nkansah-Gyekye Y. A multi-stage supply chain network optimization using genetic algorithms. *arXiv Prepr arXiv14080614*. 2014.
- [12] IVANOVSKI D. Multi-objective optimization for sustainable supply chain design. A triple bottom line approach. 2014.
- [13] Jin M, Ma R, Yao L, Ren P. An effective heuristic algorithm for robust supply chain network design under uncertainty. *Appl Math Inf Sci*. 2014;8(2):819.
- [14] Mirzapour Al-e-Hashem SMJ, Baboli A, Sadjadi SJ, Aryanezhad MB. A multiobjective stochastic production-distribution planning problem in an uncertain environment considering risk and workers productivity. *Math Probl Eng*. 2011;2011.
- [15] Moncayo-Martínez LA, Zhang DZ. Multi-objective ant colony optimisation: A meta-heuristic approach to supply chain design. *Int J Prod Econ*. 2011;131(1):407-420. doi:10.1016/j.ijpe.2010.11.026.
- [16] Wang F, Lai X, Shi N. A multi-objective optimization for green supply chain network design. *Decis Support Syst*. 2011;51(2):262-269. doi:10.1016/j.dss.2010.11.020.
- [17] Pinto EG. Supply chain optimization using multi-objective evolutionary algorithms. *Retrieved December*. 2004;15:2004.
- [18] Vaklieva-Bancheva N, Espuña A, Shopova E, Puigjaner L, Ivanov B. Multi-objective optimization of dairy supply chain. In: *Computer Aided Chemical Engineering*. Vol 24. Elsevier; 2007:781-786.
- [19] Longinidis P, Georgiadis MC. Managing the trade-offs between financial performance and credit solvency in the optimal design of supply chain networks under economic uncertainty. *Comput Chem Eng*. 2013;48:264-279.
- [20] Gen M, Altıparmak F, Lin L. A genetic algorithm for two-stage transportation problem using priority-based encoding. *OR Spectr*. 2006;28(3):337-354. doi:10.1007/s00291-005-0029-9.
- [21] Moncayo-Martínez LA, Zhang DZ. A Multi-objective Optimization for Supply Chain Network using Intelligent Water Drop. In: *IIE Annual Conference. Proceedings*. Institute of Industrial and Systems Engineers (IISE); 2014:3191.
- [22] Liu S, Papageorgiou LG. Multiobjective optimisation of production, distribution and capacity planning of global supply chains in the process industry. *Omega*. 2013;41(2):369-382.
- [23] Hasan S, Eckert C, Earl C. Supply chain collaboration under uncertainty. 2012.

- [24] Pujawan IN, Er M, Kritchanchai D, Somboonwivat T. Uncertainty and schedule instability in supply chain: insights from case studies. *Int J Serv Oper Manag.* 2014;19(4):468-490.
- [25] Kazemi N, Ehsani E, Glock CH, Schwindl K. A mathematical programming model for a multi-objective supplier selection and order allocation problem with fuzzy objectives. *Int J Serv Oper Manag.* 2015;21(4):435-465.
- [26] Deb K, Agrawal S, Pratap A, Meyarivan T. A fast elitist non-dominated sorting genetic algorithm for multi-objective optimization: NSGA-II. In: *International Conference on Parallel Problem Solving from Nature*. Springer; 2000:849-858.
- [27] Guria C, Bhattacharya PK, Gupta SK. Multi-objective optimization of reverse osmosis desalination units using different adaptations of the non-dominated sorting genetic algorithm (NSGA). *Comput Chem Eng.* 2005;29(9):1977-1995.
- [28] Murugan P, Kannan S, Baskar S. NSGA-II algorithm for multi-objective generation expansion planning problem. *Electr Power Syst Res.* 2009;79(4):622-628.
- [29] Supasansanee L, Kasiphongphaisan P. *Logistics Management in Retail Industry: A Case Study of 7-Eleven in Thailand.*; 2009.
- [30] Matinrad N, Roghanian E, Rasi Z. Supply chain network optimization: A review of classification, models, solution techniques and future research. *Uncertain Supply Chain Manag.* 2013;1(1):1-24.
- [31] Sabri EH, Beamon BM. A multi-objective approach to simultaneous strategic and operational planning in supply chain design. *Omega.* 2000;28(5):581-598.
- [32] Georgiadis MC, Tsiakis P, Longinidis P, Sofioglou MK. Optimal design of supply chain networks under uncertain transient demand variations. *Omega.* 2011;39(3):254-272.
- [33] Chod J, Rudi N, Van Mieghem JA. Mix, time, and volume flexibility: Valuation and corporate diversification. *Rev Bus Econ Lit.* 2012;57(3).
- [34] Deb K. Multi-objective optimization. In: *Search Methodologies*. Springer; 2014:403-449.

MARINE PROPELLER DESIGN USING CFD TOOLS

Goutam Kumar Saha^{1,a)} Md. Hayatul Islam Maruf^{2,b)} and Md. Rakibul Hasan^{2,c)}

¹Department of Naval Architecture and Marine Engineering, BUET, Dhaka

²Department of Naval Architecture and Marine Engineering, Sonargaon University, Dhaka

a) gksaha2007@gmail.com

b) ih_maruf@yahoo.com

c) rakibname@gmail.com

Abstract. A marine propeller generates adequate thrust to propel a vessel at some design speed. So, propeller is the core to optimum performance on a ship. Considerations are made to match the engine's power and shaft speed, as well as the size of the vessel and the ship's operating speed, with an appropriately designed propeller. As marine propeller has complicated geometries, the flow around the propeller is complicated. In generally, the performance characteristics of a propeller is determined and analyze by experiments like open water and self-propulsion model test which are costly at the initial stage of the design. Numerical analysis using Computational Fluid Dynamics simulations could be an important alternative on this case. This study presents the investigation of marine propeller hydrodynamic performance and parameters through Computational Fluid Dynamic analysis. In this paper, a B-series propeller model is developed with respect to some design constraints such as ship speed, vessel draft etc. and analyzed the performance using CFD tools. In this analysis, we consider Realizable $k-\omega$ Turbulence Model & Multiple Reference Frame Model. Results found that all thrust coefficient (K_T) and torque coefficient $10 (K_Q)$ decreases with the increasing advance coefficient (J). The efficiency of propeller performance had also consistently showed characteristic trend of nonlinear increases to a peak an optimum value before decreasing drastically with increasing J value. The numerical results obtained from CFD Tool are compared with theoretical available publish data.

Keywords: Propeller, CFD, ANSYS, B-Series Propeller

INTRODUCTION

Marine propulsion is the mechanism or system used to generate thrust to move a ship or boat across water. When we consider about ship designs and design improvements, the propulsive efficiency is one of the most important issues. The marine propellers are necessary to be very efficient. The propulsive efficiency for ship designs is mandatory to be predicted and determined by model tests and full-scale observations in pre-design stage. Furthermore, there are many approaches and analysis have been done by researchers and naval architects in order to achieve the increasingly propulsive efficiency by comparing and investigating the ship hulls, propellers, rudders and energy saving devices. High marine fuel costs and low freight rates are causing operators to seek ways to boost ship efficiency.

Advanced ship propulsion solutions are one way to achieve considerable improvements in this regard but require highly detailed concept, design and construction processes. Model tests of self-propulsion were conventionally the only way to determine and evaluate the characteristics of hull-propeller interaction, the powering performance and the propulsion parameters of the ship. With the rapid advances in the field of computational fluid dynamics (CFD), numerical simulations of ship self-propulsion

have recently gained increasing attention. Due to the increased capabilities of numerical flow simulations, it has become possible to make Computational Fluid Dynamics (CFD) analyses of self-propulsion calculations of ships with propellers. Computational fluid dynamics (CFD) provides ways of simulating flow fields around different geometries using numerical methods and established algorithms. During recent years, considerable progress in the field of computer science has contributed to the decrease of computational costs of CFD simulations, making it more accessible for practical applications. Nowadays, the role of CFD methods is increasing in most fluid dynamic's applications including the process of ship propeller design. Simulating the aforementioned experiments provides the opportunity to obtain desired results by analyzing calculated flow characteristics. It can be a practical way of obtaining valid results at relatively low costs and in reasonable time in relation to the real experiments. Since the self-propulsion test simulation is still quite expensive and time demanding, the common practice is to simulate only the open water test and to use its results for the determination of self-propulsion characteristics. It can be done by considering established interaction factors, which account for the interaction between the hull resistance and open water characteristics of the propeller. The difference between approaches lies in

the level of simplification of the actual phenomenon as a trade-off between accuracy and CPU efficiency. The following two approaches, multiple frame of reference (MRF) for four bladed propellers with symmetric wall boundary condition and Steady simulation with rotating frame for simulating flow around a propeller are used and compared with them.

For the purpose of this research work steady state simulations with MRF model for a four bladed and complete propeller geometry were performed for different operating points of the propeller model. Thrust and Torque with respect to the advance ratio are obtained. As stated earlier, self-propulsion test simulation is quite expensive and time demanding. When modeling full interaction between the ship and the propeller, the main problem is the large difference between the time scales of the propeller and hull flow.

Different researchers are works on marine propellers based on CFD and FEA.

GOVERNING EQUATION

A propeller is a rotating fan like structure which is used to propel the ship by using the power generated and transmitted by the main engine of the ship. The transmitted power is converted from rotational motion to generate a thrust which imparts momentum to the water, resulting in a force that acts on the ship and pushes it forward. The simplest way to analyze propeller performance is to measure the thrust (T) produced by the propeller and the torque (Q) used to drive the propeller. Efficiency can be defined as the ratio of the acquired power in thrust production to the power used to drive the propeller. In the marine context, thrust and torque are usually given as non-dimensional measures as a function of a non-dimensional speed called the advance coefficient. The definitions of thrust- and torque coefficients, K_T and K_Q , and the advance coefficient, J , are given as

$$K_T = \frac{T}{\rho n^2 D^4}$$

$$K_Q = \frac{Q}{\rho n^2 D^5}$$

$$J = \frac{V_A}{nD}$$

Above, propeller diameter is denoted as D , n is the number of propeller revolutions in one second, ρ is the water density and V_A is the advance speed, for example the speed of a ship. The coefficients are found by applying dimensional analysis and assuming that free surfaces have no effect on the propeller performance. Under such conditions the coefficients are theoretically identical for all geometrically similar blade forms. The definition of efficiency can be written as

$$\eta = \frac{T \cdot V_A}{2\pi n Q} = \frac{K_T J}{K_Q 2\pi} \dots\dots\dots (1)$$

The thrust and torque coefficients (K_T and K_Q) being similar for all cases with an identical blade shape is not entirely true. There are several factors that affect propeller performance even with a constant advance coefficient J .

Ship flows are governed by the three basic conservation laws for mass, momentum and energy, collectively referred to as the Navier-Stokes equations. The first law is mass conservation law-continuity equation which states that the rate of change of mass in an infinitesimally small control volume equals the rate of mass flux through its bounding surface.

Mass conservation – Continuity equation:

$$\frac{\partial \rho}{\partial t} + \nabla \cdot (\rho \mathbf{V}) = 0 \dots\dots\dots (2)$$

where

∇ is the differential operator ($\partial/\partial x, \partial/\partial y, \partial/\partial z$)

ρ is water density (kg/m^3)

$\mathbf{V} = (u, v, w)$, fluid velocity (m/s)

Mass conservation – Continuity equation:

$$\frac{\partial(\rho u)}{\partial t} + \nabla \cdot (\rho u \mathbf{V}) = -\frac{\partial p}{\partial x} + \frac{\partial \tau_{xx}}{\partial x} + \frac{\partial \tau_{yx}}{\partial y} + \frac{\partial \tau_{zx}}{\partial z} + \rho f_x \quad (3)$$

$$\frac{\partial(\rho v)}{\partial t} + \nabla \cdot (\rho v \mathbf{V}) = -\frac{\partial p}{\partial y} + \frac{\partial \tau_{xy}}{\partial x} + \frac{\partial \tau_{yy}}{\partial y} + \frac{\partial \tau_{zy}}{\partial z} + \rho f_y \quad (4)$$

$$\frac{\partial(\rho w)}{\partial t} + \nabla \cdot (\rho w \mathbf{V}) = -\frac{\partial p}{\partial z} + \frac{\partial \tau_{xz}}{\partial x} + \frac{\partial \tau_{yz}}{\partial y} + \frac{\partial \tau_{zz}}{\partial z} + \rho f_z \quad (5)$$

Where, P is pressure, τ_{ij} is viscous stresses and f_i is body force.

Energy conservation – Energy equation:

$$\begin{aligned} \frac{\partial}{\partial t} \left[\rho \left(e + \frac{V^2}{2} \right) \right] + \nabla \cdot \left[\rho \left(e + \frac{V^2}{2} \right) \mathbf{V} \right] \\ = p q + \frac{\partial}{\partial x} \left(k \frac{\partial T}{\partial x} \right) + \frac{\partial}{\partial y} \left(k \frac{\partial T}{\partial y} \right) + \frac{\partial}{\partial z} \left(k \frac{\partial T}{\partial z} \right) \\ - \frac{\partial(u p)}{\partial x} - \frac{\partial(v p)}{\partial y} - \frac{\partial(w p)}{\partial z} + \frac{\partial(u \tau_{xx})}{\partial x} \\ + \frac{\partial(u \tau_{yx})}{\partial y} + \frac{\partial(u \tau_{zx})}{\partial z} + \frac{\partial(v \tau_{xy})}{\partial x} + \frac{\partial(v \tau_{yy})}{\partial y} \\ + \frac{\partial(v \tau_{zy})}{\partial z} + \frac{\partial(w \tau_{xz})}{\partial x} + \frac{\partial(w \tau_{yz})}{\partial y} + \frac{\partial(w \tau_{zz})}{\partial z} + \rho f \cdot \mathbf{V} \dots\dots\dots (6) \end{aligned}$$

MODEL PROPELLER

For the CFD analysis, the first step is to design a 3D model of propeller. By using the basic data of B-Series propeller, a 3D propeller model is developed for analysis and is shown in Fig. 1. Particulars and geometric properties of the model propeller are shown in Table 1 and Table 2.

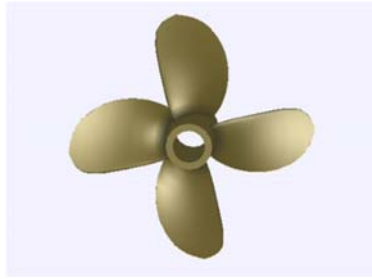


Figure 1: 3D Model Propeller

Table 1: Particulars of four bladed propeller

Particulars	Dimensions
Delivered Power, P_D	578.66 kW
BAR	0.55
Pitch Diameter ratio	0.69
Propeller Pitch	1.2486 m
Propeller Diameter	1.6029 m
Rake of GL aft	0°
Skew Angle	17.6°

Table 2: geometric properties of propeller

r/r_h	A	B	C	T (M)	R	MID C-GL	C/D
0.2	0.226	0.128	0.366	0.058	0.1603	-0.0429	0.2285
0.3	0.254	0.145	0.415	0.051	0.2404	-0.0469	0.2588
0.4	0.271	0.158	0.452	0.045	0.3206	-0.0456	0.2819
0.5	0.278	0.166	0.474	0.038	0.4007	-0.0408	0.2959
0.6	0.270	0.187	0.482	0.032	0.4809	-0.0294	0.3007
0.7	0.248	0.209	0.473	0.025	0.5610	-0.0113	0.2948
0.8	0.201	0.208	0.434	0.018	0.6412	0.0161	0.2709
0.9	0.122	0.174	0.349	0.012	0.7213	0.0520	0.2175
0.925	0.092	0.154	0.307	0.010	0.7414	0.0617	0.1915
0.95	0.051	0.123	0.246	0.008	0.7614	0.0720	0.1532
0.975	-0.007	0.076	0.152	0.006	0.7814	0.0834	0.0951
1.0	-0.093	0.005	0.010	0.005	0.8015	0.0974	0.0060

Where,

a = distance between leading edge and generator line at r.

b = distance between leading edge and location of maximum thickness.

c = chord length of blade section at radius r.

t = maximum blade section thickness at radius r.

PROPELLER PERFORMANCE ANALYSIS USING ANSYS FLUENT

ANSYS Fluent is a state-of-the-art computer program for modeling fluid flow, heat transfer, and chemical reactions in complex geometries. ANSYS Fluent provides complete mesh flexibility, including the ability to solve your flow problems using unstructured meshes that can be generated about complex geometries with relative ease. Supported mesh types include 2D triangular/ quadrilateral, 3D tetrahedral/ hexahedral/ pyramid/ wedge/ polyhedral, and mixed (hybrid) meshes. ANSYS Fluent also enables us to refine or coarsen our mesh based on the flow solution.

It is mentioned that generated mesh can be read into ANSYS Fluent, or, for 3D geometries mesh can be, create using the meshing mode of Fluent. All remaining operations are performed within the solution mode of Fluent, including setting boundary

conditions, defining fluid properties, executing the solution, refining the mesh, and post processing and viewing the results.

After determination of the important features of the problem that want to solve, the basic procedural steps are shown below have followed.

1. Define the modeling goals.
2. Create the model geometry and mesh.
3. Set up the solver and physical models.
4. Compute and monitor the solution.
5. Examine and save the results.
6. Consider revisions to the numerical or physical model parameters.

Defining Model Geometry & Meshing

At the beginning of the process, the propeller geometry is imported into Ansys Design Modeler that was created in iges format and domain is generated as shown in Fig. 2. The Cartesian coordinates system is used, where x, y and z. The origin was located at the center of the hub, and positive directions are upstream, starboard and downstream. The domain dimensions were shown in Fig. 3. The solution field was divided into global and sub-domain. The sub-domain frame simulates the propeller rotation and employs the Coriolis acceleration terms in the governing equations for the fluid. The global frame surrounds the sub-domain frame. The global frame is a circular cylinder with 2 m radius and length is 12 m. The distance between the sub-domain frame and inlet is 1.991 m, while it is 9.991 m for the outlet. The sub-domain is also cylinder with a diameter of 0.018 m and length 0.018 m. Details of meshing properties are shown in Table 3 to Table 7.

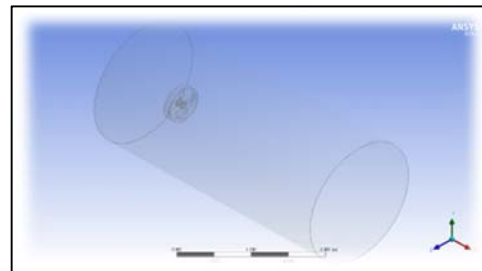


Figure 2: Propeller with Domain & Sub-Domain

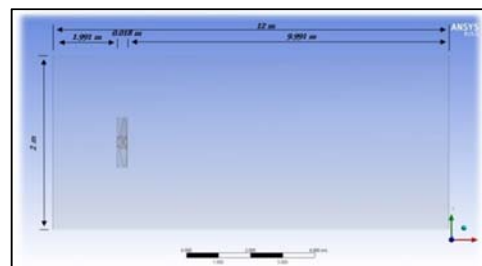


Figure 3: Dimensions of Domain & Sub-Domain

The generation of a suitable and fine grid is a crucial step in the simulation process. Promoting the negligible error in the procedure of the simulation and reducing the computational time for the program are the main issues for generating the mesh. There are two main methods to generate the mesh, one is to use the algebraic approach to make the grids, and the other one is to apply the partial differential equations to generate grids. The unstructured grids have the advantages of the lack of restriction on where points can be placed, in other words, it means it is possible to provide an automation of generation with a high degree. The mesh applied in these propeller models is the unstructured mesh which is also called the auto volume mesh, usually obtained after setting up all the parameters like inflations, the growth rate, the face sizing, the contact sizing, and the body sizing. This kind of mesh will reduce the cost of humanity but required a heavy work for the CPU of the computer. Therefore, reducing a very long computational time for each simulation is the basis issue of making mesh here. The models of the propellers are 3-D models, so the three-dimensional mesh is applied to the analysis of the 3-D models.

Table 3: Mesh Options & Its Position

Mesh Options	Position
Mapped Face Meshing	Outer Wall of Main Domain
Patch Conforming Method	Main Domain
Face Sizing	Propeller Blade
Inflation	Outer Wall of Main Domain

Table 4: Global meshing

Physics Preference	CFD
Solver Preference	Fluent
Element Order	Program Controlled
Size Function	Proximity & Curvature
Max Face Size	0.2 m
Mesh Defeaturing Size	2.74e-004 m
Growth Rate	1.15
Min Size	5.48e-004 m
Max Tet Size	0.3 m
Curvature Normal Angle	5°
Proximity Min Size	5.48e-004 m
Num Cells Across Gap	5
Boundary Box Diagonal	14.6620 m
Average Surface Area	11.2310 m ²
Minimum Edge Length	9.62e-003 m

Table 5: Inflation

Geometry	Main Domain
Boundary Scoping Method	Outer enclosure wall
Inflation Option	First Layer Thickness
First Layer Height	1.e-004 m
Maximum Layers	14
Growth Rate	1.2
Inflation Algorithm	Pre

Table 6: Statistics

Nodes	58,97,564
Elements	40,60,580

Table 7: Quality

Mesh Metric	Skewness
Min	1.3515e ⁻⁰⁰⁶
Max	0.84961
Average	0.2217
Standard Deviation	0.11467

Solver Setup

After all the alterations and adjustments are done in the meshing, the set up needs to be checked and modified before running the solutions.

This is done by the following ways

- Select the setup option from the work space.
- Select 3D for dimension
- Select Processing Option Serial

In the research work we will use, pressure-based solver type, absolute velocity function, transient time condition. For model properties, Set the viscous model is k-epsilon (2 equation), Realizable k-epsilon model and scalable wall function treatment near wall.

For materials properties, as the propeller is submerged at sea water, we select water for fluid and as our propeller is solid, we consider aluminum as a solid material. The density of water is 1025kg/m³

In cell zone conditions, Main Domain is the stationary domains and Sub Domain is a rotating domain due to the blades part of the propeller located in it. Analysis type is a transient mode here in. And initial time in the automatic with value option is chosen, started with time at zero second. Details of cell zones conditions explained Table 8.

When the fluid flow goes through Main Domain and reaches the interface 1, which is in contact with the rotating propeller, a growing velocity will be applied to the flow. Accelerated flow goes across the interface 2 to pass through Main Domain whereas the mass flow at outlet is obtained. In the stationary domain, boundary conditions like the inflation layers and contacting sizing are imposed to provide an appropriate stationary environment. Details of boundary conditions are explained in Table 9.

Table 8: Cell Zone Conditions

Sub-Domain	Motion	Frame Motion
	Relative to Cell Zone	Absolute
	Rotation-Axis Origin	0,0,0
	Rotation-Axis Direction	1,0,0
	Rotational Velocity	-400
Main Domain	Motion	Stationary

Table 9: Boundary Conditions

Velocity Inlet	Reference Frame	Absolute
	Velocity Magnitude	Diff. Velocity Corresponding to J
	Coordinate System	(X, Y, Z) = (1,0,0)
Pressure Outlet	Backflow Reference Frame	Absolute
	Gauge Pressure	0 Pascal
	Backflow Direction	Normal to Boundary
Outer enclosure wall	Wall Motion	Stationary
	Shear Condition	No Slip
Propeller Blade	Wall Motion	Stationary
	Shear Condition	No Slip

Solution Method

The SIMPLE (Semi Implicit Pressure Linked Equations) scheme is used in the transient flow analyses. An implicit scheme is used when evaluating over time steps in the transient analysis. The second order upwind scheme is used for the Pressure, Momentum, Turbulent Kinetic Energy and Turbulent Dissipation Rate. The first order scheme is less accurate than the second order, but the stability is better.

And Finally, for starting the simulation we set the time step size for 0.003s for MRF. This value has to be matched with the rotating speed, when the sub domain is rotating, it should not skip any mesh element. In other words, the step size has to be smaller than mesh element, so all elements will be taken account in calculation. Otherwise it will be less precision in the calculation. More time step size and more iteration value increase, more time will be necessary for calculation.

RESULTS AND DISCUSSION

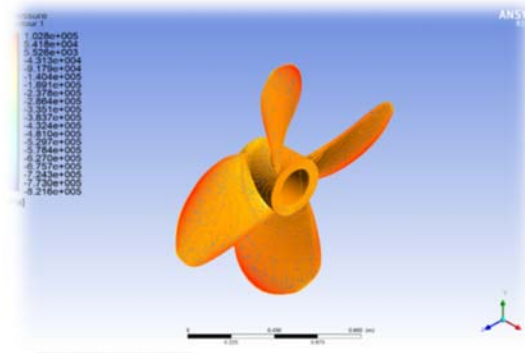
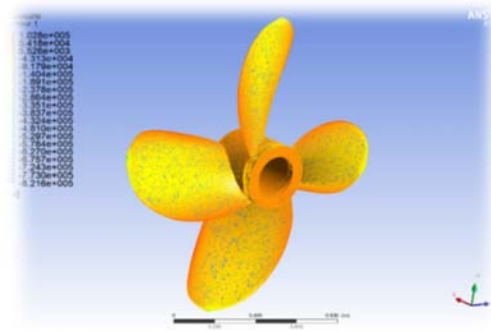
The continuous information has been contained in the exact solution of the differential equation describing the physical model would have been replaced with discrete values, in which, all grid nodes would have interactive properties between them and the neighbor nodes. A finite volume technique has been used in FLUENT package to convert the governing equations to algebraic equations that can be solved numerically. The convergence can be monitored dynamically by checking residuals. The residuals must be kept on decreasing from the start to end of the iterations, in this study the scaled residuals decrease to 10^{-5} for all equations. The numerical results have been obtained using about 1000 iterations to obtain a suitable level of solution convergence.

A direct comparison between numerical results and the experimental results has been carried out to validate the numerical model in the studied range. Validation has been carried out by calculating the thrust and torque coefficients at cases prescribed in experimental work results. The efficiency has been calculated and has been plotted to complete the total behavior of the marine propeller model. Eight different cases have been investigated as shown in Table 10:

Table 10: Values for Thrust and Torque Coefficient from CFD

Case	V_A	J	K_T	K_Q
1	1.0686	0.1	0.297	0.034
2	2.1372	0.2	0.266	0.031
3	3.2058	0.3	0.232	0.028
4	4.2744	0.4	0.196	0.025
5	5.343	0.5	0.158	0.021
6	6.4116	0.6	0.120	0.018
7	7.4802	0.7	0.079	0.014
8	8.5488	0.8	0.033	0.010

Pressure contour of propeller face and back are obtained at 400 rpm, considering 4.144 m/s inlet velocity and zero outlet gauge pressure. These contours are shown in Fig. 4 and Fig. 5. Here the maximum pressure is $1.028e^{+005}$ Pa. Also, the minimum pressure is $-8.216e^{+005}$ Pa.

**Figure 4:** Pressure contour of Propeller Face**Figure 5:** Pressure contour of Propeller Back

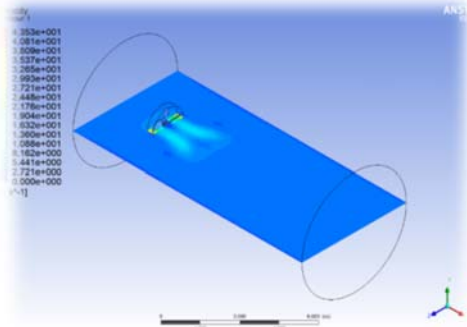


Figure 6: Velocity contour at stationary frame

The velocity contour at stationary frame is calculate at 4.144 ms^{-1} velocity, and 400 rpm and is shown in Fig. 6. At this boundary condition, the maximum velocity is $4.353 \times 10^1 \text{ ms}^{-1}$ and the minimum velocity is 0.

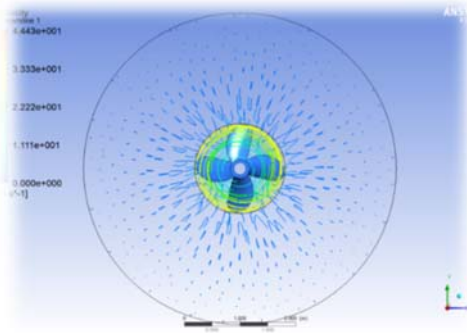


Figure 7: Velocity Streamline (sectional view)

The velocity streamlines are shown in Fig. 7 and 8. This are obtained for 400 rpm of propeller with inlet velocity 4.144 ms^{-1} . The maximum velocity of a streamline is found $4.443 \times 10^1 \text{ m/s}$ and the minimum are 0.

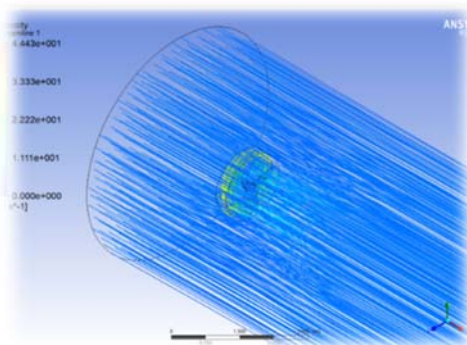


Figure 8: Velocity Streamline (Perspective view)

In order to validate the numerical results of CFD, the thrust coefficient and torque coefficient are also

calculated (Table 11) using empirical method (Shiodu, A. et al. 2013) explained below:

$$K_Q = \sum_{n=1}^{47} C_n(J) S_n \left(\frac{P}{D} \right) t_n \left(\frac{A_E}{A_0} \right)^{u_n} (Z)^{v_n}$$

$$K_T = \sum_{n=1}^{39} C_n(J) S_n \left(\frac{P}{D} \right) t_n \left(\frac{A_E}{A_0} \right)^{u_n} (Z)^{v_n}$$

Table 11: Value for Thrust and Torque Coefficient from Empirical Formula

CASE	V_A	J	K_T	K_Q
1	1.0686	0.1	0.262	0.029
2	2.1372	0.2	0.231	0.026
3	3.2058	0.3	0.197	0.023
4	4.2744	0.4	0.159	0.020
5	5.343	0.5	0.119	0.016
6	6.4116	0.6	0.076	0.012
7	7.4802	0.7	0.030	0.008
8	8.5488	0.8	-0.017	-0.017

K_T , K_Q , and efficiency (η) values of both CFD results (Table -13) and empirical values (Table-14) are plotted with respect to advance coefficient and is shown in Fig. 9. From these performance curves, the maximum efficiency of this propeller can be determined.

The maximum efficiency using empirical method is found to be 58.2% at a velocity 6.4116 ms^{-1} where in the case of CFD method, the maximum efficiency is about 64.6% at the velocity 7 ms^{-1} .

At our design speed 4.144 ms^{-1} corresponds to advance coefficient j equals to 0.4, the efficiency for empirical and CFD method are almost similar and is about 50%, but the empirical values are always slightly higher than the empirical ones.

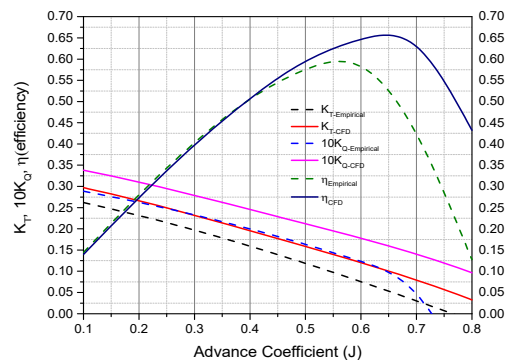


Figure 9: Performance Curve of Propeller

CONCLUSIONS

In this paper a design procedure of a marine propeller and its performance characteristics was discussed. It orders to design 3D the marine propeller PropCAD and Rhinoceros software were used. For the analysis of performances, Ansys Fluent was used. The CFD results were compared with empirical values and it is found that the CFD values always slightly higher than the empirical one. At the preliminary design stages, this method is useful to predict the performances of the propeller. In this work mesh convergence criteria were not carried out though it is required mesh convergence for CFD analysis.

REFERENCES

- [1] Barru Harish, Kondapalli Siva Prasad, G. Uma Maheswara Rao, - "Static Analysis of 4-Blade Marine Propeller" -(Journal of Aerospace Engineering & Technology, Volume 5, Issue 2, 2015-ISSN: 2231-038X Online)
- [2] Chang-Sup Lee¹, Young-Dal Choi², Byoung-Kwon Ahn¹, Myoung-Sup Shin¹ and Hyun-Gil Jang, "Performance optimization of marine propellers "(International Journal of Naval Architecture and Ocean Engineering, SNAK, 2010, Volume 2), Page 211-216
- [3] Marian RISTEA, Adrian POPA, Dragos Ionut NEAGU- "CFD modeling of a 5 bladed propeller by using the RANSE approach"- "Mirceacel Batran" (Naval Academy Scientific Bulletin, Volume XVIII – 2015) – Issue 2.
- [4] Mohamed M Helal, Tamer M Ahmed, Adel A Banawan and Mohamed AKotb- "Numerical prediction of the performance of marine propellers using computational fluid dynamics simulation with transition-sensitive turbulence model" - Proc IMechE Part M: J Engineering for the Maritime Environment 00(0). 2018
- [5] Shiodu Anthony, Williams Ekwere, Ezenwa Ogbonnaya and Kuvie Ejabefio, "Design Procedure of 4-Bladed Propeller" - (West African Journal of Industrial and Academic Research Vol.8) - No.1 September 2013.
- [6] Yanni Chang- "A comparative studyon the performances of different propeller designs", M.Sc. Thesis, University of South Eastern Norway, 2016.